Abstract

Natural and Anthropogenic Contributions to Urban Heat Islands

Lei Zhao

2015

Land use/land cover change has significant influences on climate system on both local and global scales by altering the biogeochemical and biogeophysical processes. Urbanization has been one of the most significant anthropogenic modifications to the Earth's surface in recent decades. The influence of urbanization on surface climate has a profound impact on the lives of urban residents, who comprise more than half of the world's population now and will comprise 70% of the world's population by the year of 2050. Conversion of natural land to urban land leads various changes in surface climate such as changes in temperature, humidity, precipitation, and air pollution. Among them, urban heat island (UHI), a ubiquitous phenomenon in which surface temperatures are higher in urban areas than in surrounding rural areas, represents one of the most significant human-induced changes to the surface climate. It is also a long-recognized and widely studied phenomenon in the research field of urban climate.

Although the candidate causes of UHI have been known for a long time, there is little knowledge on the relative contribution of each factor to UHIs. Previous modeling studies mostly focused on a short time scale of UHIs rather than on a climate scale. The observation-based studies cannot mechanistically quantify the contributions of each biophysical process to UHIs. Nor have these contributions been contrasted in different climate regimes. This dissertation aims to fill these gaps, for the first time quantifying the

contributions of primary causes to UHIs and contrasting among difference climate regions.

A long-held perception is that reduction in evaporative cooling in urban land is the dominant driver of UHI. In this dissertation, however, we used MODIS observations and climate modeling to show that this perception is somewhat erroneous. We conducted two separate climate simulations: one in current climate (1972-2004) and the other in future climate (2005-2100). The current-climate simulation was driven by a carefully revised climatology dataset, and the future-climate simulation was driven by the community earth system model outputs.

Results show that, for cities across North America, daytime UHI is strongly correlated with precipitation, whereas nighttime UHI is correlated with the logarithm of population but invariant with climate. The geographic variations in daytime UHI are largely driven by variations in the efficiency with which urban and rural areas convect heat to the lower atmosphere. This convection effect depends on the local background climate, contributing 3.0 ± 0.3 K (mean and standard error, s. e.) warming to daytime ΔT in cities in humid climate but causing 1.5 ± 0.2 K cooling in dry climate. Our results also show that in the humid eastern United States, there is evidence of higher daytime UHI in drier years. These relationships imply that UHIs will exacerbate heatwave stress on human health in wet climates. During nighttime, our results reaffirmed that the release of stored heat is the dominant driver of UHIs. Results also support the city albedo management as a viable means of mitigating UHIs on large scales.

Results of the future-climate simulation show that under the high emission climate change scenario (representative concentration pathway 8.5), daytime UHIs generally decrease in all three climate zones, indicating that urban and rural areas respond differently to climate change. Nighttime UHIs do not show any significant trends. Attribution of UHIs demonstrates how urban land-atmosphere interactions change with climate change.

Natural and Anthropogenic Contributions to Urban Heat Islands

A Dissertation

Presented to the Faculty of the Graduate School

of

Yale University

in Candidacy for the Degree of

Doctor of Philosophy

by

Lei Zhao

Dissertation Director: Xuhui Lee

May 2015

Copyright © 2015 by Lei Zhao

All rights reserved.

Table of Contents

List of Figures

List of Tables

Acknowledgements

I have been incredibly fortunate to enjoy the intellectual, and emotional support of countless individuals and organizations throughout my thesis work.

I would like to first thank my advisor, Prof. Xuhui Lee for his trust, support, and tremendous help during my doctoral study at Yale. I would never forget the countless times that he pointed me to the right direction, kept my momentum, and inspired me when I felt lost and hopeless. I have benefitted greatly from his thinking, his writing, his teaching, his way of doing research, and also his personalities. He has been not only my academic advisor but also my mentor of life. He always provides me with precious advices on not only my research but also my career, and my life. He has been a constant source of inspiration, guidance and support.

My sincere appreciation goes to my other committee members, Prof. Karen Seto, Prof. Ronald Smith, and Prof. Nadine Unger, who were more than generous with their knowledge, expertise and precious time. Every time after listening to my presentation, Prof. Seto would send me a list of suggested papers. I always enjoy the inspiring and challenging questions from Prof. Smith at our meetings. Answering those questions far more than rewarding. Without his help, I cannot finish the papers that I published. Prof. Unger, no matter how busy she was, would always schedule times meeting with me, listening to my immature reports, and providing me inspiring insights. I feel so much honored and fortunate to have such a great committee.

I would like to thank Dr. Keith Oleson from National Center of Atmospheric Research for his tremendous help and support on my research and his generous with sharing expertise on CESM simulation. He always offers first priority for my questions no matter how stupid they are and discussions. Without him, I cannot imagine how hard it would be for me to catch such a complex modeling system.

I am thankful to have worked alongside my labmates Kyounghee Kim, Xin Zhang, Bin Deng, and Natalie Schultz. This group has not provided encouragement, feedbacks, and useful suggestions, but also enriched my life at Yale.

Most importantly I would like to thank my fiancée, Xiao Yang. Words cannot describe what her constant presence has meant to me; nor can they weigh how it has enabled me.

Finally, I would like to express how honored, fortunate, and grateful I am to be a student at Yale. This campus, these people I met here, and the times I spent here will no doubt to be engraved into my mind for ever together with Yale's motto: Lux et veritas.

Chapter 1 Introduction

1.1 Land use change

Land use/land cover change influences the climate system by altering biogeochemical and biophysical processes at the surface. The biogeochemical effect, such as changes in CO2 concentration, impacts the climate system on the global scale but hardly on the local scale. The biophysical effect, however, including changes in surface albedo, emissivity, surface roughness, evaporation and thermal storage, has important impacts on the climate system at both local and global scale by triggering biophysical feedbacks from the surface energy balance perspective[*Bonan*, 2008; *Lee et al.*, 2011]. Ongoing anthropogenic land-use activities, such as urban expansion, are occurring at local scales which are too small to influence the global climate, but have direct effects on local climate [*Kalnay and Cai*, 2003; *Zhou et al.*, 2004]. Conversion of different landscapes causes localized warming or cooling effect through perturbations to the biophysical processes of the Earth's surface energy balance, among which urban heat island (UHI) is one of the most prominent effect that humans bring to the Earth.

1.2 Urban climate and urban heat island

Urbanization has been the most significant anthropogenic modification to the Earth's surface in recent decades [*Grimm et al.*, 2008; *Kalnay and Cai*, 2003; *Oleson*, 2012]. Although urban area takes a small fraction of the Earth's land surface till now, its climate has a profound impact on the human beings, because urban residents comprise more than half of the world's population[*Grimm et al.*, 2008]. Many globally recognized environmental problems such as climate change, air pollution,

flood, water pollution, energy crisis, and disease stem from or are exacerbated by human activities within urban areas [*Bettencourt and West*, 2010]. In recognition of these public issues, increasing attention has been drawn to interdisciplinary research of understanding the urban environment and climate, and devising adaptation and mitigation strategies [*Georgescu et al.*, 2014; *Mackey et al.*, 2012; *Stone et al.*, 2012; *Stone et al.*, 2014; *Stone et al.*, 2013].

Conversion of natural land to urban land leads to a number of differences in climatology between urban and its surrounding rural areas. Among them, urban heat island (UHI), a concept describing the phenomenon that urban areas are generally warmer than the surrounding rural areas, is one of the most well-documented and actively studied topics in the field of urban climatology [*Arnfield*, 2003]. The UHI is first recognized by Luke Howard in 1820 [*Landsberg*, 1981] and was first scientifically studied in 1970s. From then on, a large number of research efforts have been made on observing, modeling, and understanding the UHI [*Arnfield*, 2003; *Chen et al.*, 2011; *Clinton and Gong*, 2013; *Fischer et al.*, 2012; *Gallo et al.*, 2002; *Georgescu et al.*, 2014; *C S B Grimmond et al.*, 2010; *S Grimmond*, 2007; *Hung et al.*, 2006; *Imhoff et al.*, 2010; *Li and Bou-Zeid*, 2013; *Oke*, 1973; 1976; 1982; *Oleson*, 2012; *Oleson et al.*, 2011; *Peng et al.*, 2012; *Roth et al.*, 1989; *Taha*, 1997; *Voogt and Oke*, 2003]. The UHI, however, remains a compelling field for climate research because there are still a number of unresolved questions regarding the mechanism, the impacts, and the mitigation of UHI. The emergence of the idea that there are multiple UHIs even brings more complexities to the research of UHI.

Previous reports have confirmed the presence of more than one UHI concepts, including surface UHI as defined by the surface radiative temperature difference and observed by remote sensing technologies, the UHI in the urban canopy layer as measured by screen height air temperature, and the UHI upper in the urban boundary layer. These UHIs behave differently and are controlled by different physical processes [*Oke*, 1976; 1982; *Roth et al.*, 1989; *Voogt and Oke*, 1997]. Among these UHIs at different levels, the canopy layer air temperature UHI and the satellite-derived radiative surface UHI are the two most widely measured and studied concepts. The former suffers from inhomogeneity in the urban landscape. The latter is a valuable spatial average, but is influenced by the emissivity of the surface. Neither exactly matches the human experience of UHI as an individual walks across the rural or urban landscape. For the purpose of comparing different cities, the surface temperature approach is easier and more stable. *Nichol et al.* [2009] showed that the correlation between the surface and screen-height air temperature can be weak on neighborhood scales and improves considerably at the scale of urban–rural transition. Therefore in this dissertation, I focused the UHI intensity defined by the urban-rural difference of surface radiative temperature.

1.3 Contributors to UHI

Candidate causes of UHI include:

- high heat capacity and heat conductivity of urban construction materials which lead to increased surface heat storage;

- large vertical faces and reduced wind speeds which lead to decreased turbulent heat transport;
- larger impervious areas and less vegetation which lead to decreased latent heat flux;
- additional supply of energy – anthropogenic heat flux.

These factors of UHI have been known for a long time [*S Grimmond*, 2007]. No matter what urban characteristics these factors change, they essentially contribute to UHI by perturbing the terms in the surface energy balance.

A number of studies have explored the relative contributions of the candidate causes to the UHI [*Piringer et al.*, 2002]. These studies can be grouped into two categories. First category is the studies based on a single city or a few cities [*Giannaros and Melas*, 2012; *Hicks et al.*, 2010; *Roth and Chow*, 2012; *Tereshchenko and Filonov*, 2001; *K C Wang et al.*, 2007]. These studies mostly focused on the temporal variation of the UHI. Some recent modeling studies conducted sensitivity analyses to test the influence of urban parameters to UHI [*Oleson et al.*, 2011; *Oleson et al.*, 2008a], but the parameters examined are basically internal urban factors such as morphology, physical and thermal parameters. The second category is the studies using a large number of locations. These studies are able to investigate the dominant factor that drives the spatial variation of UHI on a large scale. However, identification of the primary factor of UHI is still controversial. One traditional view suggests that the urban geometry or morphology, such as city size or city height-to-width ratio, is the primary driver of UHI spatial variation [*Oke*, 1973; 1981; 1987]. Another long-held

perception from studies in recent years is that reduction in evaporative cooling because of the sharp decrease in vegetation cover between urban and rural areas is the dominant driver [*Imhoff et al.*, 2010; *Peng et al.*, 2012; *Taha*, 1997].

In this dissertation, I will combine theory, observations, and climate modeling to disentangle the relative contributions of both natural and anthropogenic processes to urban heat island. Because this is a mechanistic study of UHI, land surface modeling is necessary.

1.4 Land surface models

A land surface model (LSM) is usually the land component of a climate model. In terms of the physics, a LSM contains two major schemes: biogeophysical parameterization and biogeochemical parameterization. There are major functions for a LSM to its climate model. First is to update surface state variables such as surface temperature, surface humidity, soil moisture, and soil temperature. The second function is to calculate surface turbulent fluxes including energy flux, momentum flux, and mass flux to provide boundary conditions for the atmospheric model.

Surface energy balance (SEB) is one of the most important constrains for solving the equations in the LSMs. In most LSMs, the emitting long-wave radiation term, the sensible heat flux, the latent heat flux, and the heat storage term are parameterized as functions for surface radiative temperature. Therefore the SEB equation can be solved numerically for surface radiative temperature. Using surface radiative temperature to

parameterize sensible heat flux accurately requires some special treatments to heat transfer resistance, which are, however, neglected by most of the LSMs. Therefore through the completion of this dissertation, we investigated the impacts of using surface radiaitve temperature in bulk transfer method on predicting sensible heat flux. Because this part of work does not fit in the major objectives of this dissertation, the details of this work is documented in the Appendix of this dissertation (Appendix A).

Most LSMs can be run in two modes: offline stand-alone mode with user-defined forcing data and online coupled mode. The forcing data for LSMs are common meteorological variables including air temperature, wind speed, specific humidity, pressure, shortwave radiation, longwave radiation, and precipitation. These data come from either user-defined input if a LSM is run in offline mode or outputs of an atmospheric model if it is run in online mode. The key difference between these two modes is the scale. Offline mode essentially omits all the large-scale feedbacks and the horizontal atmospheric advections. It can be considered as a retrieval of the surface response to the current atmospheric state. Online mode incorporates both small-scale physics and large-scale dynamics and feedbacks. It is more suitable to simulate a process that will trigger or be impacted by the large-scale feedbacks.

Initially, most LSMs are for natural surfaces such as forest, grassland, crops, lake, and bare soil. As the recognition of increasing needs for urban modeling research, LSMs started to incorporate urban land surface parameterization schemes for urban land. Existing urban LSMs can be categorized into three groups according to the extent of

complexity. The first one is a group of empirical models, representing the least complexity. These models are based on empirical relations and very basic urban form parameters such as average building height and vegetation fraction. The Local-Scale Urban Meteorological Parameterization Scheme (LUMPS) by *C S B Grimmond and Oke* [2002] is a good example of this kind of LSM. The second group, slightly more complex than the first one, is adaptations of existing land surface schemes for soil and vegetated surfaces [*C S B Grimmond*, 2006]. These models simply alter the parameterizations or even just values of some parameters of the existing LSMs for natural surfaces, to account for the momentum and energy transfer from built-up surfaces and the radiation trapping by the canyon effects [*Best et al.*, 2006; *Dandou et al.*, 2005; *Dupont et al.*, 2004; *Otte et al.*, 2004]. The anthropogenic heat estimated by simple empirical schemes is also incorporated in these models [*Souch and Grimmond*, 2006]. The third group is the most complex urban LSM. These models consider the three-dimensional effects of buildings, and solve surface energy balance (SEB) equation separately for roofs, roads and walls. This group of urban models can be further divided into two classes. The first one is single-layer model. This type of models assumes that the urban canopy interacts with only one atmospheric layer above the uppermost roof of the buildings [*Harman et al.*, 2004; *Lemonsu et al.*, 2004; *Masson*, 2000; *Masson et al.*, 2002; *Oleson et al.*, 2008a; *Oleson et al.*, 2008b]. The second one is multilayer model. This type of models assumes that the built-up area distribute the impacts across multiple layers of atmosphere within the lower boundary layer [*Kondo et al.*, 2005; *Martilli et al.*, 2002].

Among these urban LSMs of different complexities, which model to choose depends on the scale and the objectives of your research. In this dissertation, we used the community land model (CLM), which is the land component of NCAR's climate model – community earth system model (CESM). There are three reasons why chose this model. First, CLM is a single layer LSM. It has the enough complexity in land surface physics to facilitate a mechanistic study, and yet is simple enough in computational burden and auxiliary data requirement for cities. Second, our work focused on the climatology of urban areas rather than a single event of a few days, therefore we chose a climate model which is suitable for long-time simulation as opposed to a weather forecast model. Lastly, This model has a surface information dataset that contains urban configuration and parameters for the whole globe, which allows us to analyze a large number of cities on the large scale easily. This fits the objectives of our work.

1.5 Research questions and methods

This dissertation aims to address the following research questions:

1) What is the primary driver that largely explains the spatial variation of UHI intensity? Is the dominant driver the same for daytime UHI and nighttime UHI?

2) What is the relative contribution of each biophysical process to urban heat island? How do these biophysical contributions to UHI reflect the interactions between urban land and lower atmosphere?

3) How does UHI vary with climate change in the future? How do urban land – atmosphere interactions change with climate change?

In order to address these questions, we designed our research work in three major steps. First, choose correct forcing dataset for CLM. Because the focus of our research is essentially land – atmosphere interactions on the local scale, we chose to run CLM in the offline mode. The question then is what forcing datasets should we use. Previous reports have found that most global climate models overestimate the incoming solar radiation at Earth's surface [*Wild et al.*, 2013]. Solar radiation is an important driver of surface exchange processes. An overestimated solar radiation must lead to a biased solution of surface energy balance equation in CLM. But how about reanalysis data? Can we use reanalysis dataset to drive the CLM? Therefore the first step of our work was to validate the surface solar radiation of data assimilation systems.

Second, after correctly choosing the forcing dataset to drive the CLM, we ran the simulation for 33 years using current climatology. An attribution method was developed based on surface energy balance equation and bulk transfer parameterization for sensible heat flux. We applied the attribution model on the CLM modeled data to decompose the UHI into contributions from each biophysical process.

Third, we ran the CLM simulation into the future under Representative Concentration Pathway (RCP) 8.5 scenario. Based on the modeled data of this future projection, we forecasted the UHI trend under climate change and the urban land – atmosphere interactions in the future.

1.6 Dissertation outline

This dissertation explores the physical mechanism of radiative temperature-derived urban heat island in the current and future climate with a focus on the natural and anthropogenic contributions.

Chapter 1 provides an overview of the motivation of urban studies, previous research work on urban climate and UHI, understandings of urban land surface models, and the major research questions and methods of this dissertation.

Chapter 2 to 4 present in detail the research work conducted along the path of my doctoral dissertation, following the three steps described in Chapter 1. Specifically, **Chapter 2** describes the work on validation of surface solar radiation of data assimilation systems. We also proposed a post-reanalysis algorithm to correct the overestimation of surface solar radiation by reanalysis systems. **Chapter 3** presents relative contributions of biophysical processes to UHI and what process primarily determines the large-scale spatial variation of UHI. **Chapter 4** shows how UHI and urban land-atmosphere interactions will change with climate change in the future.

Chapter 5, the last chapter, summarizes the major results and concluding remarks of this dissertation and provides some possible directions for future research.

Chapter 2 Reanalysis surface solar radiation

Published as Zhao, L., X. H. Lee, and S. D. Liu (2013), Correcting surface solar radiation of two data assimilation systems against FLUXNET observations in North America, *Journal of Geophysical Research-Atmospheres*, *118*(17), 9552-9564, doi:Doi 10.1002/Jgrd.50697.

Summary

Solar radiation at the Earth's surface is an important driver of meteorological and ecological processes. The objective of this study is to evaluate the accuracy of the reanalysis solar radiation produced by NARR (North American Regional Reanalysis) and MERRA (Modern-Era Retrospective Analysis for Research and Applications) against the FLUXNET measurements in North America. We found that both assimilation systems systematically overestimated the surface solar radiation flux on the monthly and annual scale, with an average bias error of +37.2 W m^{-2} for NARR and of +20.2 W m^{-2} for MERRA. The bias errors were larger under cloudy skies than under clear skies. A post-reanalysis algorithm consisting of empirical relationships between model bias, a clearness index, and site elevation was proposed to correct the model errors. Results show that the algorithm can remove the systematic bias errors for both FLUXNET calibration sites (sites used to establish the algorithm) and independent validation sites. After correction, the average annual mean bias errors were reduced to +1.3 W m^{-2} for NARR and +2.7 W m^{-2} for MERRA. Applying the correction algorithm to the global domain of MERRA brought the global mean surface incoming shortwave radiation down by 17.3 W m^{-2} to 175.5 W m^{-2}. Under the constraint of the energy balance, other radiation and energy balance terms at the Earth's surface, estimated from independent global data products, also support the need for a downward adjustment of the MERRA surface solar radiation.

2.1 Background

Solar energy at the earth's surface (*S*) is an important driver of various interactions between the land and the atmosphere. To improve our understanding of how meteorological processes distribute energy in the climate system, an accurate assessment of this variable is required. Because this variable is not among the measurements made at standard surface weather stations, models of various complexities are used to estimate its spatiotemporal distributions. Atmospheric reanalysis is one such class of models. In reanalysis model systems, solar radiation at the surface is calculated with radiative transfer models (RTMs). The reanalysis modeled products are superior to discrete surface observations because of large and continuous spatial and temporal coverages. These features are especially attractive for people interested in climate and ecological patterns on the regional and global scale.

Implementation of RTMs can be divided into two categories: stand-alone mode and application embedded in global climate models (GCMs) or reanalysis systems. The stand-alone models provide accurate single column calculations, while the applications in GCMs and reanalyses are suited for regional and global scales with minimal loss of accuracy. Previous efforts have taken advantages of both types of the RTMs to produce the radiation fluxes at the top of atmosphere (TOA), within the atmosphere and at the surface [*Hatzianastassiou et al.*, 2005; *Kiehl and Trenberth*, 1997; *Rossow and Zhang*, 1995; *Zhang et al.*, 1995; *Zhang et al.*, 2004]. Of interest

here is the discrepancy in the estimate of the global mean *S*. According to the ISCCP-FD (fluxes using the International Satellite Cloud Climatology Project–D input data), the global mean *S* value is 188.5 Wm^{-2} for the period of 2000 to 2004 [*Trenberth et al.*, 2009]. Using the same cloud climatology in the ISCCP-D series but a different RTM and ancillary datasets [*Zhang et al.*, 2004], *Hatzianastassiou et al.* [2005] estimated a mean value of 171.6 Wm^{-2}. These two estimates differ by 17 Wm^{-2} or 9.8%, indicating uncertainties in the various RTMs or input datasets used.

Validation of reanalysis model products against surface observations is an active area of research. This is because reanalysis represents only the best "guess" of various atmospheric and hydrological variables through a combination of model predictions and a variety of observations, the latter of which serve to constrain the model calculations. One source of error is the spatial and temporal mismatch between the model analytical framework and the observational datasets. In the case of radiative fluxes, neither cloud observations nor surface radiation measurements are directly assimilated in the model system. (MERRA assimilates clouds indirectly by adjusting moisture over the oceans.) Furthermore, as noted above, the RTMs imbedded in the modeling system have their own inherent uncertainties.

Several investigators have compared the surface radiation variables produced by NARR and MERRA against field observations. Using the data obtained at a FLUXNET site in Oklahoma, USA, *Kennedy et al.* [2011] concluded that both MERRA and NARR have positive biases (NARR: 47 Wm^{-2}; MERRA: 19 Wm^{-2}) for

S and negative biases for the surface downward longwave radiation. They attributed the significant positive bias in NARR to a combination of too low cloud amounts in the model domain and too weak light extinction by aerosols and water vapor. *Markovic et al.* [2009] found similar positive biases (40 Wm^{-2}) in the annual mean *S* for NARR at six sites in six states from west to east US and attributed them to a negative bias in cloud fraction. *Walsh et al.* [2009] evaluated surface radiative fluxes and cloud fraction from NARR and three other reanalyses against ground measurements at Barrow, Alaska in the Arctic, and found positive biases of +4 to +43 W m^{-2} in monthly *S* and the associated negative biases of cloud fraction. Over the same region, *Zib et al.* [2012] found an annual mean high bias of 3.9 Wm^{-2} for MERRA at two BSRN (Baseline Surface Radiation Network) sites. They also related the bias errors to biases in the modeled cloud fraction although the radiation biases still exist for some time periods despite that the observed cloud fraction is correctly reproduced by the model. In a recent evaluation study involving six reanalysis products at nine field sites on the Tibetan Plateau, *A Wang and Zeng* [2012] reported an overestimation of up to 40 W m^{-2} for *S* in MERRA. According to their study, the bias errors appear to be related to latitude.

The few investigations conducted over large spatial scales have confirmed the tendency for reanalysis models to overestimate the surface solar radiation. Utilizing hourly observations at 33 FLUXNET sites in the US and Canada, *Decker et al.* [2012] evaluated a number of surface micrometeorological and flux variables produced by the NCEP/NCAR, CFSR, ERA-40, ERA-Interim, GLDAS and MERRA reanalysis

systems, concluding that all of them overestimate *S* by varying amounts of 10 to 50 Wm^{-2} with ERA-Interim having the best accuracy. In another large-scale evaluation study, *Wild et al.* [1998] compared surface solar energy of the reanalysis product ECMWF (European Center for Medium Range Weather Forecasts) against the monthly mean radiation observations at 720 GEBA (Global Energy Balance Archive) sites distributed worldwide. In terms of annual means, an underestimation at low latitudes in the Northern Hemisphere and an overestimation in the rest of the world were found in the study. But overall, the reanalysis bias errors are substantially smaller than in GCMs estimates [*Wild et al.*, 1995].

The published studies show that the annual mean bias errors of reanalyzed *S* are in the range of +5 to +60 W m^{-2}. These positive bias errors have undesirable consequences for atmospheric and ecological applications. First, these bias errors are 5-30% of the observed net all-wave surface radiation balance at mid-latitude forests [*Lee et al.*, 2011; *Rotenberg and Yakir*, 2010]. Use of the reanalyzed surface solar radiation to drive land surface model calculations will result in extra energy going to the atmosphere via sensible and latent heat fluxes assuming other radiation terms remain unchanged. An excess of net radiation at the surface, for example, could cause excessive surface evaporation especially under moist climate [*Betts et al.*, 1996]. Under the assumption that surface evaportransporation is balanced by precipitation, this would lead to excessive precipitation in climate models. In reanalysis systems excessive surface evaportransporation calculated by the model may not be balanced by precipitation assimilated from observations, thus forcing the model to drift to a dry

soil state [*Viterbo and Courtier*, 1995]. Second, the reanalysis *S* is used to predict surface ozone formation [*Hickman et al.*, 2010; *Leung and Gustafson*, 2005; *Mickley et al.*, 2004; *Nolte et al.*, 2008; *Weaver et al.*, 2009]. The study by *Nolte et al.* [2008] suggests that a high bias error of 20 W m^{-2} in *S* can cause an increase of surface ozone concentration by about 3-5 ppb in eastern Texas and along much of the east coast of the US. Third, because solar radiation is the primary driver of plant photosynthesis, bias errors in *S* are problematic for ecological models. Finally, the reanalysis radiation data is used to assess the global energy budget of the climate system [*Bosilovich et al.*, 2011; *Stephens et al.*, 2012a; *Stephens et al.*, 2012b; *Wild*, 2009]. The reported bias errors in *S* are comparable in magnitude to the global mean surface sensible heat flux [*Trenberth et al.*, 2009], emphasizing the need for a quantitative correction algorithm.

The first objective of this study is to evaluate the two reanalysis *S* products, NARR and MERRA, against the FLUXNET observations in North America. Our strategy is to perform the evaluation at a large number of FLUXNET sites across different climate regimes, over a wide range of elevations, and at multiple time scales of months to multiple years. Simultaneous evaluation of two reanalysis products may help us to uncover model errors related to the data sources and the approach taken by the models. FLUXNET is a global network of eddy flux towers which maintain continuous measurements of surface meteorological variables and land-atmosphere fluxes [*Baldocchi et al.*, 2001]. Because our analysis is conducted with monthly averages, it is essential that the sites have long records to produce large

enough numbers of gap-free months for rigorous comparison. Many FLUXNET sites satisfy this criterion (Table 2.1). In addition, long time series allow us to examine the capability of the reanalyses to capture the interannual variations in *S*.

Our second objective is to develop an algorithm for reducing the systematic errors. A computationally efficient post-reanalysis correction algorithm is desired by the end users engaged in the applications discussed above. The routine was applied to the MERRA data to obtain a sense of its bias in the global mean *S* estimate. Although the algorithm is restricted to MERRA and NARR, the insights gained may be useful for developing correction algorithms for other reanalysis products.

As in *Decker et al.* [2012] and *Wild et al.* [1998], we validated the reanalyzed *S* products against a large number of observational sites. We expanded the work of *Wild et al.* [1998] by focusing not only on annual mean *S* but also on its seasonal and interannual variations. Instead of using hourly data as in *Decker et al.* [2012], we conducted the comparison using monthly means which have smaller random errors than the hourly data, allowing better isolation of systematic errors.

Table 2.1 Annual mean surface incoming solar radiation fluxes at and ancillary information on the calibration and validation sites.

Site Code	Site Name	State /Prov	Lat	Long	Elev (m)	Yeas Included	Annual Means	Annual Mean Bias		Reference
							Observed (Wm^{-2})	NARR (Wm^{-2})	MERRA (Wm^{-2})	
Calibration										
CA-Obs	Old Black Spruce	SK	53.99	-105.12	629	10	134.6	29.2	18.6	[*Jarvis et al.*, 1997]
CA-Ojp	Old Jack Pine	SK	53.92	-104.69	579	10	133.3	30.8	19.9	[*Baldocchi et al.*, 1997]
CA-Oas	Old Aspen	SK	53.63	-106.20	601	10	136.4	29.6	19.5	[*Blanken et al.*, 1997]
CA-Ca1	BC Douglas-fir 1949	BC	49.87	-125.33	320	12	127.2	34.6	21.0	[*Humphreys et al.*, 2003]
US-UMB	UMBS	MI	45.56	-84.71	234	8	150.8	39.3	22.5	[*Schmid et al.*, 2003]
CA-Cbo	Borden	ON	44.20	-79.93	217	14	149.2	39.8	26.0	[*Lee et al.*, 1999]
US-NR1	Niwot Ridge	CO	40.03	-105.55	3050	5	188.0	59.8	37.0	[*Monson et al.*, 2002]
US-MMS	Morgan Monroe State Forest	IN	39.32	-86.41	275	9	167.6	41.0	22.7	[*Schmid et al.*, 2000]
US-Ton	Tonzi Ranch	CA	38.43	-120.97	177	7	218.8	23.6	6.0	[*Ma et al.*, 2007]
US-Var	Vaira Ranch	CA	38.41	-120.95	129	8	213.1	26.9	9.0	[*Ma et al.*, 2007]
US-WBW	Walker Branch	TN	35.96	-84.29	343	10	174.3	35.6	22.8	[*Wilson and Meyers*, 2001]
US-Aud	Audubon Research Ranch	AZ	31.59	-110.51	1469	6	237.2	35.0	11.1	[*Krishnan et al.*, 2012]
US_SP2	Mize	FL	29.76	-82.24	43	7	184.2	41.3	18.9	[*Gholz and Clark*, 2002]
US-SP3	Donaldson	FL	29.75	-82.16	36	7	182.1	43.1	21.1	[*Gholz and Clark*, 2002]
Validation										
CA-Qfo	Quebec Mature Boreal Forest	QC	49.69	-74.34	390	1	127.9	30.9	24.7	[*Bergeron et al.*, 2007]
CA-Ca3	BC Douglas-fir 1988	BC	49.53	-124.90	120	1	133.5	35.5	17.5	[*Humphreys et al.*, 2006]
US-Ho1	Howland Forest Main	ME	45.20	-68.74	60	2	150.7	37.7	28.5	[*D Y Hollinger et al.*, 1999]
US-Bkg	Brookings	SD	44.35	-96.84	510	4	175.3	35.4	12.4	[*Gilmanov et al.*, 2005]

US-Bo1	Bondville	IL	40.01	-88.29	219	7	168.7	39.6	23.7	[*S E Hollinger et al.*, 2005]
US-Slt	Silas Little Experimental Forest	NJ	39.91	-74.60	30	4	159.5	48.5	27.6	[*Clark et al.*, 2010]
US-MOz	Missouri Ozark	MO	38.74	-92.20	219	4	180.0	39.4	16.4	[*Gu et al.*, 2006]
US-Dk2	Duke Forest Hardwoods	NC	35.97	-79.10	168	5	183.4	35.7	15.3	[*Oren et al.*, 2006]
US-NC2	North Carolina Loblolly Pine	NC	35.80	-76.67	12	4	170.3	40.3	27.2	[*Noormets et al.*, 2010]
US-Fmf	Flagstaff Managed Forest	AZ	35.14	-111.73	2160	3	230.2	36.1	13.4	[*Dore et al.*, 2008]

2.2 Materials

2.2.1 Surface observations

The Ameriflux (level 2) and FLUXNET-CANADA (http://public.ornl.gov/ameriflux/index.html; http://fluxnet.ccrp.ec.gc.ca/e_about.htm) are two regional networks of FLUXNET, consisting of eddy-covariance sites in North America, Central America, and South America. In this study, we selected 24 sites, spanning a large geographic range of the US and Canada (Figure 2.1). Of these, 14 sites have long measurement records and were used as calibration sites (sites used to develop the correction algorithm). The other 10 sites were used as validation sites (sites used to independently validate the corrected *S*). These sites all measured the four components of the surface radiation balance and had high (>90%) data coverage. All the sites in this study used a pyranometer to measure *S*, but the sensor type varies. The uncertainty of measured *S* in Ameriflux is ±3.55 W m^{-2} according to a cross-site comparison with a roving Ameriflux standard pyranometer [*Schmidt et al.*, 2012].

BSRN [*Ohmura et al.*, 1998], established in 1992, is a global network of continuous measurements of radiative fluxes at the Earth's surface. It has 56 stations, covering a latitudinal range from 80°N to 90°S. BSRN monitors the global solar irradiance primarily by a combination of diffuse sky irradiance measured by a shaded pyranometer and direct solar irradiance measured by an absolute cavity radiometer, with a target accuracy of 5 W m^{-2} [*Ohmura et al.*, 1998]. In this study we selected 42 BSRN sites for further validation of the correction algorithm outside of North America (Figure 2.2 and Table 2.2); at these sites, measurements are complete for at

least one year. In addition to the BSRN sites, we also include on the validation list the data from the published literature in which the observed annual mean *S* is reported.

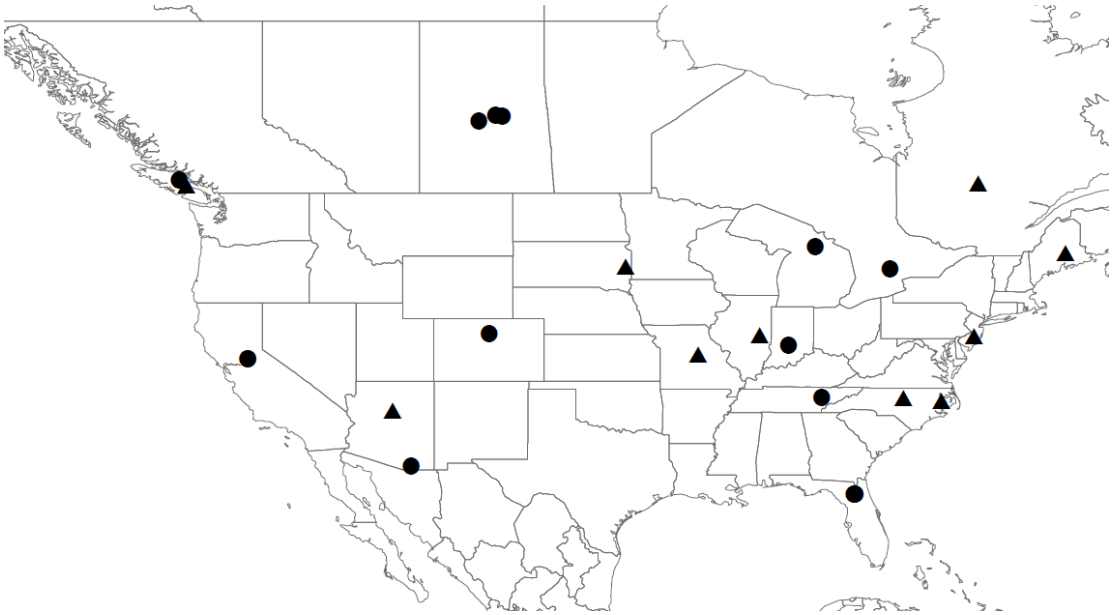

Figure 2.1 Map of the selected Ameriflux and FLUXNET CANADA sites. Circles denote the calibration sites; and triangles denote the validation sites.

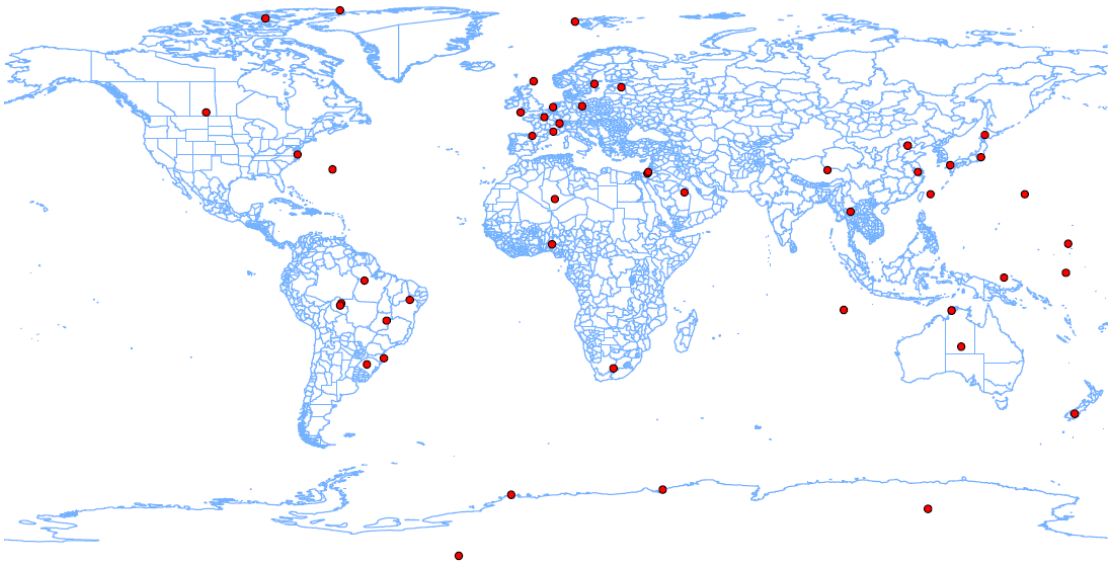

Figure 2.2 Map of the validation sites from BSRN and the published literature

Table 2.2 Validation sites from BSRN and the published literature.

Site label	Area	Latitude	Longitude	Elevation (m)	Year	Mean (W m^{-2})	Reference
ALE	Lincoln Sea	82.49	-62.42	127	2005-2007	103.7	
ASP	Macdonnell Ranges, Northern Territory, Australia	-23.80	133.89	547	2002-2009	260.7	
BER	Bermuda	32.27	-64.67	8	2000-2008	191.3	
BRB	Brasilia City, Distrito Federal, Brazil	-15.60	-47.71	1023	2010-2011	231.0	
CAB	The Netherlands	51.97	4.93	0	2006-2011	123.0	
CAM	United Kingdom	50.22	-5.32	88	2001-2007	128.7	
CAR	France	44.08	5.06	100	2000-2010	181.2	
CNR	Spain, Sarriguren, Navarra	42.82	-1.60	471	2009-2011	168.0	
CLH	North Atlantic Ocean	36.91	-75.71	37	2000-2009	184.3	
COC	Cocos (Keeling) Islands	-12.19	96.84	5.8	2006-2009	235.0	
DOM	Antarctica	-75.10	123.38	3233	2006-2009	157.0	
DAR	Australia	-12.43	130.89	30	2004-2009	238.7	
DWN	Australia	-12.42	130.89	32	2009-2010	225.5	
DAA	South Africa	-30.67	23.99	1287	2002-2003	237.0	

EUR	Ellesmere Island, Canadian Arctic Archipelago	79.99	-85.94	85	2008-2011	102.5	
FLO	South Atlantic Ocean	-27.53	-48.52	11	2000-2004	179.6	
FUA	Japan	33.58	130.38	3	2011	152.0	
GVN	Dronning Maud Land, Antarctica	-70.65	-8.25	42	2000-2010	127.2	
ILO	Nigeria	8.53	4.57	350	2000-2004	190.8	
ISH	Japan	24.34	124.16	6	2011	168.0	
KWA	North Pacific Ocean	8.72	167.73	10	2001-2007	228.9	
LAU	New Zealand	-45.05	169.69	350	2001-2008	163.5	
LER	United Kingdom	60.13	-1.18	84	2002-2006	92.8	
LIN	Germany	52.21	14.12	125	2000-2004	122.4	
MNM	Minami-Torishima	24.29	153.98	7	2011	218.0	
MAN	Papua New Guinea	-2.06	147.43	6	2000-2008	210.8	
NAU	Nauru	-0.52	166.92	7	2005-2007	245.7	
NYA	Ny-Ålesund, Spitsbergen	78.93	11.93	11	2000-2010	78.2	
PAL	France	48.71	2.21	156	2006	134.0	
PAY	Switzerland	46.82	6.94	491	2000-2008	144.4	
PTR	Brazil	-9.07	-40.32	387	2009	219.0	
REG	Canada	50.21	-104.71	578	2000-2007	160.3	
SAP	Japan	43.06	141.33	17	2011	140.0	
SBO	Israel	30.91	34.78	500	2005-2009	240.4	

SOV	Saudi Arabia	24.91	46.41	650	2002	265.0	
SPO	Antarctica	-89.98	-24.80	2800	2000-2009	129.0	
SYO	Cosmonaut Sea	-69.01	39.59	18	2000-2005	127.2	
SMS	Brazil	-29.44	-53.82	489	2009-2011	197.7	
TAM	Algeria	22.78	5.51	1385	2002-2010	265.2	
TAT	Japan	36.05	140.13	25	2005	161.0	
TOR	Estonia	58.25	26.46	70	2000-2010	111.4	
XIA	China	39.75	116.96	32	2006-2009	161.3	
Tibet	China	31.90	91.70	4620	2003	246.1	*Wang and Zeng* [2012]
Yatir	Israel	31.35	35.05	650	2000-2005	238.0	*Rotenberg and Yakir* [2010]
Tapajos SP	Brazil	-3.01	-54.58	100	June2000-May2001	180.0	*da Rocha et al.* [2004]
Forest Rondonia	Brazil	-10.08	-61.93	145	Sep1999-Sep2000	206.0	*von Randow et al.* [2004]
Pasture FNS	Brazil	-10.75	-62.37	293	Sep1999-Sep2000	202.8	*von Randow et al.* [2004]
Lake Taihu	China	31.40	120.22	7	2011	154.7	*Deng et al.* [2013]
GEBA Stockholm	Switzerland	59.30	17.95	55	2000	114.0	*Wild* [2009]
Mount Pui	Thailand	18.80	98.90	1263.1	1998	167.0	*Tanaka et al.* [2003]

2.2.2 NARR

The North American Regional Reanalysis (NARR), carried out by the National Center for Environmental Prediction (NCEP), is a long-term, near real-time, high-resolution, high-frequency, atmospheric and land surface reanalysis product [*Mesinger et al.*, 2006]. This regional reanalysis provides a much-improved dataset of land hydrology and land-atmosphere interactions compared to the earlier global reanalysis dataset NCEP-NCAR. NARR covers the period from 1979 up to the present, with the data archived at 3-hourly, daily, and monthly time scales. The grid resolution is approximately 32 km. Documented in the NARR outputs are meteorological, hydrological and ecological variables. Here we used the surface incoming shortwave radiation flux data.

The radiative fluxes at the surface are computed through the radiation scheme embedded in the NCEP Eta model, which has a shortwave [*Lacis and Hansen*, 1974] and a longwave package [*Fels and Schwarzkopf*, 1975]. The shortwave absorption scheme considers the amount and type of cloud, the humidity, the solar elevation angle and the vertical distribution of ozone within the stratosphere. The cloud information is obtained from the cloud microphysics in the Eta model [*Ferrier et al.*, 2002].

2.2.3 MERRA

MERRA [*Rienecker et al.*, 2011], maintained by NASA Global Modeling and Assimilation Office, is the second generation reanalysis dataset, which uses the

Goddard Earth Observing System Data Assimilation System - Version 5 (GEOS-5). GEOS-5 includes GEOS-5 atmospheric circulation model and the gridpoint statistical interpolation. MERRA implements a procedure called incremental analysis updates [*Bloom et al.*, 1996] to slowly converge modeled calculations toward the observations. A key feature of this global reanalysis is that it takes advantage of a variety of recent satellite observations to improve the estimates of earth's energy and water cycles. Same with NARR, MERRA spans the satellite era, from 1979 to the present. Most of the MERRA outputs are archived hourly at its native spatial grid resolution of 2/3 degree × 1/2 degree.

The radiative transfer model developed at the Goddard Climate and Radiation Branch at NASA is utilized in MERRA to generate the radiative fluxes at the top of the atmosphere (TOA) and at the surface. The shortwave radiation scheme, documented in *Chou and Suarez* [1999], resolves the absorption by water vapor, ozone, oxygen, carbon dioxide and aerosols. The longwave radiation scheme, documented in *Chou et al.* [2001], calculates the absorption by water vapor, trace gases, clouds and aerosols. A prognostic cloud scheme embedded in MERRA assumes that clouds are maximum-randomly overlapped.

2.3 Method

2.3.1 Spatial interpolation

In order to account for the spatial mismatch between modeled grids and surface observations, the reanalysis data were horizontally interpolated, using a bilinear

interpolation technique, to the measurement site from the center of the four surrounding grid cells with a weighting factor that is inversely proportional to the distance. The same technique was used by *Wild et al.* [1998] in their validation of the ECMWF reanalysis. The interpolation was done at the 3-hourly intervals for NARR and at hourly intervals for MERRA, and daily mean values were computed with the interpolated data. The interpolation should eliminate errors arising from latitudinal mismatch especially for measurement sites located near the edge of a grid cell. The slight mismatch between the interpolated model grid elevation and that of the measurement site (500 m at most) has negligible consequences and is ignored.

2.3.2 Monthly average

The space-time sampling mismatch between model products and surface measurements can cause large uncertainties in validation studies [*Rossow and Zhang*, 1995; *Zhang et al.*, 2004]. This is because surface measurements are for single points in space, whereas modeled fluxes are for the area of a grid cell. At hourly time steps, large random errors are unavoidable due to variations of cloud within the grid cell. Using longtime temporal averages to compare the cell mean and the point measurement should reduce the errors caused by the problem [*Zhang et al.*, 2004]. For this reason, we conducted the comparison using monthly averages.

The original observational data are half-hourly. We excluded outliers (daytime negative values) in the original data. In order to avoid introducing new uncertainties, we did not perform any gap filling for missing data or daytime outliers. Instead, we

excluded the day if one or more half-hourly observation was missing during the daytime and excluded the whole month if five or more days were missing in that month. (Missing nighttime values were substituted by zero.) To ensure proper comparison, we also excluded the same days to calculate the reanalyzed monthly means.

2.3.3 Dependence of bias error on clearness index

We utilized the concept of clearness index (k_t) to develop an algorithm for correcting the reanalysis bias errors. This index is defined as the ratio of global solar radiation received at the surface to the extraterrestrial radiation at the TOA (S_e) [*Gu et al.*, 1999],

$$k_t = \frac{S}{S_e}, \tag{2.1}$$

where S_e is given by

$$S_e = S_{sc}\left[1 + 0.033\cos(360t_d / 365)\right]\sin\beta, \tag{2.2}$$

In Equation 2.2, S_{sc} is the solar constant, t_d is the day of the year, and β denotes the solar elevation angle. The hourly values of S_e given by Equation 2.2 were converted into monthly means using the same method as for the reanalyzed S. The clearness index was used as an independent variable to relate with the model errors in this study.

A bias ratio (b_m) was used to measure the relative bias error, as:

$$b_m = \frac{S_m - S}{S_m}, \tag{2.3}$$

where S_m denotes the modeled solar radiation at the surface, and S denotes the observed solar radiation. Using the bias ratio rather than the actual bias non-dimensionizes the error, and helps to eliminate the possible latitudinal dependence of the bias [*Wild et al.*, 1998].

The reanalysis systems have much better performance under clear-sky conditions than under cloudy sky conditions. *Wild et al.* [1998] has demonstrated the accurate performance of the radiation scheme in ECMWF under clear-sky conditions. Similarly, MERRA is also able to calculate the clear-sky surface global radiation flux reasonably well [*Kennedy et al.*, 2011]. Under cloudy skies, both NARR and MERRA underestimate the cloud fraction [*Kennedy et al.*, 2011; *Zib et al.*, 2012], contributing to overestimation of *S*. Here we used the following simple linear equation to include the dependence of bias on sky conditions

$$b_m = a \cdot k_t + b \tag{2.4}$$

where a and b are empirical coefficients.

2.3.4 Dependence of bias error on elevation

Site elevation can also introduce model bias errors [*Frauenfeld et al.*, 2005; *A Wang and Zeng*, 2012; *P Zhao et al.*, 2007], for two reasons. First, if elevation at the model grid does not match that at the observational point, the sunlight optical path is not correctly resolved by the model, leading to underestimation or overestimation of the sunlight extinction. However, among all the observation sites chosen for this study, the elevation mismatch is at most 0.5 km, and according to the observed elevation

gradient of *S* in the eastern US [*Richardson et al.*, 2004], the resulting bias in *S* should be no greater than 2%. Second, our analysis suggests that either the lack of fully resolved orographic clouds or the bias in higher cloud liquid water path (LWP) result in increased bias errors at higher elevation sites. Empirically, this second elevation effect is captured here by modifying the coefficient *b* in Equation 2.4 to be a function of the site elevation z_e (< 5 km)

$$b = c_0 z_e^{\,2} + c_1 z_e + c_2, \tag{2.5}$$

where c_0, c_1 and c_2 are empirical coefficients.

To determine the regression coefficients in Equations 2.4 and 2.5, we first applied the geometric mean regression to Equation 2.4, using monthly data from all the calibration sites, to obtain the slope coefficient *a* separately for NARR and MERRA. Next we applied Equation 2.4 to the monthly data at individual sites with the fixed slope coefficient to determine the intercept coefficient *b*. Finally, the coefficients c_0, c_1 and c_2 in Equation 2.5 were found by regression of the site *b* value against its elevation. To avoid abnormal behavior of the quadratic curve beyond the valid data range, we set a threshold of 5 km in site elevation, beyond which *b* remains constant.

2.3.5 Post-reanalysis correction

The above set of equations cannot be used directly to correct the model bias errors because the clearness index is an unknown variable without actual measurement of the surface solar radiation. However, a solution for the corrected monthly mean *S* can be derived from Equations 2.3 and 2.4, as

$$S = \frac{(1-b)S_m S_e}{aS_m + S_e}, \tag{2.6}$$

where a is fixed for each of the two reanalysis products and b depends on the surface elevation of the model grid according to Equation 2.5. To avoid negative bias ratio, we set the thresholds for k_t as $k_t > 0.75$ for NARR and $k_t > 0.70$ for MERRA, or,

$$\frac{(1-b)S_m}{aS_m + S_e} > 0.75 \quad \text{for NARR} \tag{2.7}$$

$$\frac{(1-b)S_m}{aS_m + S_e} > 0.70 \quad \text{for MERRA} \tag{2.8}$$

No correction was conducted above these thresholds.

2.4 Results and Discussion

2.4.1 Relations of bias errors to clearness index and elevation

Sky condition is the primary factor that drives the variations of model bias error for both NARR and MERRA. Applying the regression analysis to 1253 monthly observations pooled together from the 14 calibration sites, we obtained the following empirical relationships:

$$b_m = -0.89 \cdot k_t + 0.65 \text{ for NARR} \tag{2.9}$$

$$b_m = -0.82 \cdot k_t + 0.55 \text{ for MERRA} \tag{2.10}$$

The slopes of these regression equations are large, reflecting large sensitivity to the clearness index. The sensitivity to the clearness index is slightly larger for NARR than for MERRA. The intercepts of the regression equations represent the model bias ratios under the theoretical limit of $k_t = 0$. In this limit, NARR has larger bias errors

than MERRA. These intercepts also give the upper limits of the model bias ratios. According to the regression R^2 values, the clearness index explains 62% of the variations of the bias errors in NARR and 36% in MERRA. MERRA has a smaller R^2 value than NARR, in part due to the few outliers (Figure 2.3b) which will be discussed in section 2.4.3; excluding these outliers, the R^2 would improve to 0.52.

The negative relationships shown in Figure 2.3 confirm that the model bias errors are larger under cloudy skies than under clear skies. This indicates that the NARR and MERRA model systems have poor capability of describing cloudiness. When $k_t \geq 0.7$, both reanalysis systems have bias ratios near zero. When $k_t \leq 0.2$, NARR and MERRA have bias ratios of around 0.5 and 0.4, respectively. Like other reanalysis systems, NARR and MERRA parameterize cloud with cloud microphysics packages instead of directly assimilating cloud observations. Our results suggest that these parameterizations have a tendency to underestimate cloud amount. Similarly, *Walsh et al.* [2009], *Kennedy et al.* [2011], and *Zib et al.* [2012] found that a negative bias in the modeled cloud fraction is associated with a positive bias in the reanalyzed surface solar radiation. *Wu et al.* [2012] found significant underestimation of cloud fraction (20-40%) in three reanalyses over the Southern Great Plains, USA and this underestimation is related to underestimation of other cloud properties such as cloud albedo and surface relative shortwave cloud forcing.

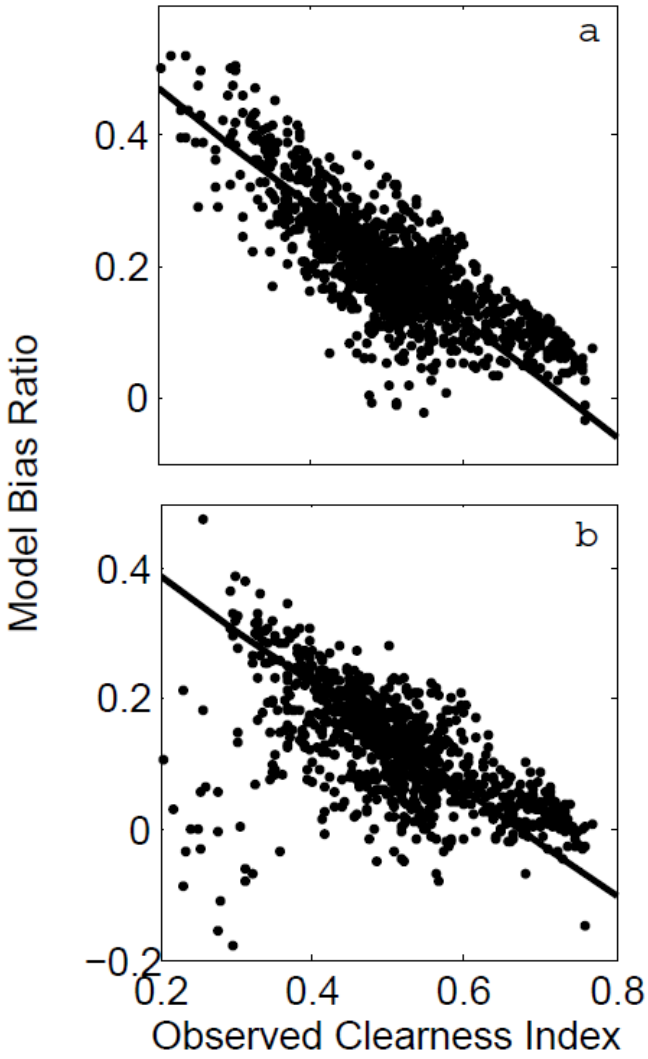

Figure 2.3 Relationship between monthly mean clearness index, S / S_e, and monthly mean model bias ratio, (S_m - S) / S_m, for the calibration sites. a: NARR, regression equation $y = -0.89 \times x + 0.65$ (R^2 = 0.62, n = 1253) b: MERRA, regression equation $y = -0.82 \times x + 0.55$ (R^2 = 0.36, n =1253).

Underestimation of the cloud liquid water path (LWP) is another possible source of error. The amount of cloud liquid water influences the reflection and absorption of shortwave radiation. *Zib et al.* [2012] found that the radiation biases still exist for some time periods despite that the observed cloud fraction is correctly reproduced by the model. *Cullather and Bosilovich* [2012] reported that MERRA cloud LWP is about 45% of that of microwave retrievals in the Arctic and this bias is consistent with biases in the surface net radiation. *M Zhao and Wang* [2010] evaluated ECMWF cloud LWP against long-term observations at Barrow, Alaska in the Arctic during 1999-2007 and found that the model on average underestimates LWP by 30 g m^{-2}. Outside of the Arctic, *Duynkerke and Teixeira* [2001] found that the ECMWF reanalysis ERA-15 strongly underestimates marine stratocumulus cloud cover and LWP off the coast of California. Similar results were found in ERA-40 by *Stevens et al.* [2007].

Figure 2.4 illustrates that the model bias errors tend to be larger at higher elevation sites. The regression equations are

$$b = -0.010 z_e^{\,2} + 0.070 z_e + 0.63 \quad \text{for NARR} \tag{2.11}$$

$$b = -0.0087 z_e^{\,2} + 0.065 z_e + 0.51 \quad \text{for MERRA} \tag{2.12}$$

In this Figure we have added the available high elevation FLUXNET validation and BSRN sites (elevation greater than 1 km). Even though the regressions were established with only two high elevation FLUXNET calibration sites, they captured the overall elevation dependence reasonably well. The choice of the quadratic fitting

function is somewhat arbitrary. Use of a linear fit function would yield similar results (Table 2.3).

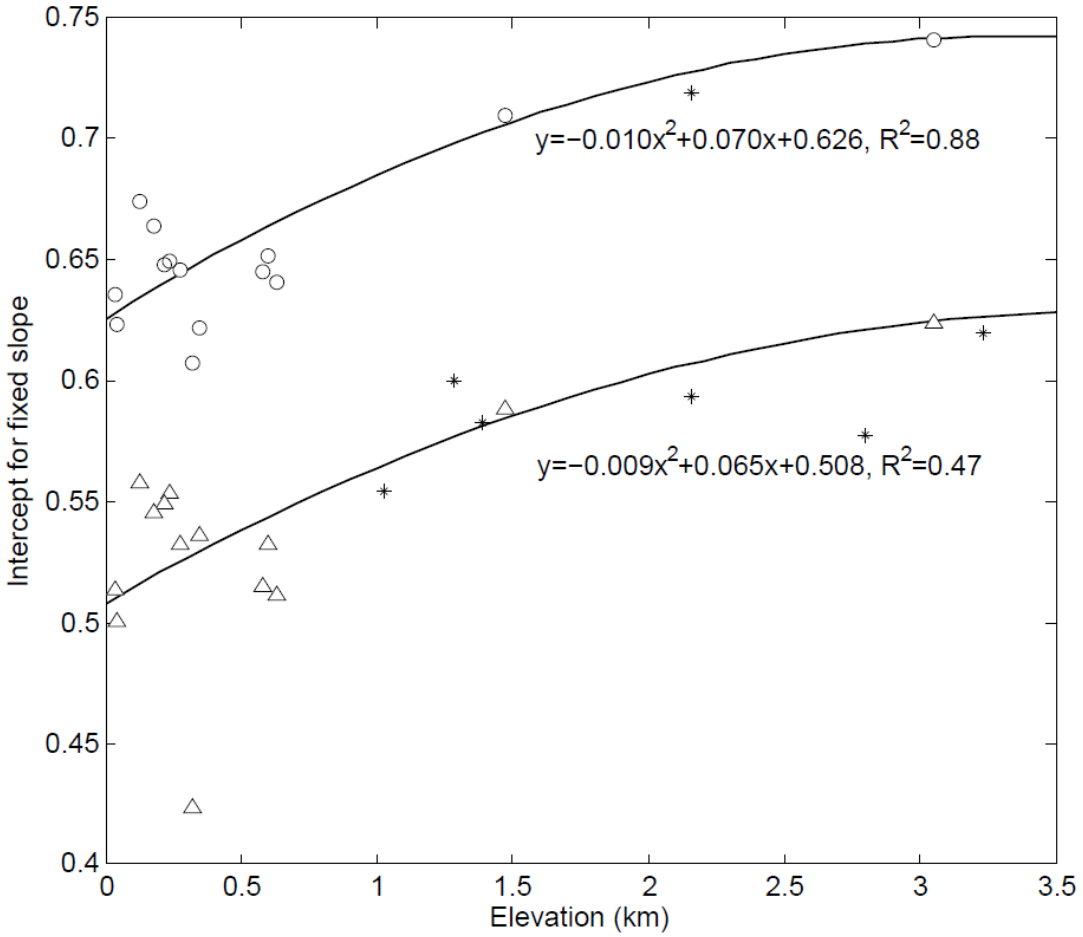

Figure 2.4 Relationship between the intercept coefficient of Equation 2.4 and the site elevation for the calibration sites. The slope coefficient of Equation 2.4 is fixed at -0.89 for NARR and -0.82 for MERRA. Circles: NARR; Triangles: MERRA; Star: available high elevation sites from BSRN and validation sites.

Table 2.3 Statistics of monthly *S* correction by quadratic fit (Equation 2.11 and 2.12) and linear fit (NARR: $b = 0.044z_e + 0.63$; MERRA: $b = 0.057z_e + 0.50$)

Site Code	NARR				MERRA			
	Quadratic fit		Linear fit		Quadratic fit		Linear fit	
	ME (Wm^{-2})	RMSE (Wm^{-2})	ME (Wm^{-2})	RMSE (Wm^{-2})	ME (Wm^{-2})	RMSE (Wm^{-2})	ME (Wm^{-2})	RMSE (Wm^{-2})
Calibration								
CA-Obs	-11.3	21.6	-7.7	19.5	1.1	16.4	3.5	17.6
CA-Ojp	-7.8	20.5	-4.5	19.4	3.1	16.8	5.4	18.3
CA-Oas	-7.7	19.5	-4.4	18.1	5.6	17.3	7.8	18.9
CA-Ca1	-9.7	19.2	-8.3	18.5	-0.3	22.2	1.5	23.2
US-UMB	6.4	17.8	7.5	18.5	7.2	13.5	9.2	14.4
CA-Cbo	4.9	19.3	5.8	19.7	10.4	17.1	12.9	19.0
US_NR1	6.4	22.0	-9.7	19.1	6.6	23.0	-20.7	25.3
US-MMS	1.5	15.6	3.1	15.9	2.5	16.3	5.2	16.8
US-Ton	9.0	22.2	9.3	22.2	-1.1	9.9	-0.4	9.7
US-Var	14.9	24.9	14.9	24.9	3.4	10.4	4.1	10.5
US-WBW	-11.9	22.9	-9.7	21.7	1.4	20.3	4.1	20.3
US-Aud	7.2	24.8	14.3	26.6	-3.2	24.4	-3.5	24.5
US_SP2	-0.6	32.4	-1.4	32.5	-2.7	34.5	-0.8	34.0
US-SP3	6.6	35.5	5.7	35.4	3.3	36.6	5.1	36.5
Average	0.6	22.7	1.1	22.3	2.7	19.9	2.4	20.6
Validation								
CA-Qfo	-17.9	21.3	-16.1	19.5	1.5	18.0	3.7	19.6
CA-Ca3	1.6	25.6	1.7	25.6	2.0	31.5	3.3	31.6
US-Ho1	-0.6	21.2	-1.2	21.1	12.9	19.3	15.1	21.5
US-Bkg	8.0	24.2	11.6	26.0	-3.0	16.5	-0.3	16.5
US-Bo1	4.5	19.3	5.5	19.6	8.3	23.5	10.9	24.5
US-Slt	19.6	31.4	18.6	30.6	12.7	18.8	14.8	20.5
US-MOz	12.0	23.5	13.1	24.3	1.5	14.0	4.2	14.3
US-Dk2	-0.6	20.5	0.0	20.6	-2.4	21.5	0.2	21.2
US-NC2	2.6	19.8	1.4	19.6	12.6	24.8	14.5	25.3
US-Fmf	0.8	23.0	4.4	24.0	-4.2	16.6	-12.6	20.0
Average	3.0	23.0	3.9	23.1	4.2	20.5	5.4	21.5

The elevation dependent-intercept brings much improvement to the algorithm for high elevation sites, regardless of the form of the fitting function for the intercept parameter. For example, at the Niwot Ridge site in Colorado (site ID, US-NR1; elevation, 3050 m), the monthly mean NARR and MERRA were biased high by 62.6 and 39.4 Wm^{-2}, respectively (Table 2.4). Using the intercepts in Equations 2.9 and 2.10 (without accounting for site-specific elevation) reduced the bias errors slightly to 61.5 and 35.7 Wm^{-2}, respectively. Using the elevation-dependent intercept parameters (Equations 2.11 and 2.12) the bias errors were reduced to 6.4 and 6.6 Wm^{-2} (Table 2.4). At a site in Tibet (elevation 4620 m, Table 2.2; [*A Wang and Zeng*, 2012]), the monthly MERRA was biased high by 19.8 Wm^{-2}. Using the correction with the intercept given in Equation 10 and with the elevation dependent intercept (Equation 2.12) reduced the bias error to 18.5 and 2.0 Wm^{-2}, respectively. With the elevation-dependent intercept, significant improvements were also seen at Audubon Research Ranch, Arizona (elevation 1469 m) and Flagstaff Managed Forest, Arizona (elevation 2160 m; Table 2.1) and at five BRNS and the literature sites with elevation >1000 m (Table 2.2).

Table 2.4 Statistics of monthly mean surface incoming solar radiation fluxes in NARR and MERRA before and after correction.

	NARR			Corrected NARR			MERRA			Corrected MERRA		
Site Code	ME (Wm^{-2})	RMSE (Wm^{-2})	R^2	ME (Wm^{-2})	RMSE (Wm^{-2})	R^2	ME (Wm^{-2})	RMSE (Wm^{-2})	R^2	ME (Wm^{-2})	RMSE (Wm^{-2})	R^2
Calibration												
CA-Obs	31.3	35.1	0.98	-11.3	21.6	0.95	20.9	28.3	0.98	1.1	16.4	0.97
CA-Ojp	32.7	37.4	0.98	-7.8	20.5	0.94	22.0	29.1	0.98	3.1	16.8	0.98
CA-Oas	32.9	37.1	0.98	-7.7	19.5	0.95	23.8	30.6	0.98	5.6	17.3	0.98
CA-Ca1	33.6	37.5	0.98	-9.7	19.2	0.95	20.5	29.9	0.98	-0.3	22.2	0.97
US-UMB	35.6	37.6	0.99	6.4	17.8	0.98	20.9	22.2	0.99	7.2	13.5	0.98
CA-Cbo	43.4	46.1	0.98	4.9	19.3	0.95	28.5	31.3	0.98	10.4	17.1	0.97
US_NR1	62.6	70.8	0.96	6.4	22.0	0.96	39.4	46.5	0.97	6.6	23.0	0.96
US-MMS	40.9	42.8	0.98	1.5	15.6	0.95	22.4	25.7	0.97	2.5	16.3	0.95
US-Ton	22.1	23.9	0.99	9.0	22.2	0.97	4.7	10.8	0.99	-1.1	9.9	0.99
US-Var	26.5	28.2	0.99	14.9	24.9	0.98	8.6	12.7	0.99	3.4	10.4	0.99
US-WBW	36.3	38.1	0.97	-11.9	22.9	0.90	23.5	26.9	0.96	1.4	20.3	0.90
US-Aud	34.9	39.8	0.94	7.2	24.8	0.94	11.1	15.2	0.98	-3.2	24.4	0.89
US_SP2	37.8	40.9	0.90	-0.6	32.4	0.63	16.7	25.8	0.84	-2.7	34.5	0.58
US-SP3	43.4	47.3	0.86	6.6	35.5	0.59	22.0	31.5	0.78	3.3	36.6	0.53
Average	36.7	40.2	0.96	0.6	22.7	0.90	20.4	26.2	0.96	2.7	19.9	0.90
Validation												

CA-Ca3	35.5	35.4	0.98	1.6	25.6	0.94	17.5	24.5	0.96	2.0	31.5	0.93
US-Ho1	37.7	43.8	0.97	-0.6	21.2	0.94	28.5	32.5	0.98	12.9	19.3	0.99
US-Bkg	35.4	40.7	0.97	8.0	24.2	0.94	12.4	20.1	0.97	-3.0	16.5	0.96
US-Bo1	39.6	43.2	0.95	4.5	19.3	0.93	23.7	30.8	0.93	8.3	23.5	0.91
US-Slt	48.5	53.0	0.98	19.6	31.4	0.96	27.6	30.5	0.98	12.7	18.8	0.97
US-MOz	39.4	41.8	0.98	12.0	23.5	0.96	16.4	19.9	0.98	1.5	14.0	0.96
US-Dk2	35.6	38.0	0.97	-0.6	20.5	0.90	15.4	19.8	0.95	-2.4	21.5	0.88
US-NC2	40.0	43.4	0.98	2.6	19.8	0.91	27.0	31.0	0.96	12.6	24.8	0.89
US-Fmf	38.5	48.9	0.87	0.8	23.0	0.96	14.7	24.0	0.94	-4.2	16.6	0.98
Average	38.1	42.4	0.96	3.0	23.0	0.94	20.8	26.7	0.96	4.2	20.5	0.95

2.4.2 Annual and monthly bias errors before and after correction

Equation 2.6 was used to obtain the corrected monthly mean *S* at both the calibration and validation sites. In this post-reanalysis correction, the coefficient *a* was -0.89 for NARR and -0.82 for MERRA, the coefficient *b* was given by Equations 2.11 and 2.12 as a function of site elevation. The algorithm reduced the annual mean bias errors from +37.2 Wm^{-2} (range 23.6 to 59.8 W m^{-2}) and +20.2 Wm^{-2} (range 6.0 to 37 W m^{-2}), which are much larger than the measurement uncertainties of 3-5 Wm^{-2}, to +1.3 Wm^{-2} (range -17.9 to 19.6 W m^{-2}) and +2.7 Wm^{-2} (range -3.9 to 16.6 W m^{-2}) for NARR and MERRA, respectively (Table 1). Figure 2.5a shows the overestimation of surface solar radiation on the annual scale in NARR and MERRA. After correction the annual mean values are evenly distributed along the 1:1 line as illustrated in Figure 2.5b.

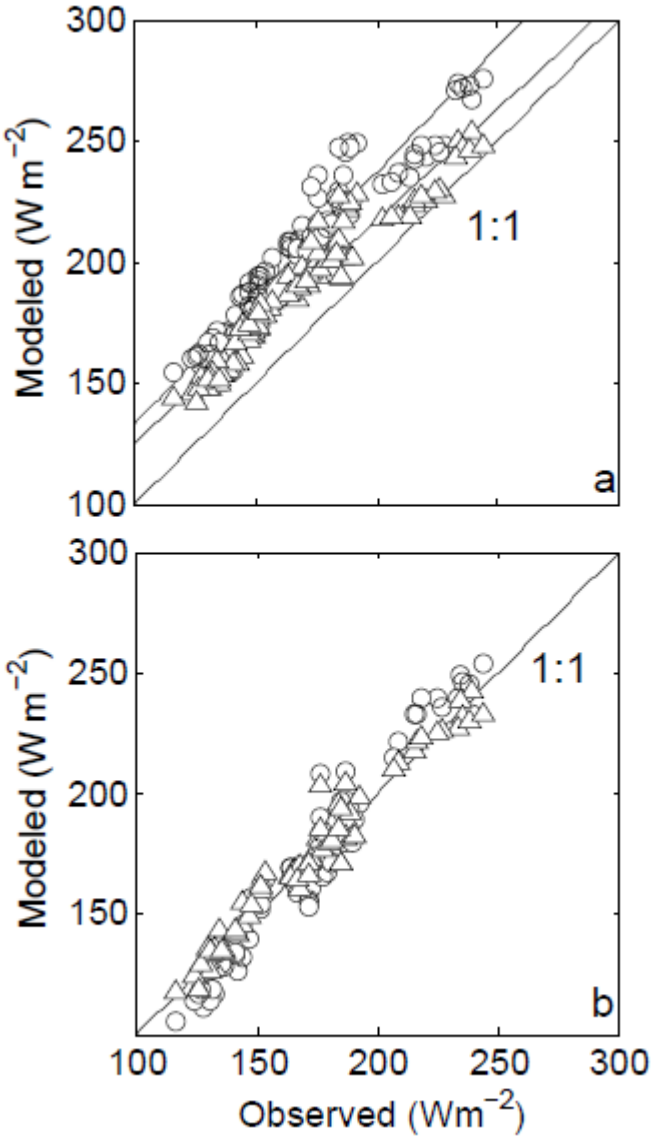

Figure 2.5 Comparison of annual mean surface incoming shortwave radiation flux at the calibration sites. a: before correction; b: after correction. Circles: NARR; Triangles: MERRA. Each data point represents an annual mean value for a site year.

The monthly statistics for the individual sites are listed in Tables 2.4. Because the data samples are slightly different, the monthly mean bias errors are not identical to the annual bias errors shown in Table 2.1. Averaging among all the sites, the correction algorithm reduced the magnitudes of both the monthly mean bias errors and RMSEs (root mean-square errors) for the two reanalyses. The values of R^2 were slightly reduced after the correction. For the calibration and the validation sites, the average R^2 were both 0.96 before correction for NARR and MERRA; after the correction, the average R^2 for the calibration sites were reduced to 0.90 for both NARR and MERRA, and for the validation sites reduced to 0.94 and 0.95, respectively. The larger reduction of the average R^2 for the calibration sites was caused by overcorrection at the two Florida sites, Mize (US-SP3) and Donaldson (US-SP2) near Gainesville. The calibration and validation sites behave very similarly in terms of the magnitudes of monthly mean bias errors, RMSE and R^2 before and after the correction, demonstrating robustness of the correction coefficients in Equations 2.6, 2.11 and 2.12.

2.4.3 Temporal and spatial variations in bias errors

The time series plots in Figure 2.6 illustrate that the corrected *S* tracked the observed interannual variabilities reasonably well at the six selected calibration sites (Old Aspen, Saskatchewan; Borden, Ontario; Morgan-Monroe State Forest, Indiana; Walker Branch, Tennessee; Donaldson, Florida; Vaira Ranch, California). These sites span a large latitudinal/longitudinal band, including both good (panels a, b, c) and one of the two worst sites (Donaldson, FL, panel e) in terms of the algorithm

performance. The monthly mean errors of the good sites were significantly reduced, with the correlation coefficients of monthly variability retained (Table 2.4), and the correlation coefficients of interannual variability were improved (Table 2.5). The two worst sites are Mize and Donaldson, both in Florida in the subtropical Mediterranean climate regime. Although the monthly mean error of Donaldson site was reduced, the correlation coefficients of monthly variability significantly decreased from 0.86 and 0.78 to 0.59 and 0.53 for NARR and MERRA, respectively.

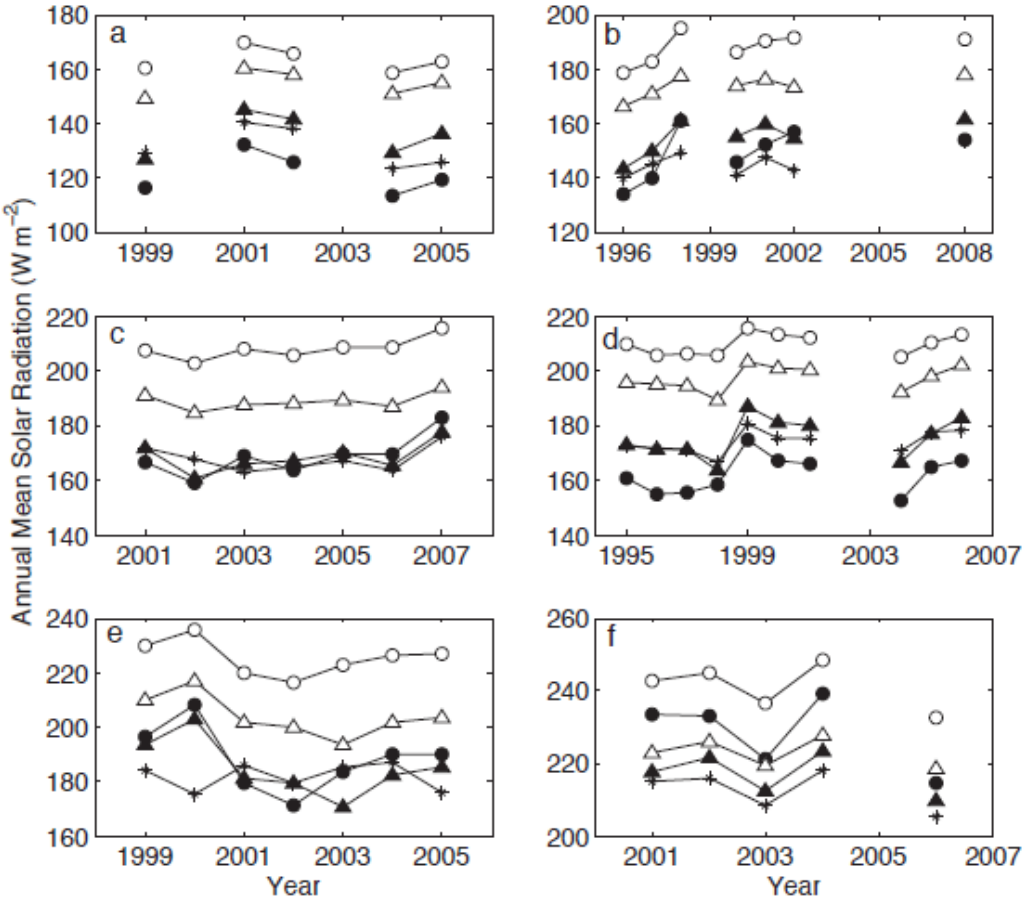

Figure 2.6 Annual mean surface incoming shortwave radiation flux at six selected sites. Open circles: NARR before correction; Black circles: NARR after correction; Open triangles: MERRA before correction; Black triangles: MERRA after correction; stars: observations. a: Old Aspen , Saskatchewan (site ID CA-Oas); b: Borden, Ontario (site ID CA-Cbo); c: Morgan-Monroe State Forest, Indiana (site ID US-MMS); d: Walker Branch, Tennessee (site ID US-WBW); e: Donaldson, Florida (site ID US-SP3); f: Vaira Ranch, California (site ID US-Var).

Table 2.5 Correlation coefficients between the modeled and the observed annual mean radiation at the calibration sites.

	R			
Site Code	NARR	Corrected NARR	MERRA	Corrected MERRA
CA-Obs	0.85	0.98	0.74	0.82
CA-Ojp	0.65	0.52	0.61	0.67
CA-Oas	0.87	0.95	0.79	0.85
CA-Ca1	0.94	0.94	0.80	0.88
US-UMB	0.90	0.91	0.95	0.96
CA-Cbo	0.83	0.79	0.85	0.90
US-NR1	0.49	0.57	0.17	0.22
US-MMS	0.59	0.61	0.41	0.79
US-Ton	0.98	0.98	0.93	0.95
US-Var	0.86	1.00	0.83	0.97
US-WBW	0.90	0.84	0.94	0.96
US-Aud	0.24	0.25	0.31	0.22
US_SP2	-0.20	0.32	-0.13	0.12
US-SP3	-0.41	-0.35	-0.51	-0.50
Average	0.61	0.67	0.55	0.63

Table 2.5 lists the correlation coefficient of the observations with the modeled annual mean *S* before and after the correction for the 14 calibration sites. (The validation sites are not listed as they do not have sufficient records for the computation of the correlation coefficient.) The two reanalysis systems generally capture the interannual variations (linear correlation $R > 0.6$), again with the two Florida sites being notable exceptions where both systems have negative correlation coefficients with the observations and the correction algorithm was unable to rectify this problem.

Averaged across all the calibration sites, the correction algorithm improved the correlation coefficient slightly by 0.06 for NARR, and 0.08 for MERRA.

Figure 2.7 illustrates the seasonal pattern of the bias errors before and after correction for the 6 selected sites as in Figure 2.6. Before correction, the seasonal cycles of bias were site-dependent. Old Aspen, Saskatchewan and Borden, Ontario had maximum bias errors in June (Figure 2.7a-b). Morgan Monroe State Forest, Indiana, Walker Branch, Tennessee, and Donaldson, Florida had peak bias errors in April (Figure 2.7c-e). Vaira Ranch, California did not have much seasonal variation (Figure 2.7f). Generally the cold season bias was smaller than the warm season errors.

After correction, the bias at the two northern sites (Old Aspen and Borden) had no obvious seasonal cycle. The algorithm overcorrected the modeled surface solar radiation in the summer at Donaldson (Figure 2.7e), and to a lesser degree at Morgan Monroe State Forest and Walker Branch (Figure 2.7c &d). At Donaldson, overcorrection caused negative monthly mean biases of up to 40 Wm^{-2} to both reanalyses. Similar magnitude of overcorrection was also found for Mize (site ID US-SP2) which is 8 km away from Donaldson. On the annual time scale, the warm season negative bias was compensated by the cold season positive bias, resulting in, fortuitously, much reduced mean bias (Table 2.4). At Vaira Ranch, our correction procedure did not bring improvements to S from May to October (Figure 2.7f). During these months, the clearness index was 0.70 - 0.75, which are beyond the k_t threshold of correction.

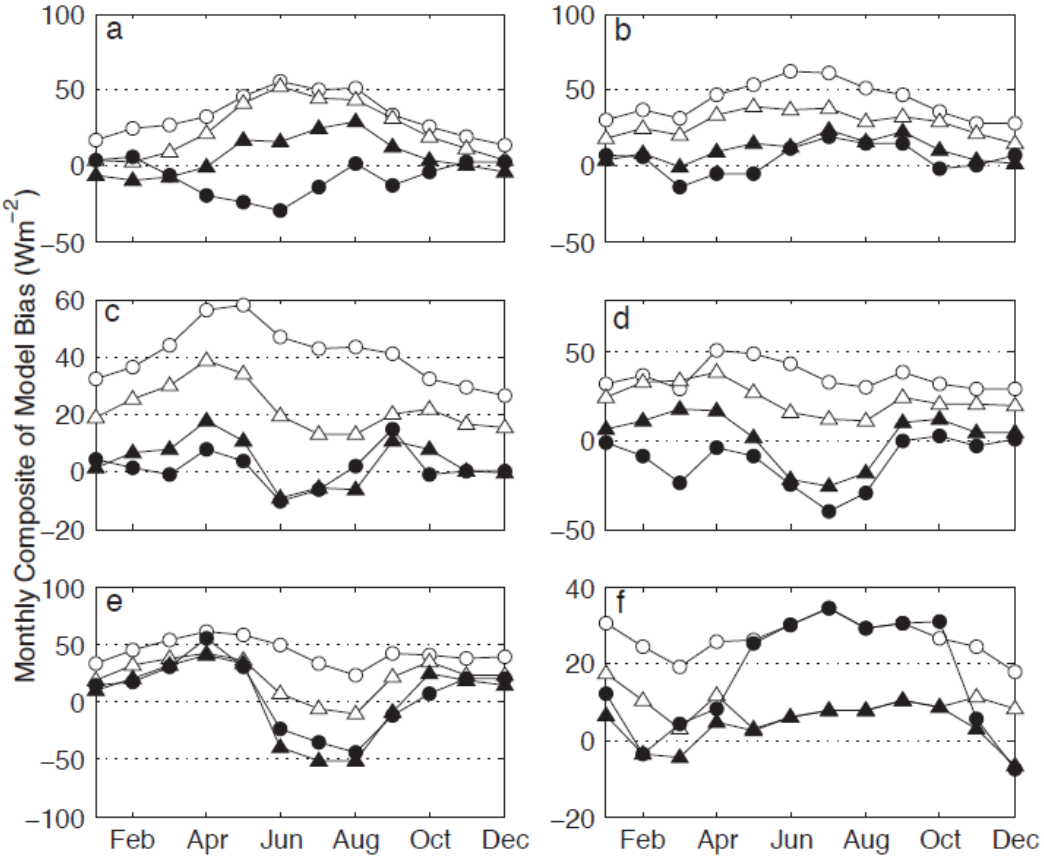

Figure 2.7 Same as Figure 2.6 except for monthly composite bias errors.

The difficulty encountered at Varia Ranch and Donaldson indicates that factors other than cloudiness and elevation also contribute to the model bias errors. Measurement errors, according to the cross-site comparison of the radiometers at these sites against an Amerflux roving standard, are too small to explain the anomalous results [*Schmidt et al.*, 2012]. A possible explanation is incorrect description of aerosols at these locations in the models, noting that even the original NARR and MERRA data fail to capture the interannual variations of *S*. Despite this limitation, our simple correction algorithm has resulted overall reduction of the RMSEs for the sites we examined (from 41.1 to 22.8 W m^{-2} for NARR and from 26.4 to 20.1 W m^{-2} for MERRA; Table 2.4).

The outliers in the left corner of Figure 2.3b came from the Douglas Fir 1949 site on Vancouver Island, British Columbia. The original MERRA data had very low and even slightly negative bias ratios. These points all came from the winter months with low monthly mean *S* (< 30 W m^{-2}; lowest among the sites we examined). Our algorithm caused slight overcorrection during these months. But the performance on the annual scale was not adversely affected, as evidenced by the large reduction of the mean bias error from 21.0 to -1.8 W m^{-2} (Table 2.1). This wintertime overcorrection was also found in Douglas Fir 1988 site, which is about 50 km away, and for the same reason, the algorithm was able to bring improvement, reducing the annual mean bias error from 17.5 to 2.0 W m^{-2} (Table 2.1).

2.4.4 Comparison between the two reanalysis products

The error structures of the two products share several similar features. The bias ratios of both reanalyses show dependence on clearness index and surface elevation (Figures 2.3 and 2.4). In addition, the two products show similar seasonal variations in the bias errors (Figure 2.7). The reasonable correlations with the observed annual mean *S* suggest the similar interannual variations in the bias errors for the two reanalyses (Figure 2.6, Table 2.5).

There are also a number of differences. In general, MERRA shows better agreement with observations than NARR (Table 2.1, Figure 2.5a). The mean errors of NARR and MERRA for all the sites were +37.3 and +20.5 Wm^{-2}, respectively, and their RMSEs were 41.1 and 26.4 Wm^{-2}, respectively (Table 2.4). The significantly positive bias in NARR likely resulted from a combination of underestimation of cloud and a lack of aerosols and water vapor in the atmospheric column [*Kennedy et al.*, 2011]. After correction, the average bias errors of NARR and MERRA for all the sites were brought down to 1.6 and 3.3 Wm^{-2}, respectively and the RMSEs were 22.8 and 20.1 Wm^{-2}, respectively.

Both uncorrected NARR and MERRA capture well the observed seasonal ($R^2 > 0.8$ for most sites) and interannual variations ($R > 0.6$ for most sites). MERRA showed no superiority compared to NARR in terms of capturing the observed seasonal and interannual variability. The correction procedure did not improve the capability of

capturing seasonal variability and improved slightly interannual variability for the two reanalysis products (Table 2.5).

2.4.5 Implication for the global radiation and energy balances

Our results indicate that MERRA overestimates the global mean *S*. In order to apply our algorithm on the global domain, examining the algorithm's performance outside of North America is required in addition to the performance evaluation done for the North American sites discussed above. Towards this goal, we selected 42 BSRN sites which have at least one year continuous *S* measurement and 8 sites from the literature (Figure 2.2 and Table 2.2). The algorithm was able to adjust the modeled annual mean *S* towards the 1:1 line for the sites both in and outside North America (Figure 2.8). Even though the algorithm was developed from the calibration sites on land, it improved the results at the BSRN ocean sites: the average bias error was 13.9 W m^{-2} before correction and -3.0 W m^{-2} after correction for these sites (Figure 2.9). Aerosol loading varies between land and ocean sites. The improvement at the ocean sites suggests that the clearness index as an independent variable has some capacity to implicitly account for the aerosol impact. For the sites outside North America, the mean bias error was 14.5 W m^{-2} before correction and -2.1 W m^{-2} after correction. Excluding the four obvious outliers, the mean bias error was 16.7 W m^{-2} and 1.3 W m^{-2} before and after correction, respectively. The four outlier sites are in the tropics (site IDs Llorin, Kwajalein, Momote and Tapajos). At these sites the original MERRA *S* matched reasonable well with the observations, and the correction

algorithm caused a low bias. If all the 12 tropical sites are considered (Table 2.2), the MERRA bias is 15.4 W m^{-2} before correction and 0.7 W m^{-2} after correction.

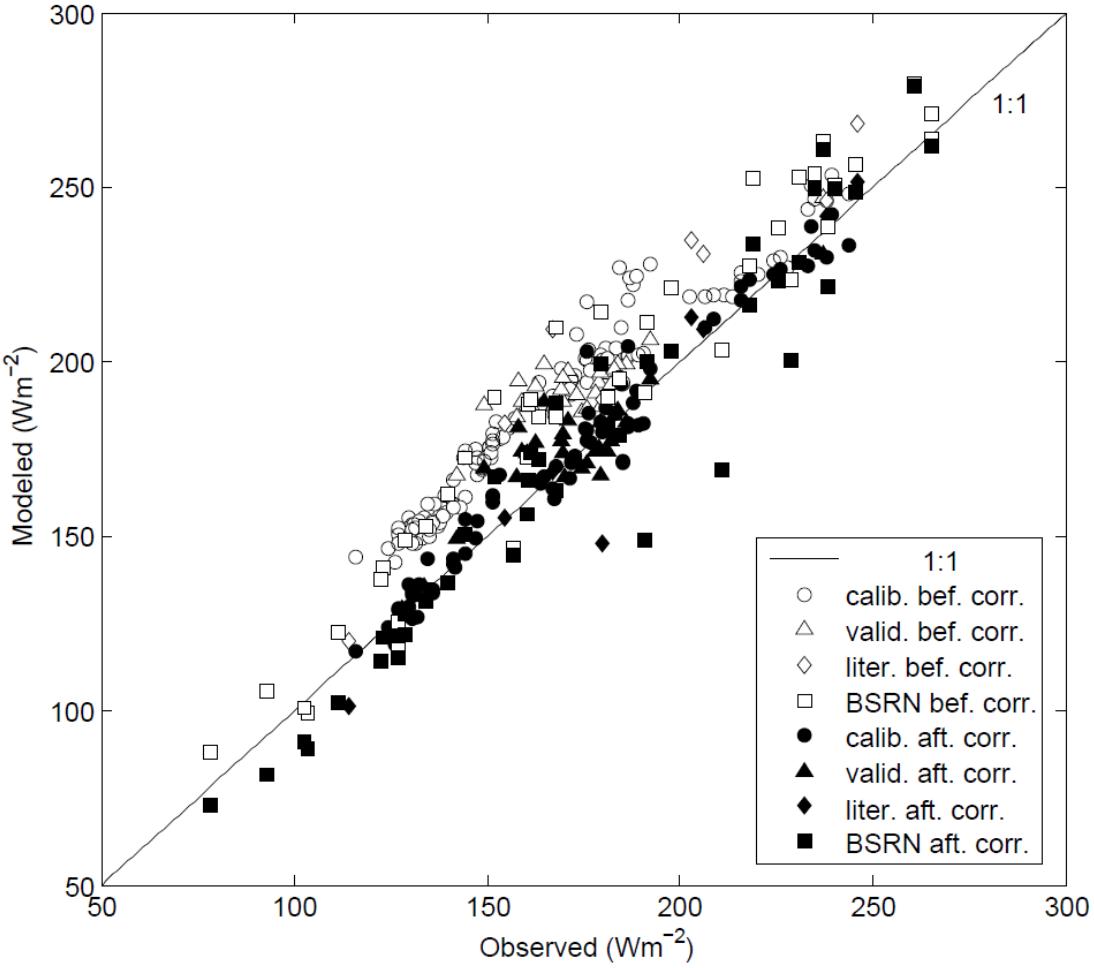

Figure 2.8 Comparison between observed and modeled annual mean surface incoming shortwave radiation flux before and after correction at the calibration, the validation, the BSRN and the sites from the literature. Each data point represents measurement at one site.

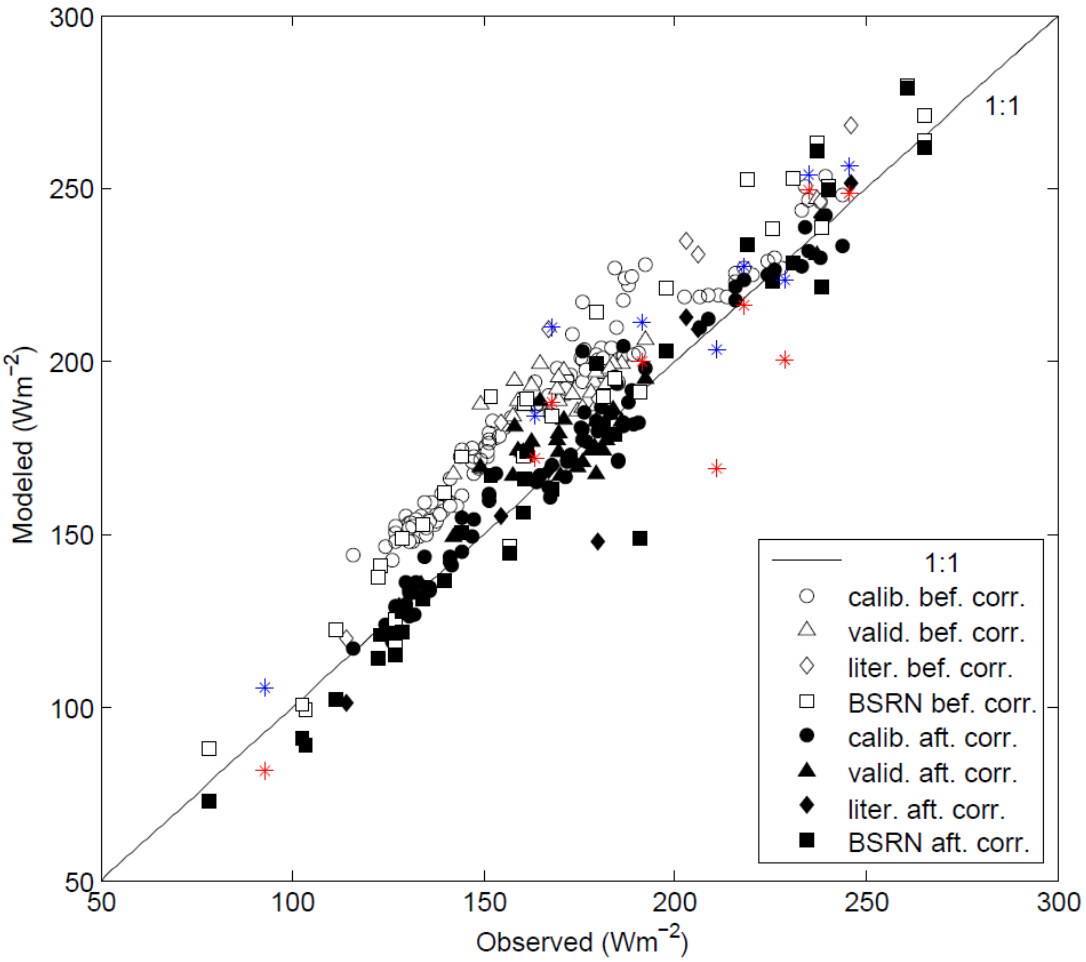

Figure 2.9 Same with Figure 2.8 Blue star: ocean sites before correction; red star: ocean sites after correction.

The reasonably good performance of the algorithm both in North America and elsewhere provides the basis of using it on the global domain. According to the default MERRA data, the global annual mean *S* is 192.8 Wm^{-2} for the year 2000 - 2004, the same years as used by *Trenberth et al.* [2009]. After correction, it was reduced to 175.5 Wm^{-2}. The default MERRA overestimates the global *S* by 17.3 Wm^{-2}.

Obviously, if *S* is adjusted in the light of this study, equivalent adjustments on other terms of the radiation and energy balances are required for energy closure. In Table 2.6, we summarize the revised global surface radiation and energy balance and compare it with the estimates of *Trenberth et al.* [2009]. Briefly, in *Trenberth et al.* [2009], the global mean *S* is an improved estimate from that of *Kiehl and Trenberth* [1997] using ISCCP-FD and CERES and with an improved calculation of the absorption by atmospheric aerosol and water vapor. Their *S* value is very close to the CERES satellite estimate (186.7 Wm^{-2}) for the period 2000-2010 [*Kato et al.*, 2013]. The global mean albedo is derived from field and satellite observations. The outgoing longwave radiation is derived from satellite observations of emissivity and the surface temperature. The sensible heat flux is the average of three reanalysis products spanning the range of 15.7 and 18.9 W m^{-2}. The latent heat flux is estimated under the assumption that precipitation is equal to global evaporation; this number is uncertain because considerable uncertainty exists in precipitation measurements, especially over the oceans. The incoming longwave radiation is computed as a residue of the surface energy balance.

Table 2.6 Comparison of two estimates of the global radiation and energy balances. Units are W m^{-2}. S: incoming solar radiation; S_u: reflected solar radiation; $L\downarrow$: incoming longwave radiation; $L\uparrow$: outgoing longwave radiation; H: surface sensible heat flux; LE: surface latent heat flux

	S	S_u	$L\downarrow$	$L\uparrow$	H	LE
Trenberth et al. (2009)	184	23	333	396	17	80
This study	175	22	344	396	20	76

In our revised depiction, the energy balance terms were estimated from independent sources independent of the energy balance constraint. The good energy balance closure (within 5 Wm^{-2}) serves as an independent confirmation that the MERRA global S value was indeed biased high. Our assessment was based on the following considerations:

- We estimated the reflected shortwave radiation by adopting the same albedo of *Trenberth et al.* [2009].
- The incoming longwave radiation $L\downarrow$ was provided by *Stephens et al.* [2012b] according to the synthesis products. These authors found a systematic underestimation of reanalyzed $L\downarrow$ and attributed the bias also to the underestimation of modeled cloudiness. Globally this underestimation is on the order of 10 Wm^{-2}.
- As for the outgoing longwave radiation, we adopted *Trenberth et al.* [2009]'s number because it is derived from observations, not from reanalysis products.
- The revised latent heat flux was an area-weighted average of a recent estimate of the terrestrial [*Mu et al.*, 2011] and the ocean latent heat flux [*Yu et al.*,

2008]. *Mu et al.* [2011] provides a global land surface evaportransporation dataset over 2000-2006 based on MODIS and a global meteorological reanalysis, which has been validated at 46 Ameriflux tower sites. The ocean dataset provides multi-decadal estimates of air-sea fluxes over global oceans using bulk transfer formulation. (Here we used the ocean flux data from 2000 to 2004, the same period as our *S* estimate.) The global mean latent heat flux is insensitive to uncertainties in the land evaporation estimates and is largely determined by the ocean value. Replacing *Mu et al.'s* [2011] land value by *Jung et al.'s* [2011] value (39 W m^{-2}) changes the global latent heat flux slightly, to 76.5 W m^{-2}. Similarly, there is a relatively large spread among a variety of the land latent heat flux products examined by *Jimenez et al.* [2011]; When combined with the ocean flux of *Yu et al.* [2008], the resulting global mean value lies in a very narrow range of 75.2 – 77.0 W m^{-2}.

- Similarly, the revised estimate of sensible heat flux was a combination of the land [*Jung et al.*, 2011] and the ocean flux [*Yu et al.*, 2008]. *Jung et al.* [2011] applied a machine learning technique - model tree ensembles to upscale FLUXNET observations to the global scale from 1982 to 2008. We adopted their long-term mean value of the terrestrial sensible heat flux.

The downward adjustment in *S* is mostly compensated by an upward adjustment of the incoming longwave radiation by a similar amount. A recent study by [*Stephens et al.*, 2012a] suggests that much of the extra incoming longwave radiation (as compared to Trenberth's assessment) to the surface is offset by more latent heat flux from the surface. Our study suggests an alternative hypothesis that the compensation

exists between S and $L\downarrow$without the need to adjust the other energy balance terms significantly.

2.5 Conclusion

In this study, the surface incoming shortwave radiation S modeled by two data assimilation systems, NARR and MERRA, was evaluated against observations from 24 FLUXNET sites in the US and Canada at multiple time scales. NARR and MERRA systematically overestimated the surface solar radiation flux on both monthly and annual scales. Their bias errors were larger under cloudy skies than under clear skies and increased with increasing elevation. The two products show similar capability to reproduce the seasonal and interannual variations of S, and similar seasonal variations in the bias errors. MERRA generally shows better agreement than NARR with the flux tower measurements.

A simple post-reanalysis correction algorithm was proposed on the basis of the dependence of the bias on sky clearness and surface elevation. Results show that the correction algorithm worked well on the annual scale for the FLUXNET sites in North America; it reduced the annual mean bias errors from +37.2 Wm^{-2} and +20.2 Wm^{-2} to +1.3 Wm^{-2} and +2.7 Wm^{-2} for NARR and MERRA, respectively. The algorithm slightly improved the modeled interannual variability for the two products. The algorithm showed good performance as well for sites outside North America except for 4 tropical sites.

There are a few limitations to this algorithm. The algorithm overcorrected *S* in Florida in the summer and the annual mean *S* at 4 sites near the equator. But this simple algorithm was able to reduce the overall mean bias errors and the RMSEs of the sites considered.

The global mean S was 192.8 W m^{-2} for 2000 to 2004 according to MERRA. The correction algorithm reduced it by 9.0% to 175.5 W m^{-2}. This corrected *S* is 12.5 and 8.8 W m^{-2} lower than that given by *Stephens et al.* [2012a] and *Trenberth et al.* [2009]. It appears that various modeled products likely have similar problems in underestimating the atmospheric absorption of shortwave radiation.

Chapter 3 Urban heat islands in current climate

Published as Zhao, L., X. Lee, R. B. Smith, and K. Oleson (2014), Strong contributions of local background climate to urban heat islands, *Nature, 511*(7508), 216-219, doi:10.1038/nature13462.

Summary

Urban heat island (UHI), the ubiquitous phenomenon of higher surface temperature in urban buildup land than that of its surrounding, represents one of the most significant human-induced changes to the earth's surface climate [*Kalnay and Cai*, 2003; *Zhou et al.*, 2004]. Even though they are localized hot spots in the landscape, these islands have profound impact on the lives of urban residents who comprise more than 50% of the world's population [*Grimm et al.*, 2008]. A barrier to UHI mitigation is the lack of quantitative attribution of various factors contributing to the intensity of UHI (ΔT, temperature of urban center minus rural temperature) [*Voogt and Oke*, 2003]. A common perception is that reduction in evaporative cooling in urban land is the dominant driver of ΔT [*Taha*, 1997]. Here we perform a factor separation analysis of surface radiative temperature with a climate model to show that, for cities across North America, variations in daytime ΔT are largely explained by variations in convection efficiency (associated with aerodynamic resistance) between urban and nonurban land. If urban areas are aerodynamically smoother than surrounding rural areas, urban heat dissipation is relatively less efficient and urban warming occurs (and vice versa). This convection effect depends on local background climate, increasing daytime ΔT by 3.0 ± 0.3 K (mean and standard error) in humid climates but decreasing ΔT by 1.5 ± 0.2 K in dry climates. In the humid eastern United States, there is evidence of higher ΔT in drier years. These relationships imply that UHIs will exacerbate heatwave stress on human health in wet climates where high temperature effects are already compounded by high air humidity [*Fischer and Schar*, 2010; *Smith et al.*, 2013] and in drier years when positive temperature anomalies may be

reinforced by a precipitation-temperature feedback [*Schar et al.*, 2004]. Results also support albedo management as a viable means of reducing ΔT on large scales [*Akbari et al.*, 2009; *Georgescu et al.*, 2013].

3.1 Background

The conversion of natural to urban land causes several notable perturbations to the surface energy balance. Reduction of evaporative cooling is generally thought to be the dominant factor contributing to UHI. Anthropogenic heat release is an added energy input to the energy balance and should increase the surface temperature. Energy input via radiation will also increase if albedo is reduced in the process of land conversion. Buildings and other artificial materials can store more radiation energy in the daytime than natural vegetation and soil; release of the stored energy at night contributes to nighttime UHI. Finally, energy redistribution through convection between the surface and the atmospheric boundary layer can either increase or reduce ΔT, depending on whether the efficiency of convection in urban land is suppressed or enhanced in reference to the adjacent nonurban land. Although these concepts have been known for some time[*Arnfield*, 2003; *S Grimmond*, 2007; *Oke*, 1982], a quantitative understanding of their contributions to UHI across different climate regimes still remains elusive[*Voogt and Oke*, 2003].

A number of recent modeling studies on UHIs are primarily on the scale of a few days [*Li and Bou-Zeid*, 2013; *Li et al.*, 2014; *Oleson et al.*, 2008b]. Few studies were conducted to model the UHIs on the scale of climate. The UHI that we investigated in

this dissertation is in the context of climatology, rather than a synoptic event of a few days.

From the previous chapter, we have learned that MERRA and NARR have systematic high bias in surface incoming solar radiation. It appears that various modeled products likely have similar problems in overestimating the surface incoming solar radiation. Therefore, the reanalysis data cannot be directly used to drive the land surface model before certain corrections. We chose to use a carefully revised reanalysis climatology based on surface observations [*Qian et al.*, 2006] as the model forcing data. This dataset significantly reduced the high bias of the surface incoming solar radiation in the original reanalysis. In addition, it also corrected other variables that would be used to drive the land surface model including precipitation, air temperature, and surface specific humidity.

3.2 Results and discussion

3.2.1 Geographic pattern over North America

The climatic context can be understood by posing the following question in a thought experiment: if two cities are built identically in terms of morphological and anthropogenic aspects but in different climates, will they have the same ΔT? The answer depends on time of the day according to the MODIS satellite observations of the surface temperature. For 65 selected cities in North America, the annual mean midnight ΔT (surface temperature of urban core pixels minus that of rural pixels) is positively correlated with the logarithm of population (correlation coefficient r = 0.54, confidence level $p < 0.001$; Figure 3.1d), but is invariant with climate, showing statistically insignificant correlation with precipitation ($r = 0.05$, $p = 0.70$; Figure 3.2), solar radiation ($r = 0.15$, $p > 0.20$) and air temperature ($r = 0.20$, $p > 0.10$). On the other hand, the annual mean midday ΔT is strongly correlated with precipitation ($r = 0.74$, $p < 0.001$, Figure 3.1b) and has a weaker statistical dependence on population size than the nighttime ΔT ($r = 0.27$, $p = 0.027$; Figure 3.2). The nighttime ΔT shows little spatial coherence (Figure 3.1c), but the daytime ΔT has a discernible spatial pattern that follows precipitation gradients across the continent (Figure 3.1a). Twenty-four of the cities are located in the humid southeast United States, which coincides roughly with the Köppen-Geiger temperate climate zone (Figure 3.3a). Their daytime annual mean ΔT is on average 3.9 K and is 3.3 K higher than that of the 15 cities in the dry region (Figure 3.3e and 3.3d). For comparison, the nighttime ΔT differs by 0.1 K between the two groups (Figures 3.3f and 3.3g, $p > 0.60$). These results are in broad agreement with previous remote sensing studies on UHI across

biophysical and developmental gradients [*Clinton and Gong*, 2013; *Imhoff et al.*, 2010; *Peng et al.*, 2012; *Roth et al.*, 1989].

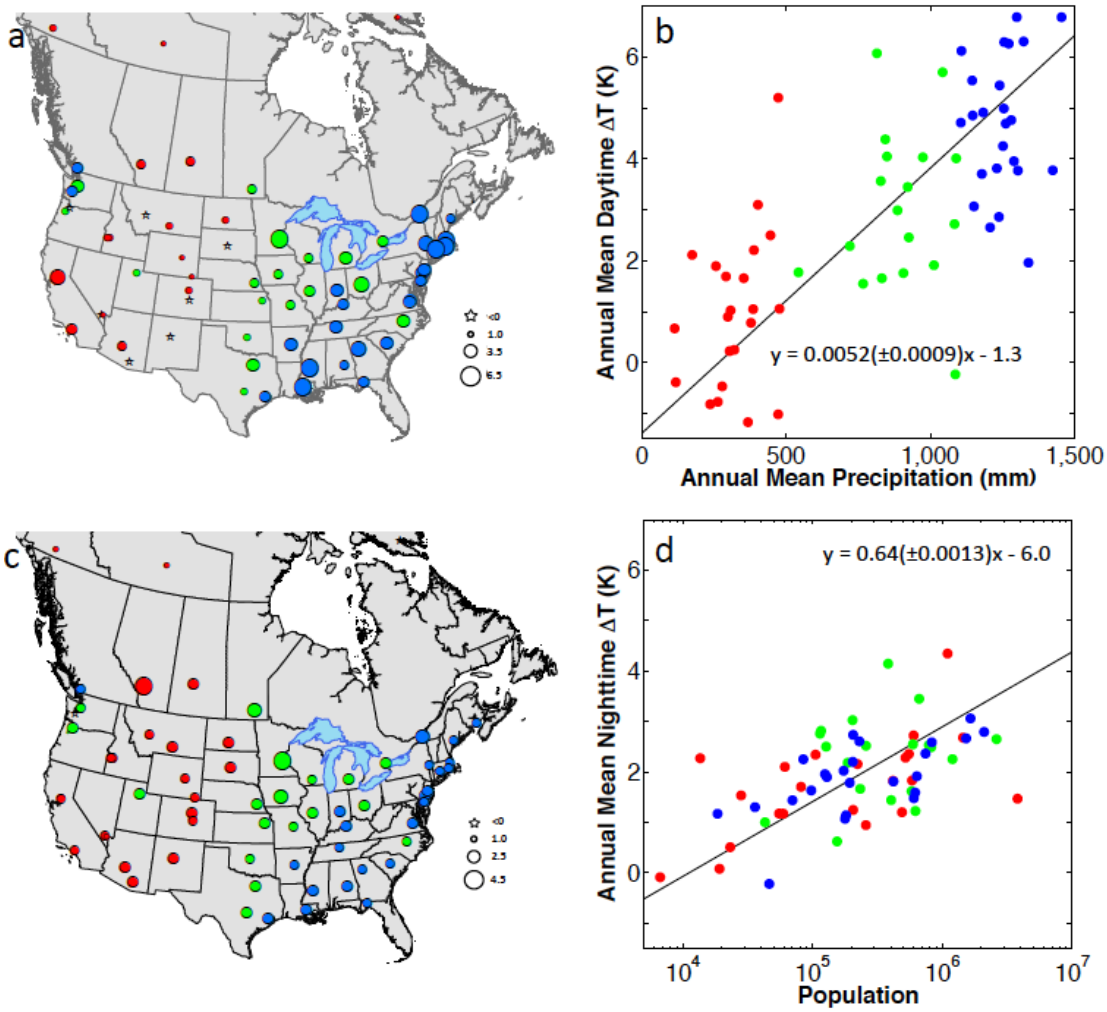

Figure 3.1 Precipitation and population influences on MODIS-derived annual mean UHI intensity. **a**, map of daytime UHI. **b**, dependence of daytime UHI on precipitation ($r = 0.74$, $p < 0.001$). **c**, map of nighttime UHI. **d**, dependence of nighttime UHI on population ($r = 0.54$, $p < 0.001$). Red, green and blue symbols denote cities with annual mean precipitation less than 500 mm, between 500 and 1100 mm and over 1100 mm, respectively. Lines in panels **b** and **d** are linear regression fit to the data.

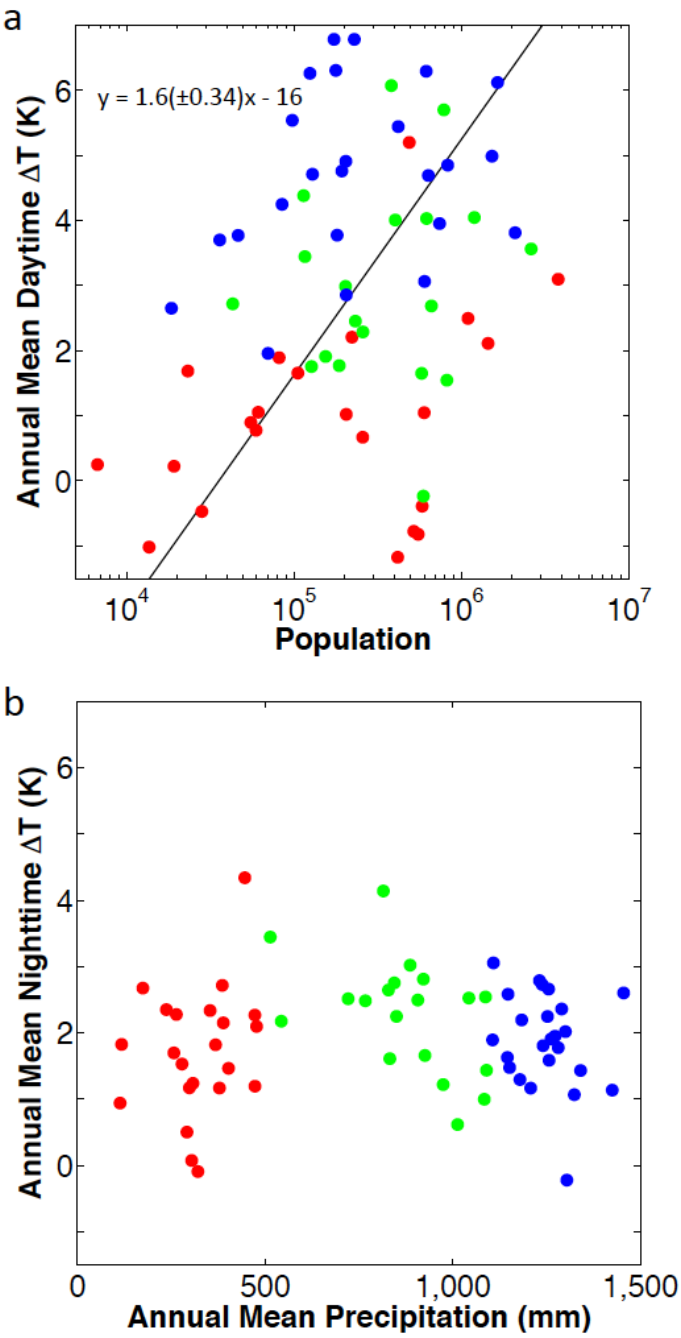

Figure 3.2: Precipitation and population influences on MODIS-derived annual mean UHI intensity. a, Dependence of daytime UHI on population size (r = 0.27, p = 0.027). b, Dependence of nighttime UHI on precipitation (r = 0.05, p = 0.70). Red, green and blue symbols denote cities with annual mean precipitation less than 500 mm, between 500 and 1100 mm and over 1100 mm, respectively. The solid line in panel a is the linear regression fit to the data.

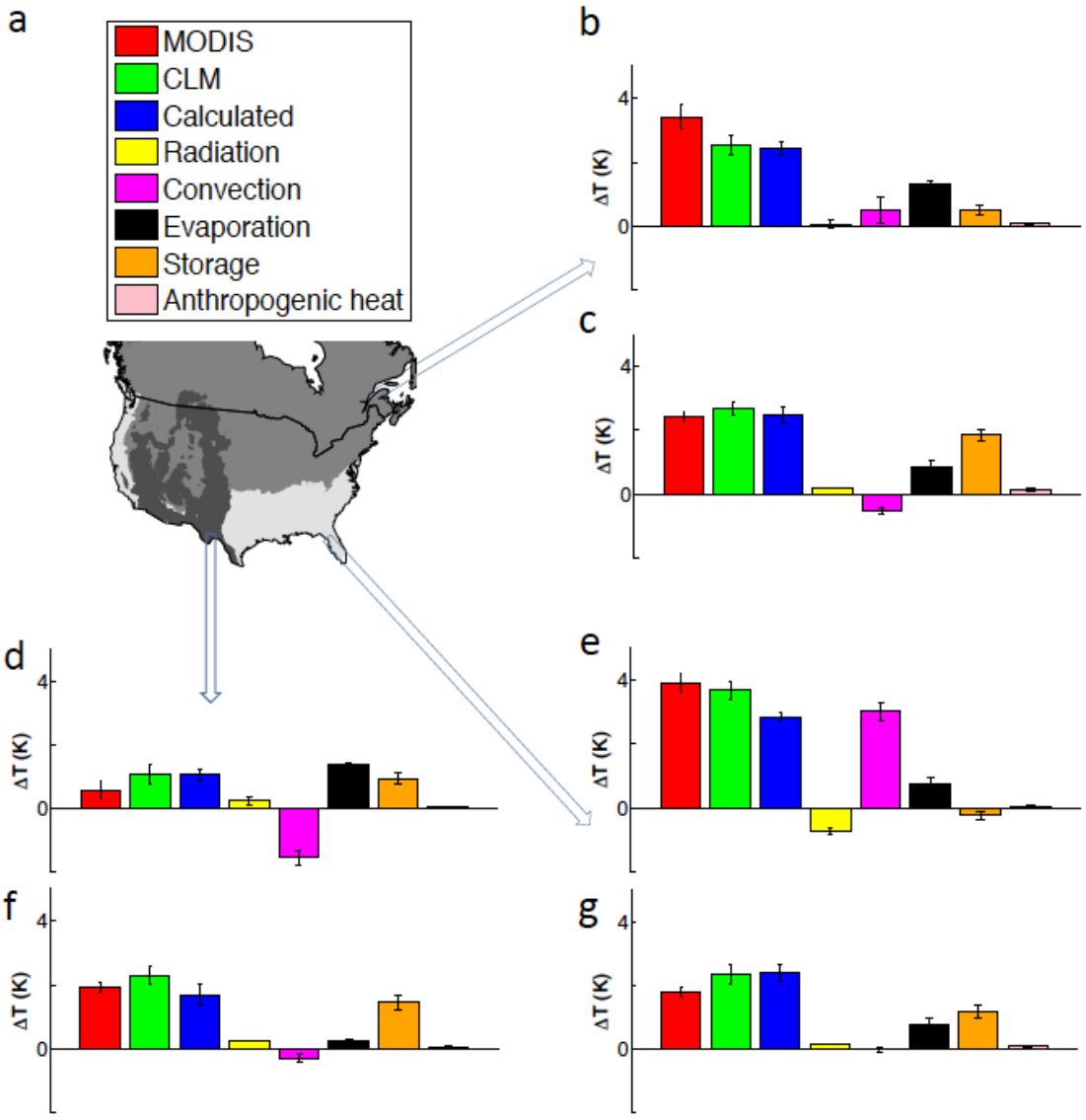

Figure 3.3 Attribution of UHI intensity in three Köppen-Geiger climate zones. **a**, map of climate zones: white, mild temperate/mesothermal climate; grey, continental /microthermal climate; dark grey, dry climate. **b**, **d** and **e**, daytime values of MODIS and modeled ΔT and its component contributions. **c**, **f** and **g**, nighttime values. Green bars denote model-predicted ΔT and blue bars denote UHI intensity calculated as the sum of the component contributions. Error bars are 1 s. e. for each climate zone.

3.2.2 Contributions of biophysical processes

At first glance, the relationship with precipitation (Figure 3.1b) seems consistent with the hypothesis that reduction in evaporative cooling in urban land is the main driver of daytime ΔT, as the denser vegetation in wet climate regions has higher evaporation rate than the vegetation in dry climates. However, our model-based intrinsic biophysical mechanism analysis does not support such interpretation. In the model domain, ΔT is a perturbation signal to the surface temperature caused by biophysical contrast between nonurban and urban land units in the same model gridcell [*Oleson*, 2012]. This signal is further decomposed, using the method described in *Lee et al.* [2011], into contributions from changes in radiation balance, evaporation, convection efficiency and heat storage, and from anthropogenic heat addition (Figure 3.3). The credibility of the model is supported by the reasonable agreement of the modeled ΔT with the MODIS ΔT ($r = 0.31$, $p < 0.02$ for daytime and $r = 0.30$, $p < 0.025$ for nighttime) and by the successful depiction of a nighttime ΔT versus albedo relation (Figure 3.4). Furthermore, the model has reproduced the observed positive correlation between the daytime ΔT and precipitation (Figure 3.5a).

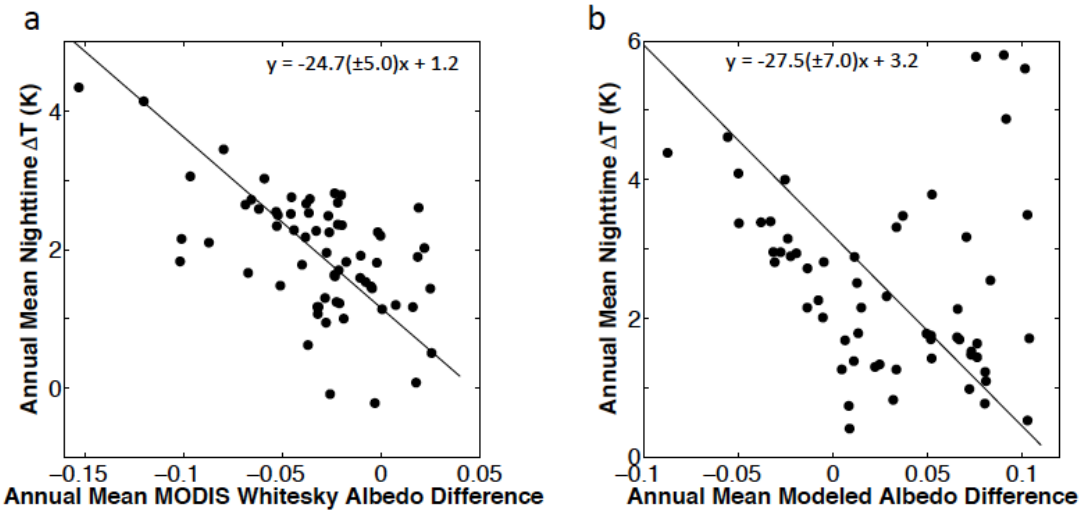

Figure 3.4: Albedo influence on annual mean nighttime UHI intensity. **a**, Dependence of nighttime MODIS-derived UHI on white-sky albedo difference (= urban albedo minus rural albedo; r = -0.60, $p < 0.001$). **b**, Dependence of nighttime modeled UHI on modeled albedo difference (r = -0.56, $p < 0.001$ excluding four outliers; r = -0.18, p = 0.16 with all data points). The four outliers in the upper right corner of panel **b** are coastal cities (Olympia, Washington; Seattle, Washington; Salem, Oregon; Vancouver, British Columbia) that have high biases of the modeled ΔT compared to the MODIS ΔT. Lines are linear regression fit to the data

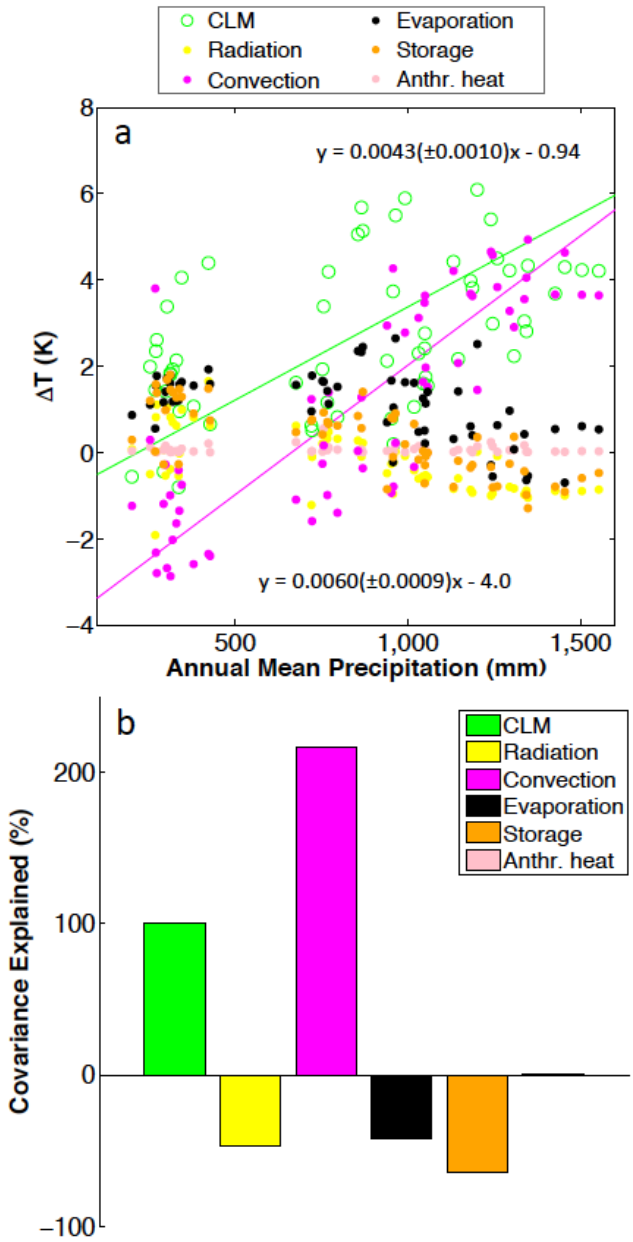

Figure 3.5 Relationship between model-predicted daytime ΔT and precipitation among the cities. **a**, Correlation of ΔT and the individual biophysical components with annual mean precipitation. Lines are linear regression fit to the corresponding data. **b**, ΔT – precipitation covariance explained by different biophysical factors. Note that the covariance explained by the anthropogenic heat term is negligibly small.

We find that it is the changes in convection efficiency associated with aerodynamic resistance change rather than in evapotranspiration that control the daytime ΔT-precipitation spatial covariance among the cities (Figure 3.5). In the humid climate (the Köppen-Geiger temperate/mesothermal zone), convection is less efficient at dissipating heat from urban land than from natural land, and the associated temperature increase is 3.0 $\pm$ 0.3 K, which dominates the overall ΔT (Figure 3.3e). At these locations, the nonurban land is in general densely vegetated, thanks to ample precipitation, and is aerodynamically rough. Quantitatively, this difference is manifested in a lower aerodynamic resistance to sensible heat diffusion in the nonurban (39 s m^{-1}) than the urban land (62 s m^{-1}). Measured with the scale of aerodynamic resistance, urbanization has reduced the convection efficiency by 58%.

The opposite occurs in the dry climate zone where urban land is rougher than non-urban land and has enhanced convection efficiency. The result is actually a cooling effect (Figure 3.3d). In this zone, the urban landscape has lower aerodynamic resistance (53 s m^{-1}) than the adjacent nonurban land (66 s m^{-1}) which is typically inhabited by vegetation of low stature such as shrubs, sagebrushes and grasses. On average, the urban land is about 20% more efficient in removing heat from the surface by convection than the nonurban land. The average cooling signal is -1.5 ± 0.2 K. In a few of the cities, convection is much more efficient than in the surrounding natural land so that ΔT becomes negative (Figures 3.1a and 3.5a). It has been suggested that negative ΔT, a phenomenon known as “urban heat sink”, arises

from evaporative cooling of trees and lawns planted in the city [*Clinton and Gong*, 2013; *Imhoff et al.*, 2010; *Peng et al.*, 2012]. Our explanation seems more logical, because the MODIS urban temperature comes from the urban core pixels with negligible amounts of vegetation cover (enhanced vegetation index < 0.18) and the urban land unit in the climate model is completely free of vegetation. An analogous situation exists in a semi-arid plantation forest where trees serve as efficient "heat convectors" leading to a lower surface temperature than in the adjacent smoother shrub land [*Rotenberg and Yakir*, 2010].

At night, release of the stored heat is the dominant contributor to ΔT across all three climate zones (Figures 3.3c, 3.3f and 3.3g). The dependence on population size (Figure 3.1d), which is an indicator of the city's horizontal dimension, can be understood in light of these results. At night, the released heat is trapped in a very shallow atmospheric boundary layer. As air moves across the urban airshed, it will accumulate more heat with increasing travel distance. Having a longer upwind fetch, the center of a larger city should experience stronger warming [*Oke*, 1982]. We note that the climate model cannot explicitly capture population dependence because population size is not a model parameter and the heat advection occurs at subgrid scales not resolved by its one-dimensional parameterization of land-atmosphere interactions.

3.2.3 Inter-annual variability of ΔT

There is some evidence of precipitation control on interannual variability in the daytime ΔT for individual cities. For each city, we have calculated the linear regression slope of the annual daytime ΔT against the annual precipitation and refer to it as temporal sensitivity to precipitation. Both the MODIS and the model data show a negative dependence of the sensitivity on site mean precipitation (Figure 3.6b and 3.6d). Twenty-four cities have annual mean precipitation exceeding 1100 mm. According to the model, 100% of these cities, which are mostly distributed in eastern United States, have negative temporal sensitivity (Figure 3.6c), meaning higher ΔT in drier years. The mean temporal sensitivity of this group of cities is -0.0021 K/mm. The MODIS results are less consistent due to shorter data records, showing negative sensitivity for 42% of them (Figures 3.6a and 3.6b).

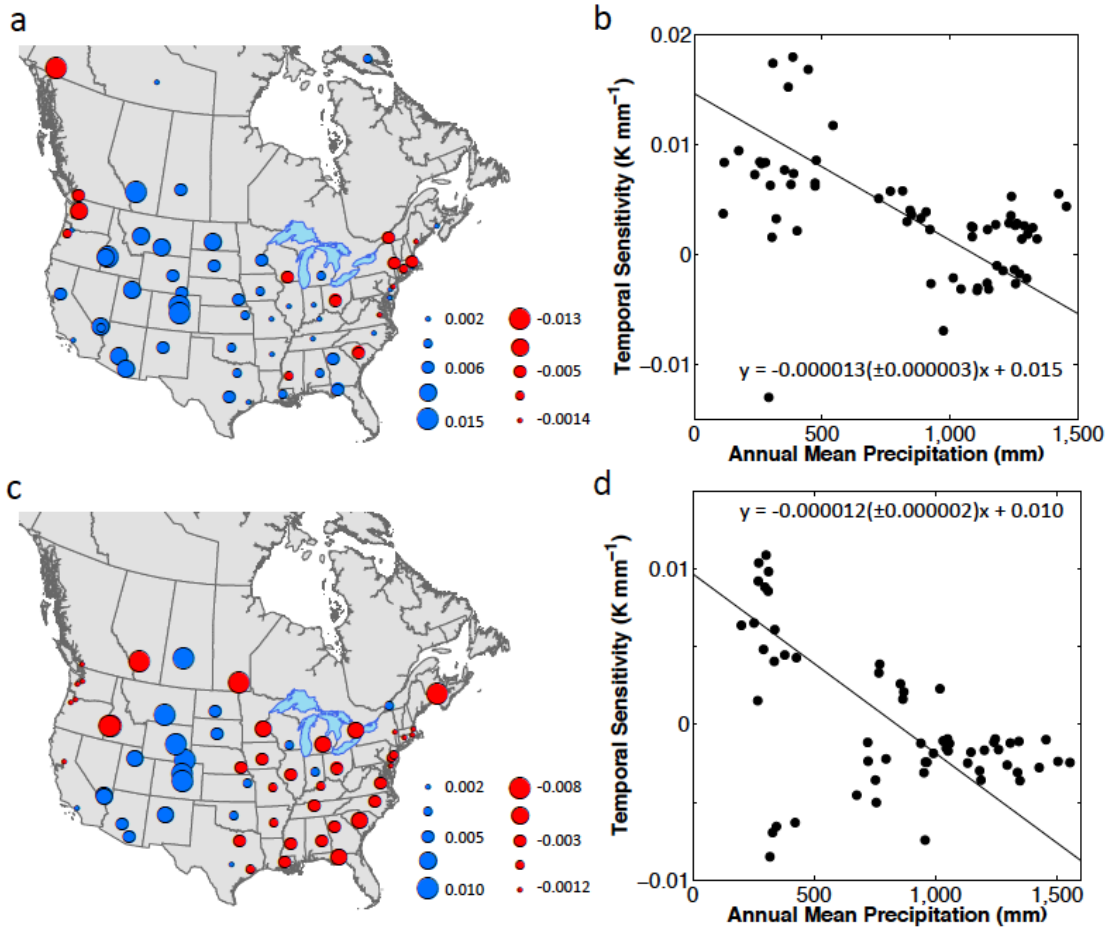

Figure 3.6. Temporal sensitivity of UHI intensity to precipitation. **a** and **c**, Map of the temporal sensitivities according to MODIS and the climate model, respectively. **b** and **d**, Dependence of MODIS and model-predicted temporal sensitivity on annual mean precipitation, respectively. The outlier city in the MODIS panels is Whitehorse, Yukon. The four outlier cities in the model panels are Boise and Nampa in Idaho, Winnipeg in Manitoba and Calgary in Alberta. Lines in panels **b** and **d** are linear regression fit to the data.

In order to gain further insights into the interannual variability, we have compared the daytime ΔT-precipitation correlation for Billings in Montana (annual mean precipitation 353 mm) and Richmond in Virginia (1183 mm). We choose these two cities because they have nearly the same morphological and biophysical specifications (Table 3.1) and therefore are essentially identical in the model world. The sensitivity to precipitation is positive at Billings and negative at Richmond (Figure 3.7). In contrast to the spatial variations across the continent (Figure 3.5b), the ΔT interannual variability shown here is driven primarily by changes in surface evaporation (Figure 3.8).

Table 3.1: Urban parameters of a city pair in CLM

City	Richmond	Billings
State	Virginia	Montana
Latitude (^{o})	37.53	45.79
Longitude (^{o})	-77.42	-108.54
Canyon Height/Width	0.48	0.48
Mean building height (m)	12	12
Roof thickness (m)	0.15	0.15
Wall thickness (m)	0.28	0.28
Wind height in canyon (m)	6	6
Roof fraction	0.55	0.50
Pervious road fraction	0.66	0.64
Emissivity (Impervious road)	0.91	0.91
Emissivity (pervious road)	0.95	0.95
Emissivity (roof)	0.65	0.65
Emissivity (wall)	0.91	0.91
Albedo (Impervious road)	0.13	0.13
Albedo (pervious road)	0.08	0.08
Albedo (roof)	0.30	0.30
Albedo (wall)	0.34	0.34
Roof thermal conductivity (W m^{-1} K^{-1})	0.84	0.84
Wall thermal conductivity (W m^{-1} K^{-1})	1.06	1.06
Impervious road thermal conductivity (W m^{-1} K^{-1})	1.67	1.67
Layers of impervious road	2	2
Roof heat capacity (MJ m^{-3} K^{-1})	0.76	0.76
Wall heat capacity (MJ m^{-3} K^{-1})	0.81	0.81
Impervious road heat capacity (MJ m^{-3} K^{-1})	2.06	2.06

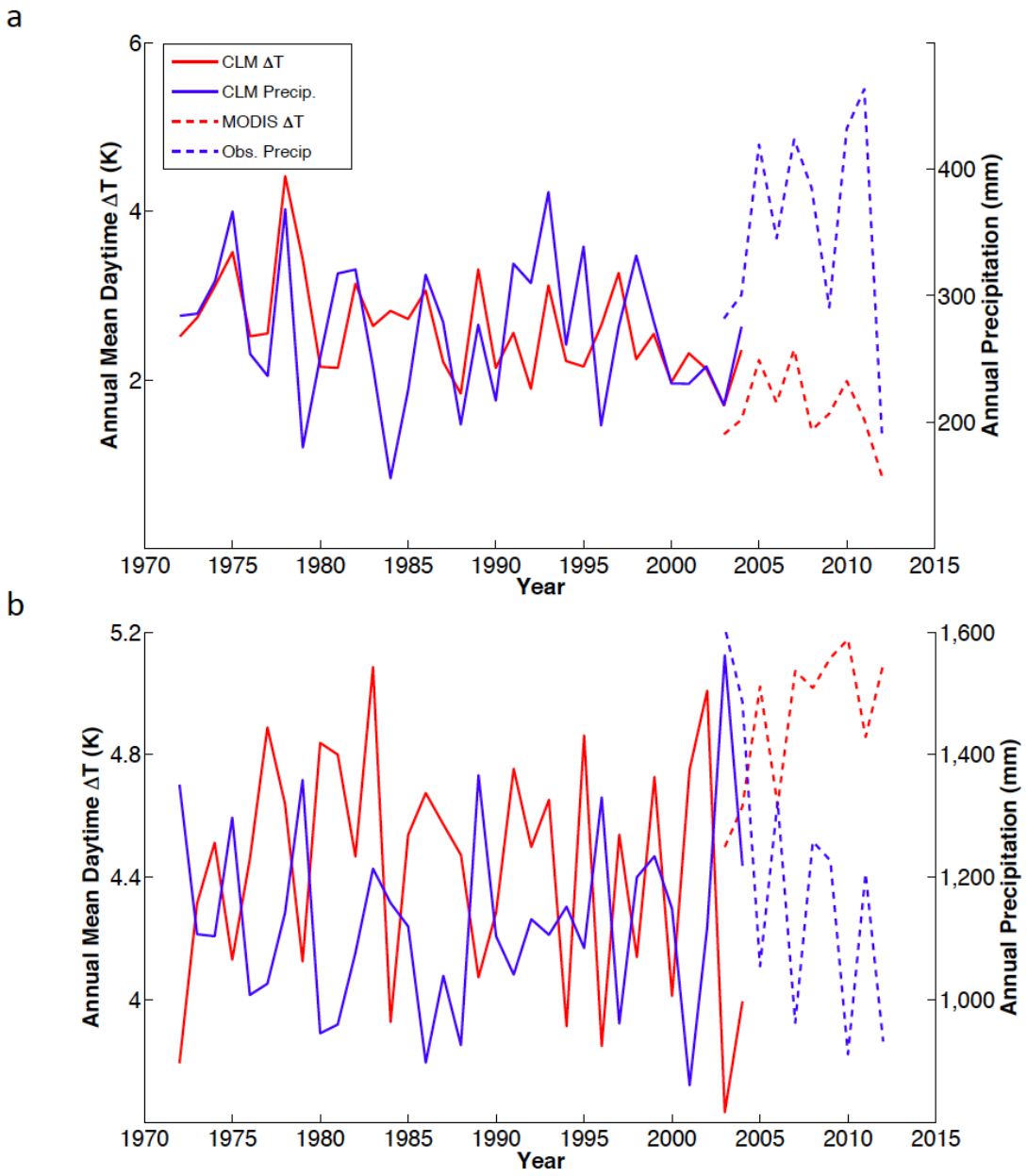

Figure 3.7: Time series of MODIS and model-predicted daytime ΔT and annual precipitation. **a**, Billings, Montana. **b**, Richmond, Virginia.

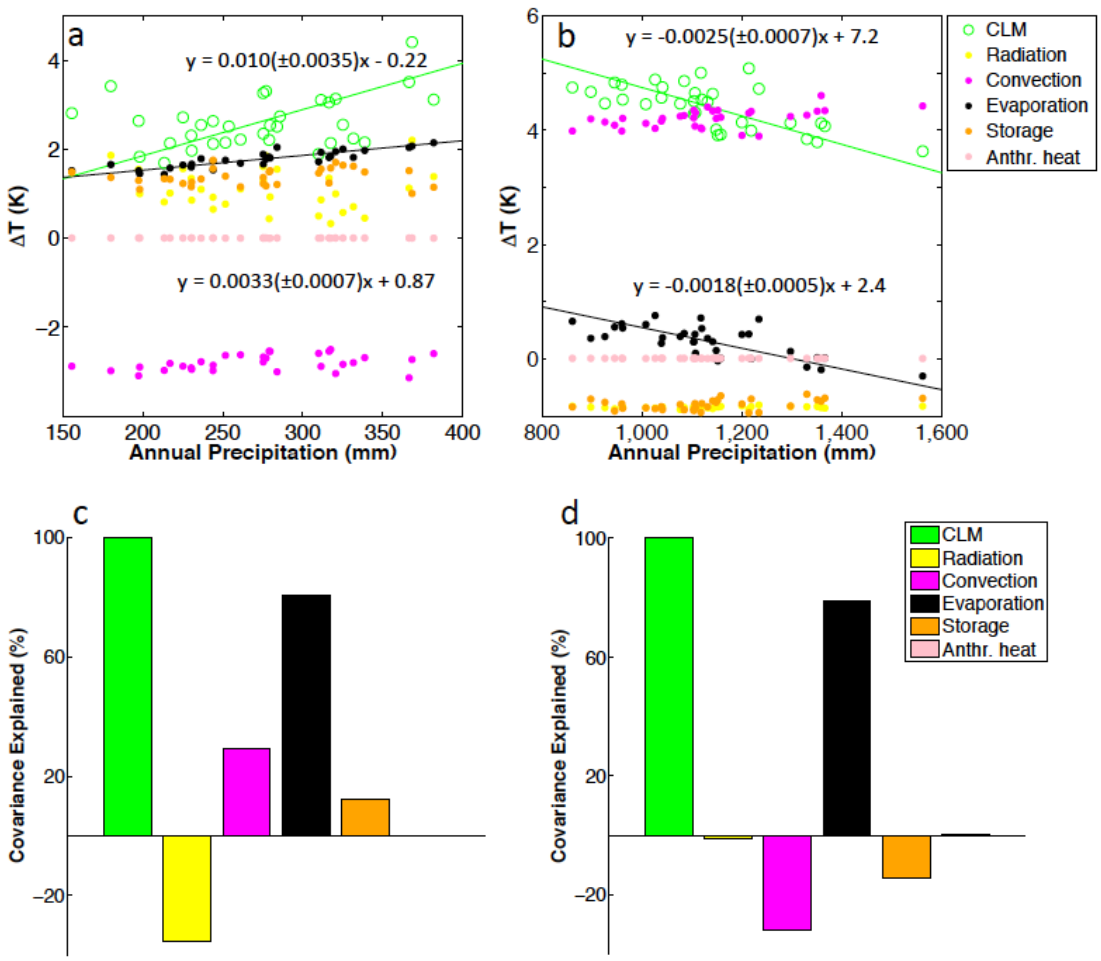

Figure 3.8: Relationship between interannual variations in model-predicted daytime ΔT and precipitation. **a**, Correlation of ΔT and the individual biophysical components with annual precipitation at Billings, Montana. **b**, same as in panel **a** except for Richmond, Virginia. **c**, ΔT – precipitation temporal covariance explained by different biophysical factors at Billings, Montana. **d**, same as in panel **c** except for Richmond, Virginia. Lines are best linear regression fit to the data points.

Our results can be interpreted in the context of heatwave climatology. A measure of heatwave intensity is the degree of deviation, in multiples of standard deviation (σ, North America mean value ~0.6 K) of summertime temperature from the climatological mean [*Hansen et al.*, 2012]. For example, the 2003 European heatwave[8] is an event measured at 5σ. These statistical considerations are based on regional background climatology. Being an additional anomaly on this background condition, UHI will aggravate heat stress on human health. In southeast United States, where the heat stress is already amplified due to high air humidity [*Smith et al.*, 2013], the daytime ΔT is equivalent to 7σ (Figure 3.3e). The situation may be further worsened in drier years when the positive temperature anomaly is likely to increase owing to a precipitation – temperature feedback [*Schar et al.*, 2004]. Empirical evidence exists for such synergistic effects [*Li and Bou-Zeid*, 2013]. Using the temporal sensitivity of -0.0021 K/mm, a 500 mm reduction in the annual precipitation corresponds to an increase in the daytime ΔT by 1.1 K or ~2σ. We caution that these numbers represent the upper bound of the UHI-added stress because UHI intensity at the screen-height [*Gallo et al.*, 2002] (the height of air temperature observation at a standard weather station) and under all-sky conditions should be smaller than our ΔT which is for clear skies and for the surface. On the other hand, summertime ΔT is generally larger than annual ΔT [*Arnfield*, 2003; *Clinton and Gong*, 2013; *Hung et al.*, 2006; *Imhoff et al.*, 2010; *Peng et al.*, 2012; *Roth et al.*, 1989].

3.2.4 Implications for urban mitigation strategies

The health impact of heatwaves is one factor that motivates the growing efforts to mitigate UHI. According to our results, a strategy that focuses on reducing anthropogenic heat would bring virtually no relief, but this might be because of the primitive anthropogenic heat scheme in the model [*Oleson*, 2012]. Managing the convection efficiency or heat storage of urban land does not seem viable, even though these are large contributors to ΔT, because it would require fundamental changes to the urban morphology such as a city-wide increase in building height. On the other hand, efforts to increase urban albedo have the promise of producing measurable results on a large scale. For the cities in southern United States, the reduction of net radiation loading amounts to a daytime cooling effect of 0.7 K (Figure 3.3e). In the model, this reduction is caused by the fact that these cities have an average albedo that is 0.06 higher than the surrounding natural land. This albedo difference is modest, considering that phasing in reflective roofs in Chicago [*Mackey et al.*, 2012] has already increased the city-wide albedo by ~0.02 and that some cool-roof implementations [*Georgescu et al.*, 2013] aim to increase the urban-rural albedo contrast by as much as 0.6. Albedo increases have little direct effect on the nighttime UHI (Figure 3.3g) but may have an indirect cooling benefit through the reduction in the daytime heat storage and therefore less heat release from storage at night [*Oleson et al.*, 2008a; *Peng et al.*, 2012; *Rosenzweig et al.*, 2009]. The negative correlation between the nighttime ΔT and urban-rural albedo contrast [*Peng et al.*, 2012] (Figure 3.4) can be viewed as empirical evidence of this indirect benefit.

3.3 Conclusions

This study investigated the contributions of biophysical processes to urban heat island (ΔT), defined as urban – rural difference in radiative surface temperature, across difference climate regimes. The analysis of MODIS land surface temperature (LST) over 65 selected cities in the North America shows that the annual-mean midday ΔT is strongly correlated with precipitation, and that the annual-mean midnight ΔT is positively correlated with the logarithm of population but statistically invariant with precipitation. This midday ΔT – precipitation correlation can be recognized as a geographic pattern. A 33-year simulation was conducted using CLM. We developed a ΔT attribution method, and applied the method to the modeled data to estimate the contribution of each biophysical process to ΔT. The modeled results show that, for cities across North America, this geographic variation in daytime ΔT is largely explained by changes in convection efficiency between urban and nonurban land. This convection effect depends on the local background climate, contributing 3.0 $\pm$ 0.3 K (mean and standard error, s. e.) warming to daytime ΔT in cities in humid climate but causing 1.5 $\pm$ 0.2 K cooling in dry climate. At nighttime, the dominant contributor to ΔT is the release of the heat storage. The correlation between nighttime ΔT and population can be understood as the accumulative effect of the stored heat release as air moves across the urban land.

The yearly ΔT data derived from both MODIS and CLM were analyzed to examine the interannual variability of ΔT. We found that in the humid eastern United States, the annual daytime ΔT is negatively correlated with the annual precipitation. This

indicates that there will be higher ΔT in drier years. This relationship implies that UHI will exacerbate heatwave stress on human health in wet climates where high temperature effects are already compounded by high air humidity and in drier years when positive temperature anomalies may be reinforced by a precipitation - temperature feedback.

The implications of this study on urban mitigation strategies were also introduced. Our results support the city albedo management as a viable means of reducing ΔT on large scales.

3.4 Methods

3.4.1 MODIS LST, precipitation, and population data

MODIS-Aqua land surface temperature (LST) data obtained at 65 cities in the US and Canada were used in this analysis. This is an 8-day clear-sky composite dataset. The spatial resolution is 1 km. The satellite overpass time is approximately 13:30 and 01:30 local time, which are close to the times of daily maximum and minimum temperature, and therefore the measurement gives better representation of the diurnal range of the ΔT than that of the other MODIS satellite Terra. According to the product QC (quality control) flag, the data we used have an average LST error less than or equal to 2 K. While selecting urban-rural paired pixels, we avoided the rural pixels that have large elevation differences and large latitude differences from the urban core. Specifically, the upper thresholds for elevation difference and latitude difference are 100 m and 0.1 degrees. Nine urban pixels (3 × 3) were selected in the

city center, paired with 1-3 patches of 9-49 pixels each (3×3 to 7×7) in the surrounding nonurban land. Because of topographic and latitudinal limitations, the number of rural pixels varied (one patch for 15 cities, two patches for 41 cities and three patches for 9 cities). The magnitude of ΔT is insensitive to the number of urban-rural pixels. Fixing the number of urban and rural pixels for all the cities to 1 patch of 3×3 pixels altered the ΔT by at most 0.6 K. All the pixels selected were validated by the MODIS land cover map and cross-checked against Google Earth. Rural pixels are classified in the MODIS land cover map as natural surfaces such as forests, grassland, cropland and bare soils. To avoid high bias of UHI, we excluded water pixels. Urban pixels are classified in the MODIS land cover map as urban and built-up surface. The resulting ΔT represents the difference between the city core and minimally developed land outside the city. The annual mean values were calculated based on the 10 years' time series of the MODIS LST (2003 - 2012). A linear gap filling was done for short periods of missing values to minimize the impact of missing data on the annual means. If there are more than 3 consecutive missing values, we excluded that year.

Cities were chosen so that each state, province, or territory was represented by at least one city, with the exception of 4 provinces and a territory in Canada (Nova Scotia, Prince Edward Island and Newfoundland and Labrador; Table 3.2). The chosen cities are large enough to be resolved by the climate model, except for 5 small cities (Helena, Montana; Augusta, Maine; Whitehorse, Yukon; Yellowknife, Northwest Territories; Iqaluit, Nunavut). These cities span a population range of 7000 – 379300. In addition, we avoided the cities on hilly terrain.

The US precipitation data were obtained from PRISM (PRISM Climate Group, Oregon State University, http://prism.oregonstate.edu). The precipitation data for cities in Canada were obtained from Environment Canada (http://climate.weather.gc.ca/). The PRISM datasets are elevation-corrected grid estimates of monthly, yearly and event-based climatic variables. The precipitation data for Canadian cities are station measurements.

The population data were obtained from the US Census 2010 (http://quickfacts.census.gov) and Canada 2011 Census from Statistics Canada (http://www12.statcan.gc.ca/census-recensement/2011/dp-pd/index-eng.cfm).

Table 3.2: List of selected cities in the United States and Canada

City, State/Province	Population	City size in CLM (km^2)	City, State/Province	Population	City size in CLM (km^2)
Albany, NY	9.79E+04	15.45	Louisville, KY	7.41E+05	45.75
Albuquerque, NM	5.53E+05	25.24	Madison, WI	2.33E+05	22.73
Atlanta, GA	4.20E+05	117.03	Minneapolis, MN	3.83E+05	90.58
Augusta, ME	1.86E+04	NA	Montgomery, AL	2.06E+05	12.99
Austin, TX	8.21E+05	63.16	Montreal, QC	1.65E+06	41.10
Baton Rouge, LA	2.30E+05	17.70	Nampa, ID	8.16E+04	6.56
Billings, MT	1.06E+05	2.14	Nashville, TN	6.36E+05	30.35
Bismarck, ND	6.13E+04	6.05	Oklahoma City, OK	5.80E+05	10.72
Boise, ID	2.06E+05	12.84	Olympia, WA	4.65E+04	12.94
Boston, MA	6.18E+05	86.42	Philadelphia, PA	1.53E+06	71.51
Calgary, AB	1.10E+06	21.48	Phoenix, AZ	1.45E+06	53.91
Casper, WY	5.53E+04	3.33	Pierre, SD	1.36E+04	0.89
Cheyenne, WY	5.95E+04	2.46	Portland, OR	5.94E+05	54.50
Colorado Springs, CO	4.16E+05	29.43	Providence, RI	1.78E+05	16.06
Columbia, SC	1.29E+05	2.56	Raleigh, NC	4.04E+05	37.60
Columbus, OH	7.87E+05	14.55	Richmond, VA	2.04E+05	8.00
Dallas, TX	1.20E+06	153.98	Sacramento, CA	4.89E+05	36.27
Denver, CO	6.00E+05	75.02	Saint John, NB	7.01E+04	1.42
Des Moines, IA	2.03E+05	32.56	Salem, OR	1.55E+05	14.41
Dover, DE	3.60E+04	1.84	Salt Lake City, UT	1.86E+05	57.87
Hartford, CT	1.25E+05	25.03	Saskatoon, SK	2.22E+05	13.07
Helena, MT	2.82E+04	NA	Seattle, WA	6.21E+05	108.04
Henderson, NV	2.58E+05	31.46	Springfield, IL	1.16E+05	12.97
Houston, TX	2.10E+06	151.09	Tallahassee, FL	1.81E+05	7.58
Indianapolis, IN	8.30E+05	37.56	Topeka, KS	1.27E+05	5.16
Iqaluit, NU	6.70E+03	NA	Toronto, ON	2.62E+06	215.29
Jackson, MS	1.74E+05	15.76	Trenton, NJ	8.49E+04	36.53
Jefferson City, MO	4.31E+04	3.54	Tucson, AZ	5.20E+05	27.73
Lansing, MI	1.14E+05	6.47	Vancouver, BC	6.04E+05	129.04
Las Vegas, NV	5.84E+05	31.46	whitehorse, YT	2.33E+04	NA
Lincoln, NE	2.58E+05	17.24	Winnipeg, MB	6.64E+05	47.08
Little Rock, AR	1.94E+05	13.64	Yellowknife, NT	1.92E+04	NA
Los Angeles, CA	3.79E+06	213.56			

3.4.2 Climate model and simulation

We used NCAR's climate model CESM (Community Earth System Model)[*Hurrell et al.*, 2013] to simulate the UHI in the United States and in Canada In this model system, the land surface processes are represented by the Community Land Model (CLM)[*Oleson et al.*, 2010]. We used CLM version 4.0. In CLM, the land surfaces are categorized into 5 land units: vegetation, glacier, wetland, urban and lake. Each gridcell can have one or more of these land units. The surface radiation and energy balance equations are solved separately for these land units, and the results are aggregated to yield gridcell means. Specifically, the urban land unit is modeled using a "canyon" structure and consists of the following sub-surfaces: roof, sunlit wall, shaded wall, pervious (e.g. bare soil) and impervious (e.g. road, sidewalk, parking lot) canyon floor. It should be noted here that the pervious canyon floor in the urban land unit potentially evaporates more than the comparable bare soil in the rural land, as all of the water in the bare soil column is available for evaporation in the urban land unit. The vegetated land unit corresponds to nonurban or rural land. This landunit may contain up to 15 different plant functional types and bare soil.

The model was run in the offline mode (uncoupled from an active atmospheric model). The urban and rural parameterizations in each gridcell were driven by the same atmospheric forcing. The atmospheric forcing data used in this study is a careful reconstruction of the climatology from 1972 to 2004 [*Qian et al.*, 2006]. It was derived from a combination of the NCEP-NCAR reanalysis [*Kalnay et al.*, 1996], observation-based analyses and observational records. Therefore the dataset has an

improved accuracy compared to the NCEP-NCAR reanalysis. We ran the model for 33 years from 1972 to 2004 after a 60-year spin-up. The simulation was conducted at the finest resolution as a standard model configuration supported by this version of the model (0.23^{o} longitude × 0.31^{o} latitude) in order to resolve individual cities. Please note that even in this finest resolution the gridcell is still large so that the total urban area in a gridcell can be a combination of several urban areas. The surface skin temperature was determined from the emitted longwave radiation for each land unit with an emissivity of 0.88 for the urban land unit and 0.96 for the vegetated land unit. The urban emissivity is the mean value of the weighted averages of the emissivity values of the urban sub-surfaces prescribed in the model for the selected cities. The rural emissivity is the mean value of the weighted average of the vegetation and soil emissivity.

To construct the UHI, urban and rural flux and state variables were extracted from the model output at the gridcells where the selected cities reside. CLM invokes the urban parameterization only if the urban area fraction exceeds a threshold of 0.1%. Therefore 5 small cities used in the MODIS data analysis (Helena, Montana; Augusta, Maine; Whitehorse, Yukon; Yellowknife, Northwest Territories; Iqaluit, Nunavut) are neglected by the model.

We only included the modeled data at 1:00 and 13:00 local time each day in this analysis; these times were selected to match closely the MODIS overpass times. To replicate the MODIS clear-sky conditions, we excluded cloudy days whose clearness

index [*Gu et al.*, 1999] was less than 0.5. We then converted the daily values into 8-day averages. The gap filling and processes of calculating annual means are the same as with the MODIS data. Under all-sky conditions, the modeled UHI intensity is on average 0.59 K lower during the daytime and 0.02 K lower at night than the clear-sky values, and the pattern regarding the component contributions remains unchanged from the clear-sky plot (Figure 3.3).

3.4.3 Attribution of UHI

Attribution of UHI is accomplished by a surface energy balance analysis. We used a factor separation method to isolate the contribution to the model-predicted ΔT from each individual biophysical factor associated with urban land conversion. In this analysis, the nonurban land is regarded as the base state, and urbanization is a perturbation to this base state. The perturbation signal is denoted by Δ. For example, $\Delta T = T_u - T_r$, where T_u is urban surface temperature and T_r is rural surface temperature within the same model gridcell. Following the method of *Lee et al.* [2011], the solution of the UHI intensity can be approximated by

$$\begin{aligned}\Delta T \approx & \frac{\lambda_0}{1+f}\Delta R_n^* \\ & + \frac{-\lambda_0}{(1+f)^2}(R_n^* - Q_s + Q_{AH})\Delta f_1 \\ & + \frac{-\lambda_0}{(1+f)^2}(R_n^* - Q_s + Q_{AH})\Delta f_2 \\ & + \frac{-\lambda_0}{1+f}\Delta Q_s \\ & + \frac{\lambda_0}{1+f}Q_{AH}\end{aligned} \qquad (3.1)$$

with

$$f = \frac{\lambda_0 \rho C_p}{r_a}(1 + \frac{1}{\beta}) \quad (3.2)$$

$$R_n^* = (1-a)K_\downarrow + L_\downarrow - (1-\varepsilon)L_\downarrow - \varepsilon\sigma T_a^4 \quad (3.3)$$

$$\Delta f_1 = \frac{-\lambda_0 \rho C_p}{r_a}(1 + \frac{1}{\beta})\frac{\Delta r_a}{r_a} \quad (3.4)$$

$$\Delta f_2 = \frac{-\lambda_0 \rho C_p}{r_a}(\frac{\Delta\beta}{\beta^2}) \quad (3.5)$$

where T – surface temperature, λ_0 – local climate sensitivity ($= 1/4\varepsilon\sigma T^3$), f – energy redistribution factor, R_n^* – apparent net radiation, ρ – air density, C_p – specific heat of air at constant pressure, r_a – aerodynamic resistance to heat diffusion, β – Bowen ratio, a – surface albedo, $K_\downarrow$ – incoming solar radiation, $L_\downarrow$ – incoming longwave radiation, ε – emissivity, σ – Stefan-Boltzmann constant, T_a – air temperature at a reference height. In this factor separation analysis, we assume that r_a, β, R_n* and Q_S and Q_{AH} are parameters associated with the external perturbation (land use conversion) and are independent of T, and the partial derivative operation can then be carried out on these variables.

In Eq (3.1), the terms on the right hand side represent, in order from the first to the last, contributions from changes in radiation balance (term 1), aerodynamic resistance (term 2), Bowen ratio (term 3), and heat storage (term 4) and from anthropogenic heat addition (term 5). Since r_a is the resistance to sensible or convection heat flux, term 2 is essentially a measure of change in the convection efficiency between urban and nonurban land. In an abstract sense, changes in β (term 3) can result from changes in

sensible heat flux (H), latent heat flux (LE) or both (Eq 3.6). In the present context of partial derivative operation, however, H and LE are not independent because the delta term Δf_2 is evaluated with the net radiation R_n^* and other valuables held constant. Thus a reduction in β is accomplished by channeling more radiation energy to the surface latent heat flux and it is appropriate to attribute term 3 to changes in surface evaporative cooling.

The calculation was performed separately for 1:00 and 13:00 local time, with cloudy days omitted. Three sets of variables were used. The first set comes directly from the forcing data and includes precipitation, incoming solar radiation ($K_{\downarrow}$), reference height air temperature (T_a, air temperature at 30 m above the surface), air pressure and downward longwave radiation ($L_{\downarrow}$). The second set has model-predicted variables, including reflected shortwave radiation ($a K_{\downarrow}$), sensible heat flux (H), latent heat flux (LE), storage heat flux (Q_s) and anthropogenic heat flux (Q_{AH}). The third set of variables, including surface temperature (T), air density (ρ), Bowen ratio (β), and aerodynamic resistance (r_a) were derived from the forcing data and the model-predicted variables. Specifically, Bowen ratio was calculated as

$$\beta = \frac{H}{LE} \qquad (3.6)$$

and the aerodynamic resistance to heat diffusion was calculated from

$$r_a = \frac{\rho C_p (T - T_a)}{H} \qquad (3.7)$$

The aerodynamic resistance determined from Eq 3.7 is the sum of the diffusion resistance in the atmospheric surface layer and the excess resistance associated with the thermal roughness [*Garratt*, 1994; *Voogt and Grimmond*, 2000] (Appendix A). The urban and nonurban land units within each model gridcell have the same forcing variables and have different values for the second and third sets of the variables. It should be noted here that the model underestimates the anthropogenic heat flux (Q_{AH}) due to the primitive anthropogenic heat scheme. The total anthropogenic heat in the model only includes heating and air conditioning (HAC) fluxes, waste heat generated by HAC and the heat removed by air conditioning. These fluxes are based on some prescribed parameters in the surface dataset of CLM and calculated heat transfer into and out of roofs and walls. The traffic heat flux is neglected by the current version of the model [*Oleson et al.*, 2011].

The sum of the component contributions is slightly lower than the modeled ΔT (Figure 3.3) because high-order terms are ignored in the linearization of the surface longwave radiation term of the energy balance equation and nonlinear interactions among the factors are omitted in the analysis. Comparison between model-predicted ΔT and calculated ΔT (sum of the individual contributions) reveals excellent correlation for daytime ($r = 0.88$, $p < 0.001$) and nighttime ($r = 0.55$, $p < 0.001$).

3.4.4 Covariance analysis

The covariance analysis was performed on modeled ΔT and its components against precipitation. Let C_R, C_H, C_{LE}, C_s and C_{AH} be the contribution from radiation,

convection efficiency, evaporation, storage and anthropogenic heat, respectively (terms 1 to 5 in Eq. 3.1). Eq. 3.1 can be rewritten as

$$\Delta T = C_R + C_H + C_{LE} + C_s + C_{AH} + e$$

where e is an error term arising from nonlinear interactions. Because the covariance operation is linear, the ΔT – precipitation covariance is equal to the sum of the covariance between each component and precipitation,

$$\begin{aligned} Cov(\Delta T, P) = {} & Cov(C_R, P) + Cov(C_H, P) + Cov(C_{LE}, P) \\ & + Cov(C_s, P) + Cov(C_{AH}, P) + Cov(e, P) \end{aligned} \qquad (3.8)$$

where P is precipitation. Eq. 3.8 decomposes the total covariance between ΔT and precipitation into the covariance contribution from its five components and a residual error term. We presented covariance here rather than correlation coefficient because the correlation is not a linear operation. In Figures 3.5 and 3.8, we normalized the covariance between each component and precipitation by the total ΔT – precipitation covariance.

We applied this technique to the analysis of both spatial covariance and temporal covariance. In the analysis of spatial covariance, each data point is the annual mean value of a city (Figure 3.5). In the analysis of the temporal covariance at a city, each data point is the annual value of that city (Figure 3.8).

Chapter 4 Urban heat islands under climate change

Summary

Predictions of urban heat island under climate change in the future are crucial for urban climate change mitigations and spatial planning and development. A 96-year simulation using community land model (CLM) driven by CESM RCP8.5 output climatology was conducted. Results show that ΔT generally decreases across all three climate regions under the RCP8.5 scenario. The spatial pattern of ΔT that we observed in the current climate still holds in the future. The variations in convection efficiency between urban and rural areas still large explain the geographic variation of daytime ΔT. The release of stored heat is the prominent contributor of nighttime ΔT. Compared to the current climate, the flourishing vegetation in the rural areas due to climate change affects the contributions of convection efficiency and radiation to daytime ΔT. At night, the two major changes in the future are the increased contribution from release of stored heat and the significant decreased contribution of evaporation.

4.1 Background

From the previous chapter, I have learned the contribution of each biophysical process to the urban heat island under current climate. How UHIs will change in future and how these contributions from the biophysical processes change with climate change remain elusive questions. Therefore I continued my study to the UHI projection under future scenarios.

A recent modeling study has shown that the UHI, defined as 2-m air temperature, would generally decrease in the future with magnitudes depending on the RCP scenarios, because urban and rural areas respond differently to changes in climate[*Oleson*, 2012]. However, whether the UHI, defined as surface radiative temperature difference, behaves similarly with the 2-m UHI in the future scenario is unclear. Surface radiative temperature is a more direct metric of the surface energy budget than the 2-m height air temperature, because it is derived from the surface energy balance equation. Therefore a study of UHI defined by surface radiative temperature under climate change is worthwhile.

4.2 Methods

4.2.1 CLM simulation

We ran CLM in an uncoupled mode driven by the output data from the CESM fully coupled simulation. The output data from CESM simulations are existing data maintained by NCAR. The fully coupled CESM simulations were conducted following the protocol of CMIP5 [*Taylor et al.*, 2009] in four Representative

Concentration Pathways (RCP) scenarios (RCP8.5, RCP6, RCP4.5 and RCP2.6; [*Moss et al.*, 2010]). The four RCP scenarios represent from lowest to highest anthropogenic greenhouse gas emission pathways. In order to emphasize the effects of anthropogenic climate forcing on the UHI, we only used the output data from CESM RCP8.5 simulation to drive the CLM. Although the simulation was conducted in this uncoupled way, the land-atmosphere-ocean feedbacks and the horizontal advection have been computed in the fully coupled CESM simulation and reflected in its atmospheric output. Therefore this way can be considered as a shortcut to retrieve the land surface properties compared to running the fully coupled CESM under the RCP8.5 scenario.

The model was run for 96 years from 2005 to 2100. The spin-up was waived because we used an initial dataset which represents an equilibrium climate state to start the simulation. The spatial resolution of the simulation is 0.9° longitude × 1.25° latitude.

4.2.2 Data analysis

We used the same 65 selected cities in the US and Canada as we did in the previous chapter. The cities are grouped in three climate zones according to Köppen-Geiger climate classification. The modeled data were analyzed with respect to the three climate zones. In order to show the complete simulated trend, we concatenated the modeled data in "current climate" (1972 to 2004; Chapter 3) and the future projections from 2005 to 2100. Time series of modeled precipitation, 2m height air temperature, surface incoming solar radiation, and ΔT were analyzed.

We applied the same ΔT attribution method on the modeled results of last thirty years of this century (2071-2100) to investigate how the contribution of each biophysical process changes with climate change.

The annual mean values only reflect the average state of the daytime and nighttime ΔT. In order to investigate the variability of ΔT, we analyzed the distributions of ΔT and compared them between current climate and future climate to see how variability of ΔT changes with climate change in the future. The data used in this analysis are all daily values.

4.3 Results and discussion

4.3.1 Trends

Like most climate modes or Earth system models, CESM overestimates the incoming solar radiation at the surface as well, according to our results. This is consistent with what we demonstrated in Chapter 2. Figure 4.1d, 4.2d and 4.3d show significant inconsistency in midday surface incoming solar radiation between the current climate (1972-2004) and the future climate (2005-2100) across the three climate zones. The inconsistency is because of the two different forcing data of solar radiation. The radiation forcing for current climate simulation is an revised climatology reanalysis data based on surface observations, and the downward solar radiation at the surface is reduced by 10-20% after revision[*Qian et al.*, 2006]. The solar radiation for the future projection simulation, however, is purely modeled by the radiative transfer model of

CESM without any observation-based bias correction. From Figure 4.1c and 4.2c, we can see that this inconsistency of incoming solar radiation causes a sharp increase in 2m-height air temperature in the continental and temperate climates. This indicates that the overestimation of surface incoming solar radiation in the mode will result in significant high biases in the prediction of near-surface temperature. This finding together with our work described in Chapter 2 calls for attentions to the overestimation of surface incoming solar radiation in climate models.

Across all three climate zones, the rural 2m-height air temperature persistently increases due to the background climate warming, which is as expected (Figure 4.1c, 4.2c and 4.3c). Specifically, the warming rates are 0.07 K yr^{-1}, 0.04 K yr^{-1}, and 0.07 K yr^{-1} in the continental, temperate and dry climates, respectively. The annual mean precipitation in the three regions show slight increasing trends as well (Figure 4.1b, 4.2b and 4.3b). The average increasing rates are 1.1 mm yr^{-1}, 2.0 mm yr^{-1}, and 1.3 mm yr^{-1} in the continental, temperate and dry climates, respectively.

Figure 4.1a, 4.2a and 4.3a show that daytime ΔT generally decreases in all three climate zones. This is consistent with *Oleson* [2012]'s findings, although the ΔT in his study is defined by 2m-height air temperature rather than surface radiative temperature. This persistent decreasing trend in ΔT indicates that urban and rural areas respond differently to changes in climate. Urban surfaces stay the same under climate change in the CLM, whereas the rural areas respond to the climate change. Generally, because of the increasing precipitation and higher atmospheric CO_2

concentrations in the future, the vegetation in the rural areas become denser. This will affect the radiation balance, convection, and evapotranspiration over rural areas. How these surface energy fluxes influence ΔT will be discuss in detail in the next section.

The two water-sufficient climate zones show more significant decreasing trends in daytime ΔT than the dry climate does (Figure 4.1a, 4.2a and 4.3a). This is consistent with what we discovered about the interannual variability of daytime ΔT in Chapter 3: in humid climates, the annual daytime ΔT is negatively correlated with annual precipitation. In the future, this relationship still holds. Figure 4.4 shows that the inter-annual variability of daytime is primarily driven by variations in precipitation in both current climate and future climate. In comparison, Figure 4.5 shows that in dry climates, this ΔT – precipitation temporal correlation is insignificant.

During nighttime, ΔT does not show significant trends in the three climate regions (Figure 4.6). This is because the dominant driver of nighttime ΔT is the release of the stored heat rather than precipitation. The heat storage is determined by the urban built-up structures and materials. However, in CLM all the urban canyon parameters stay constant from year to year. Therefore the background climate trends do not significantly drive the variation of nighttime ΔT.

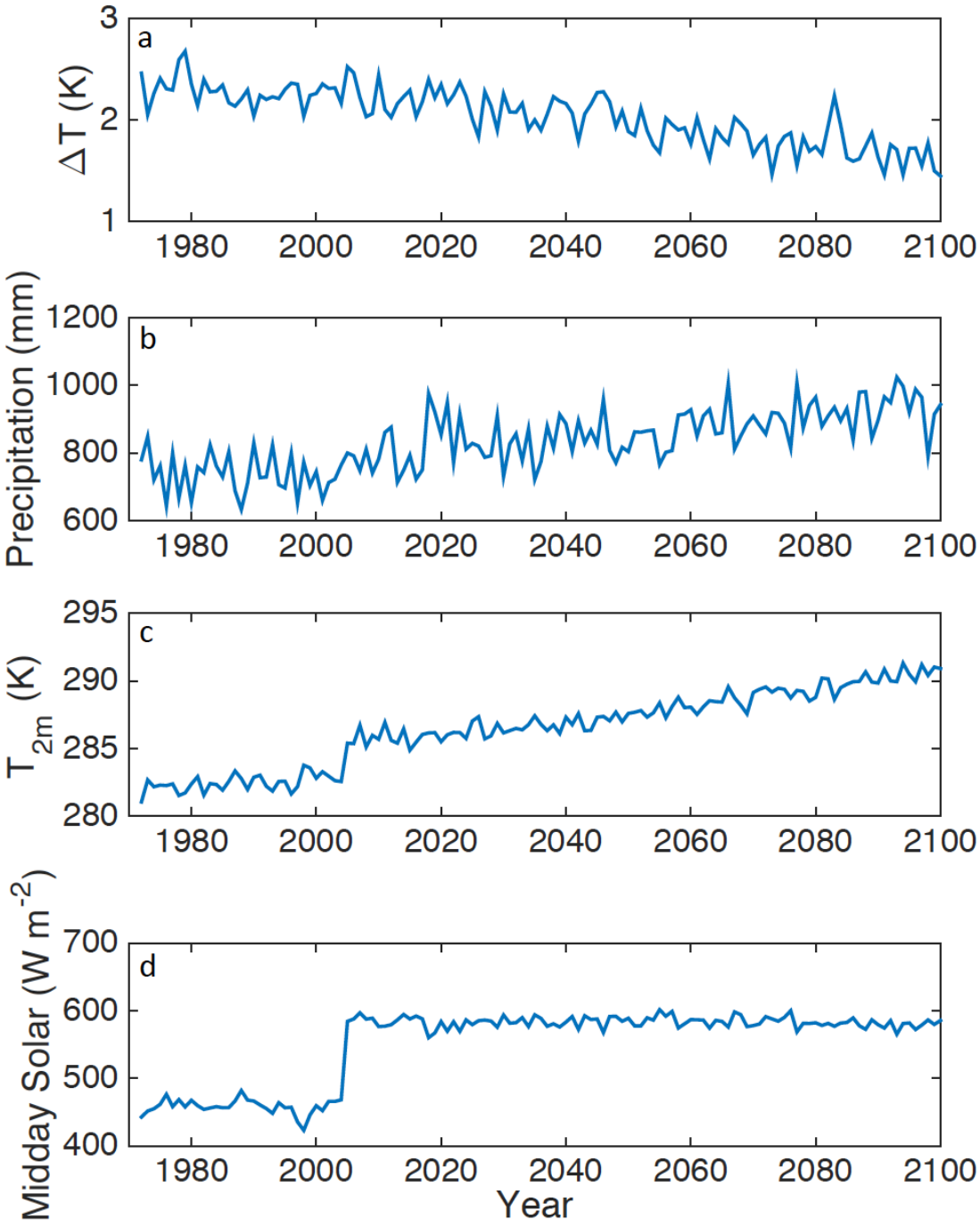

Figure 4.1 Modeled time series of ΔT and background climate variables from 1972 to 2100 in continental/microthermal climates. a: daytime ΔT; b: annual precipitation; c: 2m-height air temperature; d: midday surface incoming solar radiation

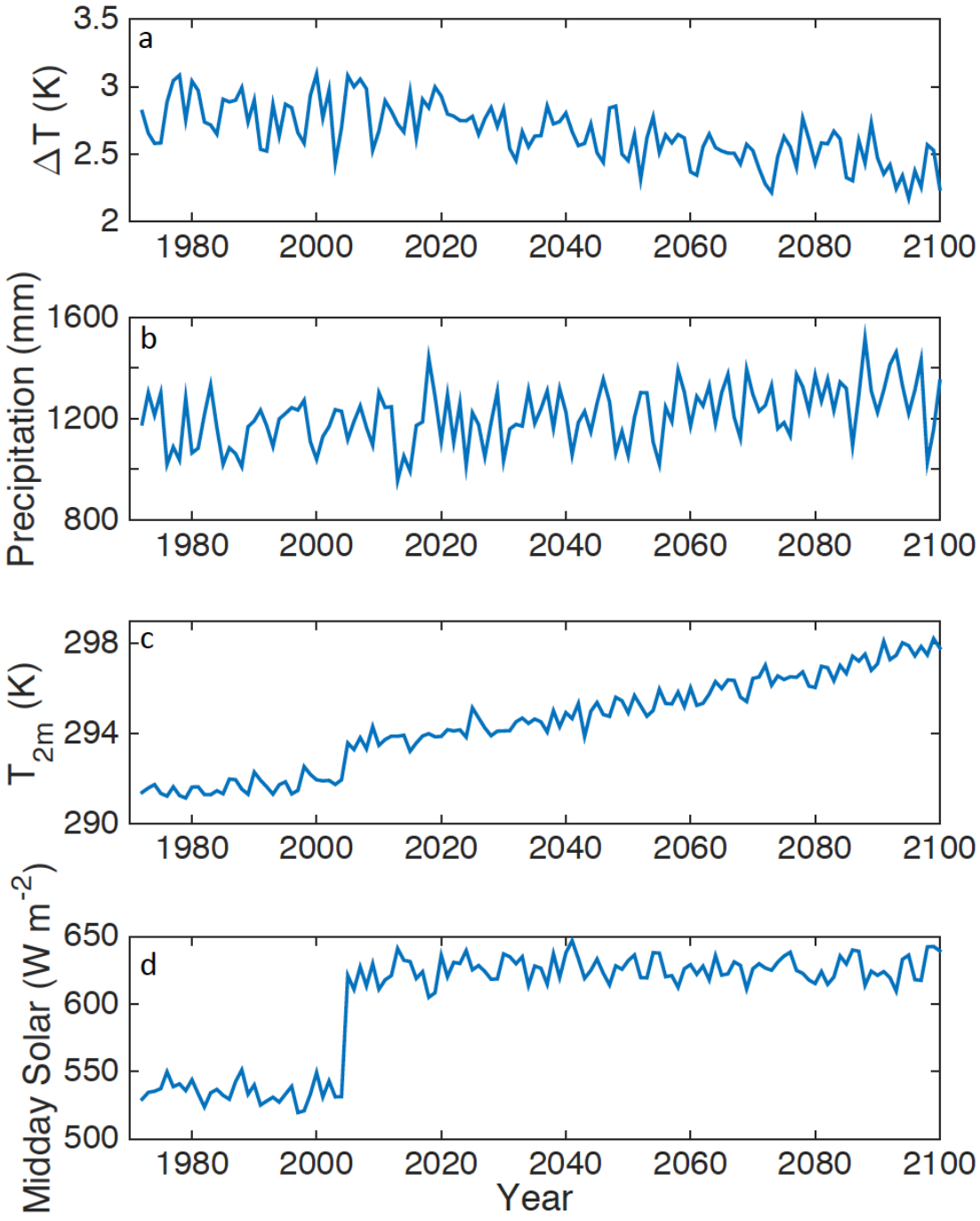

Figure 4.2 Same with Figure 4.1 except for in temperate/mesothermal climates.

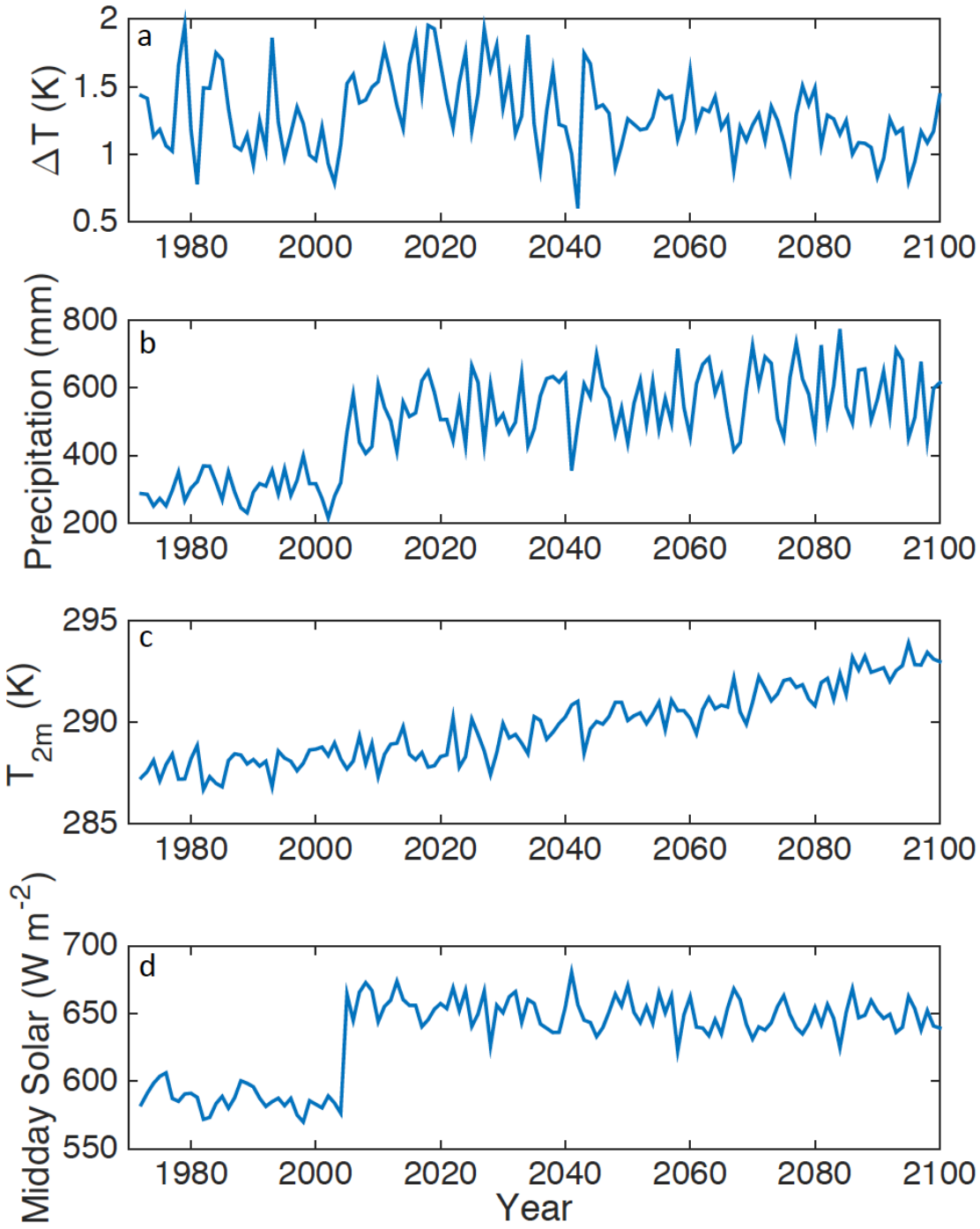

Figure 4.3 Same with Figure 4.1 except for in dry climates.

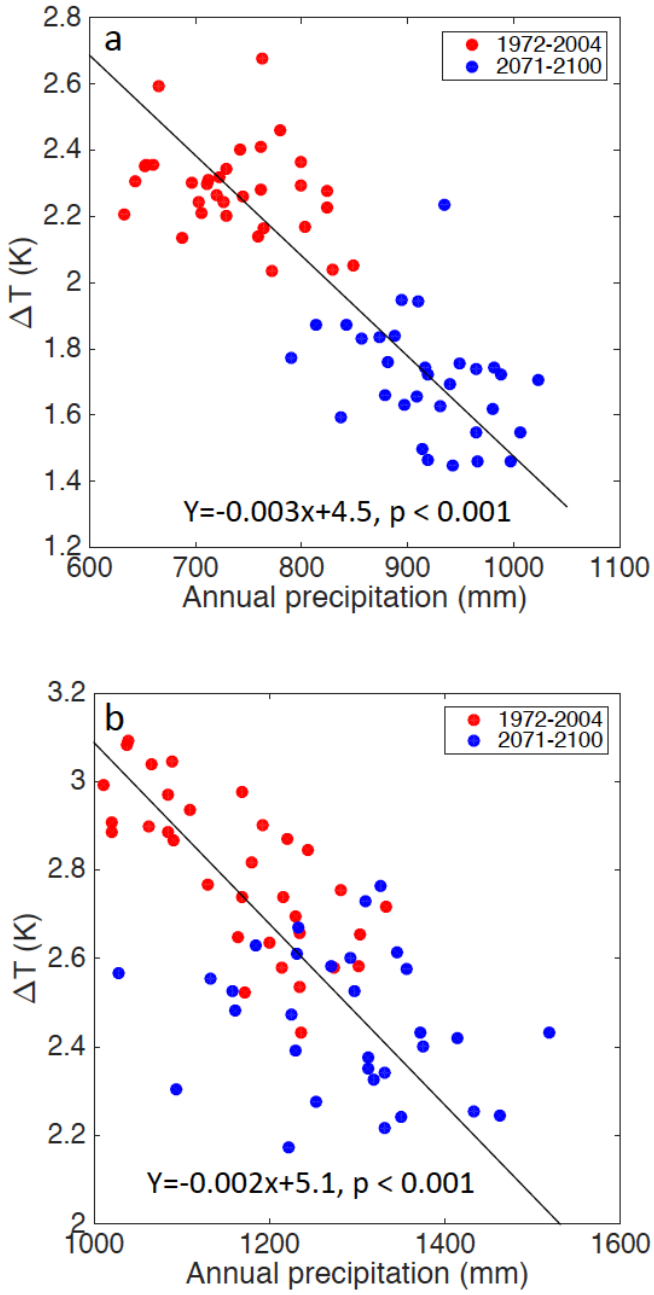

Figure 4.4 Correlation between daytime ΔT and annual precipitation in continental and temperate climates. a: continental/microthermal climates; b: temperate/mesothermal climates.

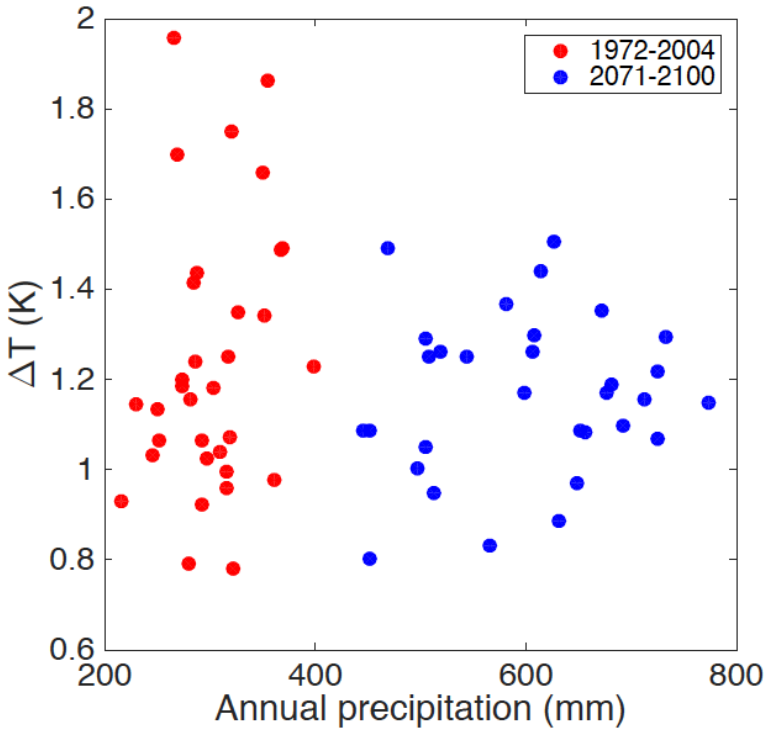

Figure 4.5 Same with Figure 4.4 expect for in dry climates

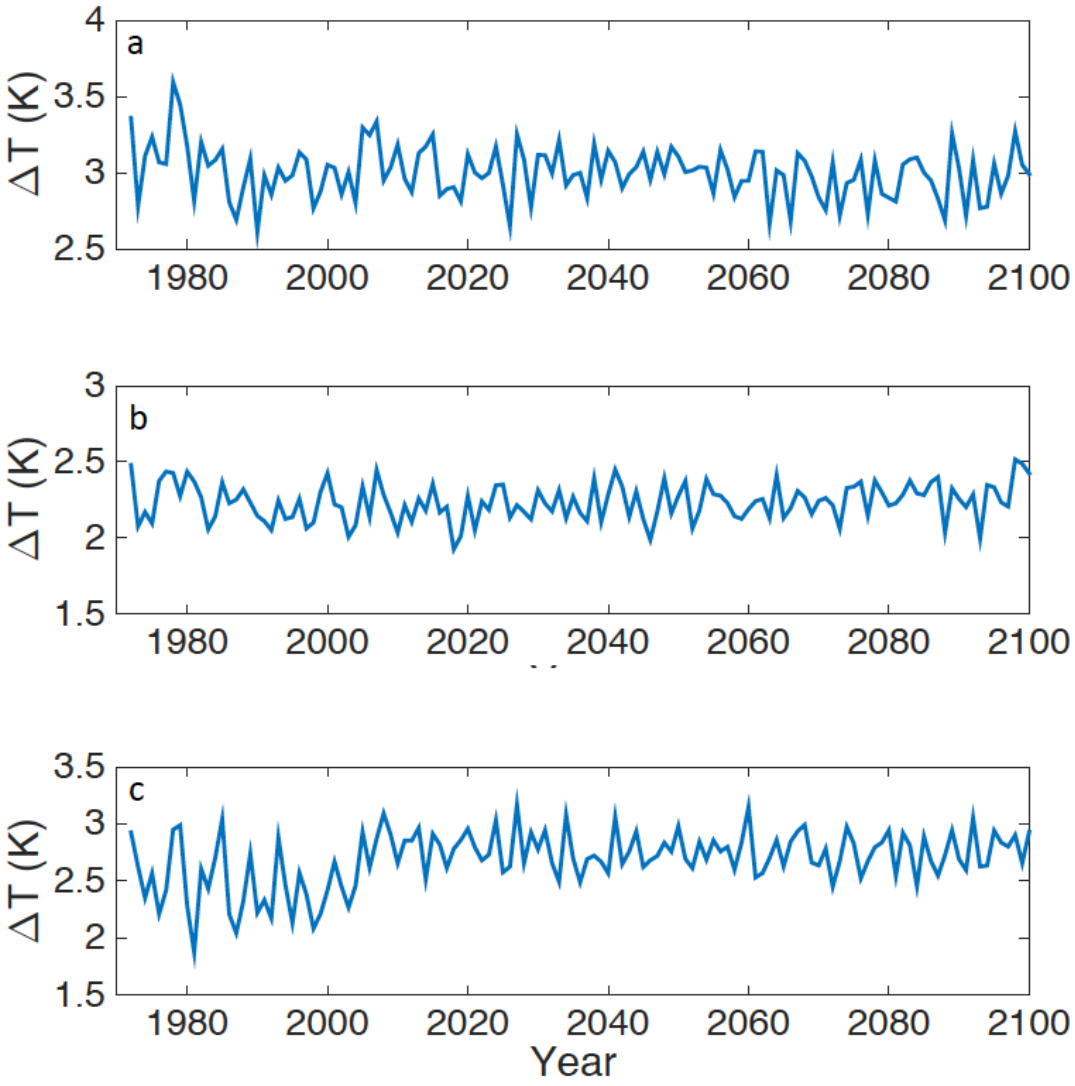

Figure 4.6 Modeled time series of nighttime ΔT in the three climate regions. a: continental/microthermal climates; b: temperate/mesothermal climates; c: dry climates.

4.3.2 Biophysical feedbacks in the future

The spatial pattern of ΔT that we observed in the current climate still holds in the future. In the daytime, there is higher ΔT in wetter climates and lower ΔT in dry climates. This geographic variation is still driven by variations in the convection efficiency between urban and rural areas. This convection effect still depends on the local background climate, increasing daytime ΔT by 2.1 K in humid climates but decreasing ΔT by 0.6 K in dry climates in the end of this century. In the nighttime, release of the stored heat is still the dominant contributor to ΔT across all three climate zones.

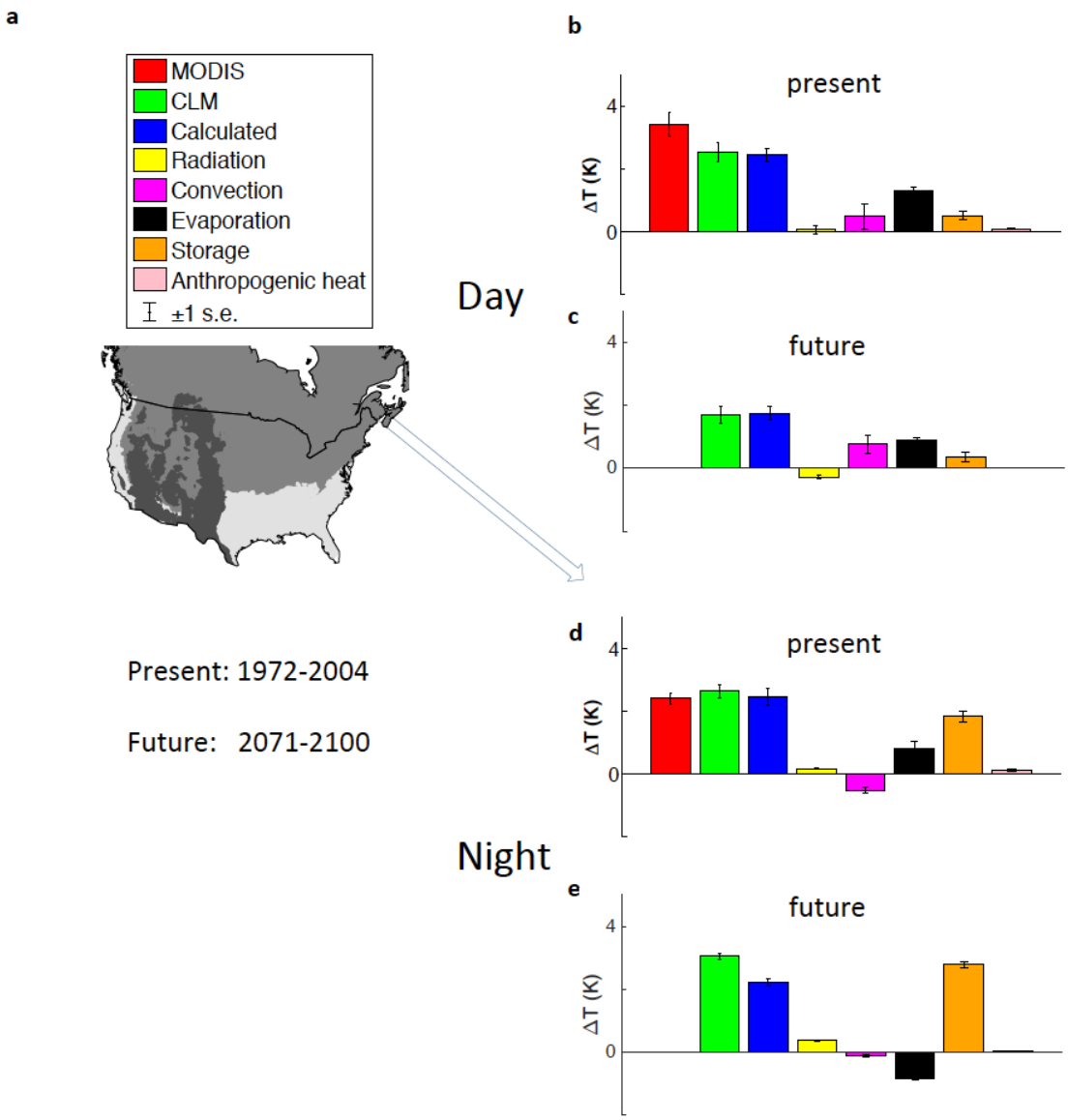

Figure 4.7 Comparison of attribution of ΔT between present and future in continental/microthermal climates. b: present daytime; c: future daytime; d: present nighttime; e: future nighttime

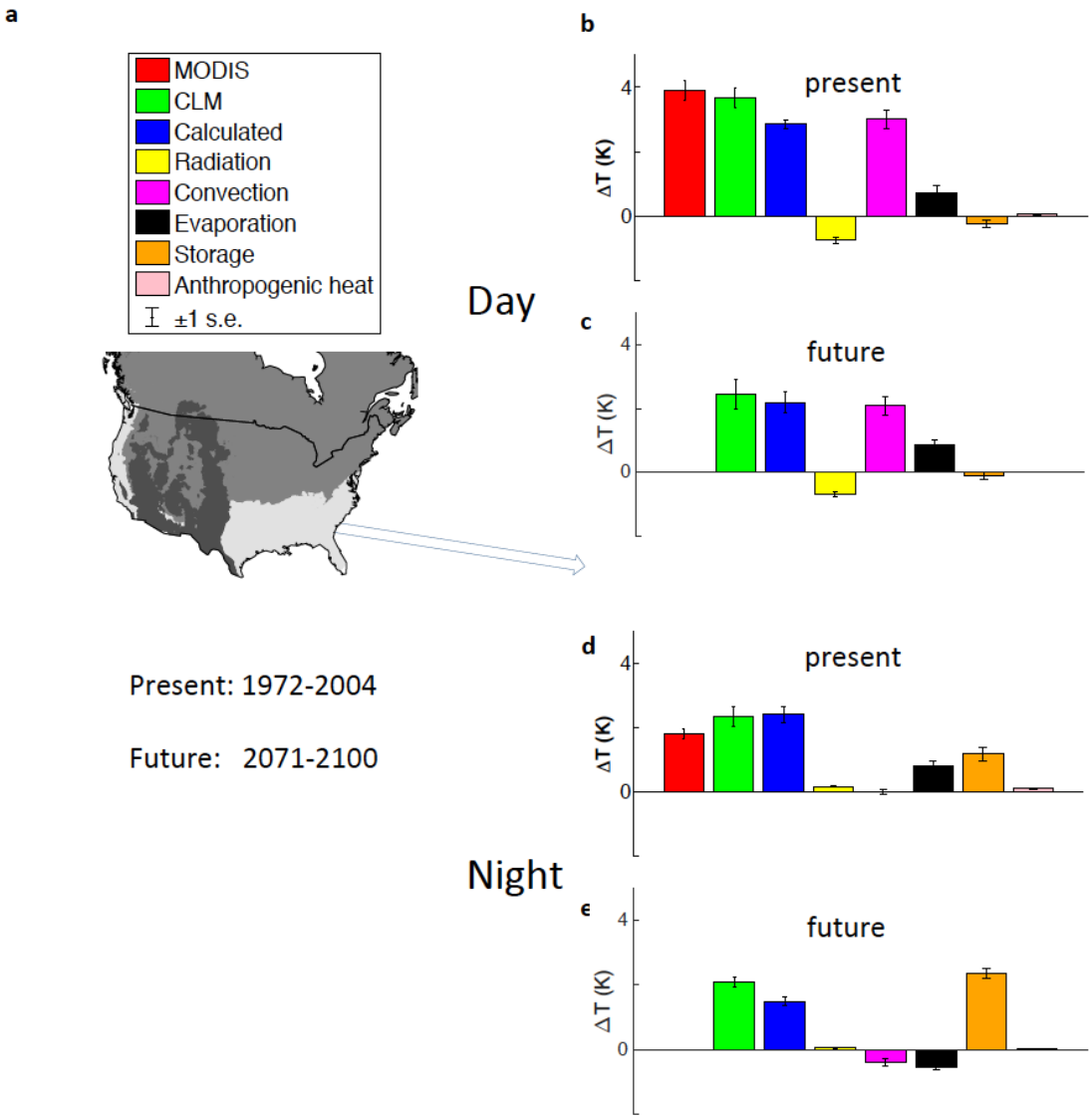

Figure 4.8 Same with Figure 4.7 except for in temperate/mesothermal climates

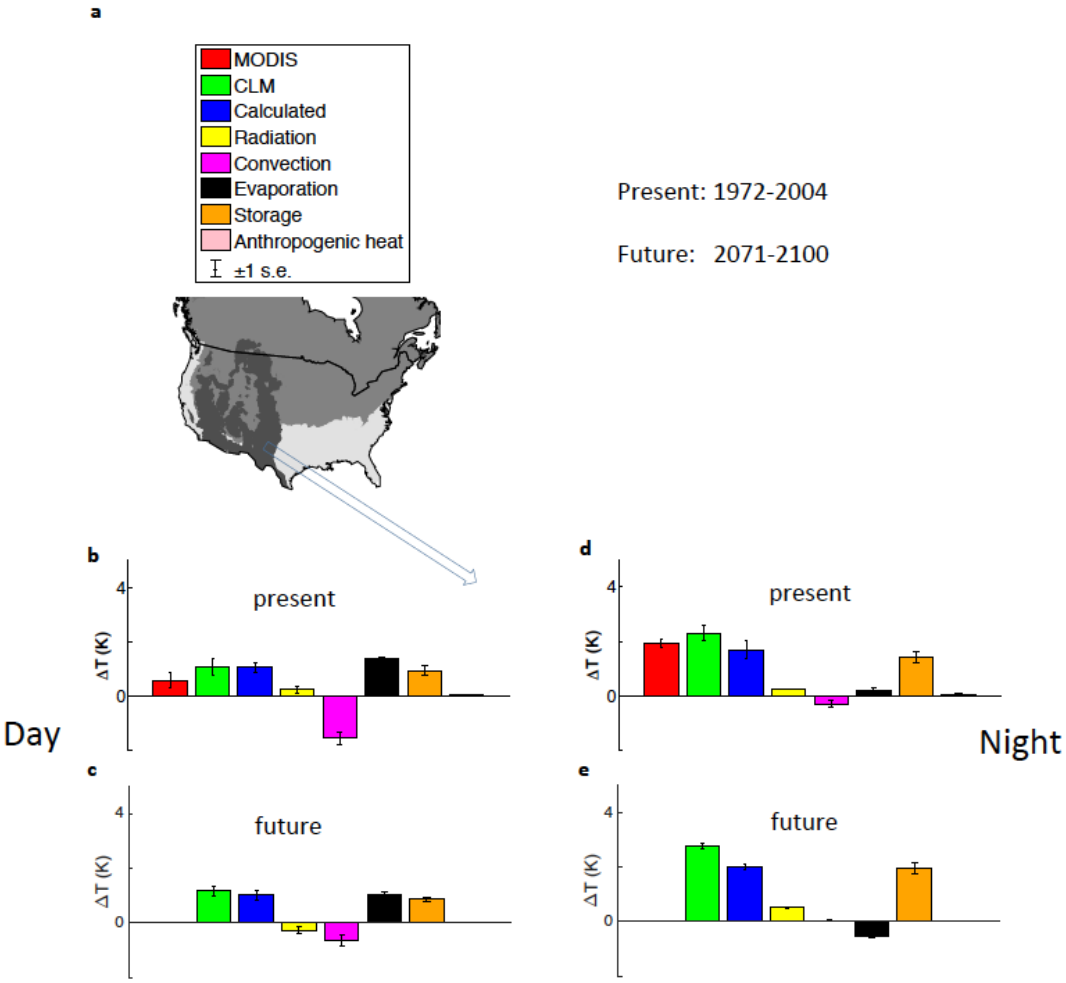

Figure 4.9 Same with Figure 4.7 except for in dry climates.

Figure 4.7 - 4.9 show the comparison of ΔT attribution between current climate (1972-2004) and future climate (2071-2100) in the three climate regions. In the dry climates, the negative contribution of convection term to daytime ΔT decreases significantly in the future compared to that in the current climate. This is because the increasing precipitation and the fertilization of enriched CO_2 in the atmosphere dense the vegetation in the rural areas. Therefore the rural surface becomes rougher in the future compared to that in the current climate, which reduces the difference in the convection efficiency between urban and rural areas. In the relatively wetter regions – continental and humid climates, the change in the contribution of convection efficiency is not that clear. In the continental climates, the convection term increases in the future compared to in the current climate; whereas in the temperate climates, the convection term decreases. This is because for dense vegetation, the surface roughness length is not a monotone function of LAI [*Raupach*, 1994]. The surface roughness length increases as LAI increases in the range of small LAI. Beyond a certain threshold, the roughness length starts to decrease as LAI further increases. This means that at high LAI surfaces, although the increasing precipitation and enriched CO_2 in the atmosphere would fertilize the vegetation and increase the LAI, the surface does not necessarily become rougher. In the continental climates, the surface roughness is still in the increasing phase when LAI increases in the future. Therefore the difference in convection efficiency between rural and urban areas is enlarged in the future. The opposite occurs in the temperate climate zone, where the LAI in the rural areas is already high. The increasing LAI in the future actually reduces the surface roughness length. The result is that the rural surface is less rough

in the future compared to in the current climate. Thus the convection efficiency in the rural areas is lessened.

Vegetation typically has a lower albedo than dry soil and concrete. Therefore a landscape covered by denser vegetation in the future due to the ample precipitation could be darker compared to an open or partially covered landscape in the current climate. The contribution of radiation term to the daytime ΔT can be understood in light of these results. The changes in the radiation term in the continental and dry climates are good demonstrations. In the current climate, the cities in these two zones are slightly darker than the surrounding rural areas due to the canyon effect. Specifically, the urban effective albedo is 0.001 and 0.004 less than the rural albedo in continental and dry climates, respectively. In the future climate, the contribution of the radiation terms become negative in these two zones. This is because the rural areas are darker than the urban areas in the future, making the rural areas absorb more energy. This radiation difference between urban and rural areas creates a cooling effect to the urban in these two zones.

In the night, there are two prominent changes in the contributions of biophysical processes to ΔT between current and future climate. First, the contribution from release of stored heat increases across all three climate zones. The reason for this lies in two aspects. One is the overestimated incoming solar radiation in the model for the period of 2005 - 2100. The extra solar radiation absorbed in the daytime will be stored and release in the nighttime. The other reason is the increased longwave

forcing due to the global warming is stored during daytime and is released at night. Second, the contribution of evaporation to nighttime ΔT is positive in all three climate zones in the current climate, but turns to negative in the future. The reason for this phenomenon lies in the projected increasing precipitation. In CLM, the pervious surface in the urban canyon is allowed to evaporate the whole water column in the soil. Therefore the increased precipitation might significantly raise the urban evaporation, and thus causing a cooling effect. But this result might be because of the unrealistic scheme of urban soil evaporation in the CLM.

4.4 Conclusions

In this study, the CESM modeled urban heat island intensity (ΔT) in the RCP8.5 scenario was examined for 65 selected North American cities. The UHI here is defined as the difference in surface radiative temperature between urban and rural surfaces in the model grid cell. Although the background near-surface temperature increases in the future, ΔT is found to decrease in the RCP8.5 scenario. Similar with in the current climate, the daytime ΔT is still higher in wetter climates, and lower in dry climates in the future. This geographic variation is still largely explained by the variations in the convection efficiency between urban and rural areas. In the nighttime, the release of stored heat is still the prominent contributor of ΔT.

Because of the enriched CO2 in the atmosphere and increasing precipitation in the future, the rural areas are generally greening. This results in increased convection efficiency in rural areas in the continental and dry climates, and decreased rural

convection efficiency in the temperate climates in the daytime. Because vegetation typically has a low albedo, denser vegetation in the future makes the rural surface darker, leading to a warming effect to rural surfaces, and thus negatively contributes the daytime ΔT.

For the nighttime ΔT, two prominent changes in the contribution of biophysical processes emerge: increased contribution from heat storage and decreased contribution from evaporation (sign changed from positive to negative). The increased contribution of heat storage is because of the increased longwave radiative forcing due to the greenhouse gas effect. The decreased contribution of evaporation is because urban landunit responses strongly to the increased precipitation in the CLM.

Chapter 5 Summary and future works

5.1 Major results

5.1.1 Overestimated surface solar radiation

In this dissertation, the surface incoming shortwave radiation *S* modeled by two data assimilation systems, NARR and MERRA, was validated against observations from 24 FLUXNET sites in the US and Canada. Results show that the two data assimilation systems overestimated the surface solar radiation on both monthly and annual scales. MERRA generally shows better agreement with the surface observations than NARR. Specifically, the annual mean bias errors for the FLUXNET sites in North America are +37.2 W m^{-2} and +20.2 W m^{-2} for NARR and MERRA, respectively. The bias errors were larger under cloudy skies than under clear skies and increased with increasing elevation.

We proposed a post-reanalysis correction algorithm based on the dependence of the bias on sky clearness and surface elevation. The correction algorithm worked well on the annual scale for the sites in the North America, reducing the annual mean bias errors from +37.2 W m^{-2} and +20.2 W m^{-2} to +1.3 W m^{-2} and +2.7 W m^{-2} for NARR and MERRA, respectively. The algorithm also showed good performance for the BSRN sites outside North America.

Although the algorithm was able to reduce the overall mean bias errors in surface incoming solar radiation modeled by NARR and MERRA, there are a few limitations to this algorithm. First, the algorithm does not help much on improving the modeled interannual variability of surface incoming solar radiation for the two products.

Second, the algorithm might have overcorrection problem for some specific locations, such as the four sites near the equator in our selected sites.

We also applied the correction algorithm to the whole global domain of MERRA data for the year 2000 to 2004 to revise the current estimate of global mean *S*. The algorithm reduced the MERRA modeled global mean *S* by 9.0% to 175.5 W m^{-2}. This corrected *S* is lower than that estimated by *Stephens et al.* [2012a] and *Trenberth et al.* [2009]. This research calls for attentions and more work needed on the problem of overestimation of surface incoming solar radiation by most GCMs.

5.1.2 Strong contributions of local background climate to UHIs

This study quantifies for the first time the primary causes of the urban heat island effect on the large spatial scale. We used MODIS data of land surface temperature to calculate the UHI intensity (ΔT) at both daytime and nighttime for 65 cities evenly distributed across North America. The MODIS results showed that the annual mean midnight ΔT is positively correlated with the logarithm of population, but is statistically invariant with climate, showing insignificant correlation with precipitation ($r = 0.05$, $P = 0.70$), solar radiation ($r = 0.15$, $P > 0.20$), and air temperature ($r = 0.20$, $P > 0.10$). However, the annual mean midday ΔT is strongly correlated with precipitation ($r = 0.74$, $P < 0.001$) and has a weaker correlation with population size than does the midnight ΔT ($r = 0.27$, $P = 0.027$). We used a climate model – CESM and a ΔT attribution method, to show that this geographic patter in daytime ΔT is largely explained by change in convection efficiency between urban

and rural areas. This convection effect actually depends on the local background climate, contributing 3.0 ± 0.3 K (mean ± 1 standard error, s. e.) warming to daytime ΔT in cities in humid climate but causing 1.5 ± 0.2 K cooling in dry climate. At nighttime, results reaffirmed the consensus view that, regardless of the local climate, the release of the heat stored in the built-up structures is the dominant contributor to nighttime ΔT.

This study also showed that in the humid eastern United States, the annual daytime ΔT is negatively correlated to annual precipitation. This means that there is higher ΔT in dried years. These relationships imply that UHIs will exacerbate heatwave stress on human health in wet climates where high temperature effects are already compounded by high air humidity and in drier years when positive temperature anomalies may be reinforced by a precipitation–temperature feedback.

The ΔT attribution results also reaffirmed that the city albedo management is a viable means of mitigating ΔT on large scales.

5.1.3 UHI in the future

In this study, we ran the CLM simulation under Representative Concentration Pathway 8.5 scenario from 2005 to 2100. Results show that the daytime ΔT generally decreases across all three climate zones because urban and rural areas respond differently to climate change. The ΔT attribution results show that the climate change made changes in the contributions of certain biophysical processes to ΔT. At daytime,

because of the increasing vegetation in the future, the contribution of convection efficiency to ΔT increases in the dry and continental climates, but decreases in the temperate region. The contribution of radiation also drops compared to that in current climate, because the denser vegetation in the rural areas darkens the rural surfaces in the future.

At nighttime, there are two major changes in the biophysical contributions to ΔT compared to that in the current climate. First, the contribution of the release of the stored heat increases in the future across all three climates. This is because of the overestimated surface solar radiation by CESM and the increased longwave radiative forcing due to the global warming. Second, the contribution of evaporation significantly decreases in the future. This is because the urban landunit responses stronger to the increased precipitation than do the rural areas. But this might be because of the primitive scheme of urban pervious surface in the CLM.

This study also revealed the overestimation of the surface incoming solar radiation in CESM. There is a sharp inconsistency between the modeled period driven by corrected reanalysis dataset and the period driven by CESM pure model outputs.

5.2 Contributions of the dissertation

Through the completion of this dissertation, the following contributions have been made:

1) Our work emphasizes the importance of improving the accuracy of surface incoming solar radiation modeled by both GCMs and reanalysis systems. The overestimated surface radiation will not only cause the inaccurate estimate of global surface energy budget, but also result in systematic bias errors in projected surface climate by various climate models.

2) A computationally efficient post-reanalysis correction algorithm is proposed for the end users engaged in the applications using NARR and MERRA radiation products.

3) This dissertation, for the first time, quantifies the contribution of each biophysical process to urban heat island. A long-held perception is that reduction in evaporative cooling in urban land is the dominant driver of UHI. However, we used a climate model to show that this common perception is erroneous. It is the changes in convection efficiency between urban and rural areas that largely explain the spatial variation of daytime UHI. This convection effect depends on local background climate.

4) A ΔT attribution method was proposed. This method, derived from the surface energy balance equation, attributes changes in surface temperature into contributions from difference biophysical processes. This method was used in the diagnostic way in this dissertation. It can also be used in a prognostic way. For example, this method can be used to predict the surface temperature change in response to changes in land surface properties such as land management.

5) Changes in UHI and urban land – atmosphere interactions with climate change in the future were examined.

5.3 Future works

Building off of my present research, this dissertation has opened up a number of new directions for future studies.

5.3.1 Surface incoming solar radiation

My present study has showed that two data assimilation systems persistently overestimate incoming solar radiation at the Earth's surface because of the underestimation of the cloud absorption. This overestimation problem exists almost every global climate model (average bias: 2 – 24 W m^{-2}) [*Wild et al.*, 2013]. Incoming solar radiation is an important driver of surface energy exchange. An overestimated incoming solar radiation in the model must lead to a biased prediction of surface temperature solved from the surface energy balance equation. However, there is little quantitative knowledge on how the extra solar radiation will affect the surface temperature prediction and the modeled surface energy fluxes. Future direction can be investigating the sensitivity of modeled surface climate to overloaded surface incoming solar radiation in the climate models.

Considerable uncertainties exist in the CMIP5 climate model projections [*Knutti and Sedlacek*, 2013]. If the future direction described above shows that the surface temperature responds significantly to the surface incoming solar radiation, then the high bias of surface incoming solar radiation in the climate models could be a

significant driver of the uncertainties in surface temperature projections by CMIP5 GCMs.

5.3.2 Climate mitigations through land-use management

The local to regional warming trends are quite different than the observed global warming trend [*Stone et al.*, 2012]. Land use/land cover changes account for more than 50% of the observed warming trend at local to regional scales [*Kalnay and Cai*, 2003; *Zhou et al.*, 2004]. To adapt to the climate change, mitigation strategies such as urban management are needed for future development planning. A major challenge faced by humanity is the lack of quantitative assessment of land management strategies. Although a number of recent modeling studies evaluated a series of urban adaptation strategies by implementing them in the model [*Georgescu et al.*, 2014; *Li et al.*, 2014; *Stone et al.*, 2013], considerable uncertainties exist due to the choice of modeling systems and the relatively arbitrary and unrealistic strategy implementation in the models.

The ΔT attribution model that we proposed in this dissertation can be used in a prognostic way. It can mechanistically demonstrate what biophysical processes would be affected and how much each process would contribute to mitigate the warming if land management strategies are implemented. Applying this theoretical model on either observed or modeled data could predict and assess the cooling effects of various mitigation strategies. Because this model, independent of any climate models, is derived from surface energy balance equation, it would provide more robust

benchmark results of quantifying the mitigation effects than the simulation results using any specific climate models. The insights gained from this work would be of great help to policy makers for designing climate mitigation strategies and planning the future development.

5.3.3 Effects of Land use/land cover change on land-atmosphere interactions

This dissertation has investigated the contributions of local background climate to urban heat islands over North American cities. The work can be expanded to other regions in the Earth including China and India where rapid urbanization is happening. Studies over these places could generate new insights.

In addition, urbanization is only one example of the human-induced changes to the Earth's surface. All types of land use activities such as deforestation and afforestation affect the Earth's surface climate. Therefore future work could be extended to other types of land use change activities. The future research questions include: How do surface climate and land-atmosphere interactions respond to other types of land surface changes? How do these interactions change with climate change? How do these interactions vary in different climate zones? Does land use change affect not only the mean climate state but also the extreme events?

References

Akbari, H., S. Menon, and A. Rosenfeld (2009), Global cooling: increasing world-wide urban albedos to offset CO2, *Climatic Change*, *94*(3-4), 275-286, doi:Doi 10.1007/S10584-008-9515-9.

Arnfield, A. J. (2003), Two decades of urban climate research: A review of turbulence, exchanges of energy and water, and the urban heat island, *International Journal of Climatology*, *23*(1), 1-26.

Baldocchi, D., et al. (2001), FLUXNET: A new tool to study the temporal and spatial variability of ecosystem-scale carbon dioxide, water vapor, and energy flux densities, *Bulletin of the American Meteorological Society*, *82*(11), 2415-2434.

Baldocchi, D., C. A. Vogel, and B. Hall (1997), Seasonal variation of energy and water vapor exchange rates above and below a boreal jack pine forest canopy, *Journal of Geophysical Research-Atmospheres*, *102*(D24), 28939-28951.

Bergeron, O., H. A. Margolis, T. A. Black, C. Coursolle, A. L. Dunn, A. G. Barr, and S. C. Wofsy (2007), Comparison of carbon dioxide fluxes over three boreal black spruce forests in Canada, *Global Change Biology*, *13*(1), 89-107.

Best, M. J., C. S. B. Grimmond, and M. G. Villani (2006), Evaluation of the urban tile in MOSES using surface energy balance observations, *Boundary-Layer Meteorology*, *118*(3), 503-525.

Bettencourt, L., and G. West (2010), A unified theory of urban living, *Nature*, *467*(7318), 912-913.

Betts, A. K., J. H. Ball, A. C. M. Beljaars, M. J. Miller, and P. A. Viterbo (1996), The land surface-atmosphere interaction: A review based on observational and global modeling perspectives, *Journal of Geophysical Research-Atmospheres*, *101*(D3), 7209-7225.

Blanken, P. D., T. A. Black, P. C. Yang, H. H. Neumann, Z. Nesic, R. Staebler, G. den Hartog, M. D. Novak, and X. Lee (1997), Energy balance and canopy conductance of a boreal aspen forest: Partitioning overstory and understory components, *Journal of Geophysical Research-Atmospheres*, *102*(D24), 28915-28927.

Bloom, S. C., L. L. Takacs, A. M. DaSilva, and D. Ledvina (1996), Data assimilation using incremental analysis updates, *Mon. Weather Rev.*, *124*(6), 1256-1271.

Bonan, G. B. (2008), Forests and climate change: Forcings, feedbacks, and the climate benefits of forests, *Science*, *320*(5882), 1444-1449.

Bosilovich, M. G., F. R. Robertson, and J. Y. Chen (2011), Global Energy and Water Budgets in MERRA, *Journal of Climate*, *24*(22), 5721-5739.

Chen, F., et al. (2011), The integrated WRF/urban modelling system: development, evaluation, and applications to urban environmental problems, *International Journal of Climatology*, *31*(2), 273-288.

Chou, M.-D., and M. J. Suarez (1999), A solar radiation parameterization for atmospheric studies, *NASA Tech. Rep. NASA/TM-1999-104606*, 40 pp, Series on Global Modeling and Data Assimilation.

Chou, M.-D., M. J. Suarez, X. Z. Liang, and M. M.-H. Yan (2001), A thermal infrared radiation parameterization for atmospheric studies, *NASA Tech. Rep.*

NASA/TM-2001-104606, 56 pp, Series on Global Modeling and Data Assimilation.

Clark, K. L., N. Skowronski, and J. Hom (2010), Invasive insects impact forest carbon dynamics, *Global Change Biology*, *16*(1), 88-101.

Clinton, N., and P. Gong (2013), MODIS detected surface urban heat islands and sinks: Global locations and controls, *Remote Sensing of Environment*, *134*, 294-304, doi:Doi 10.1016/J.Rse.2013.03.008.

Cullather, R. I., and M. G. Bosilovich (2012), The Energy Budget of the Polar Atmosphere in MERRA, *Journal of Climate*, *25*(1), 5-24.

Dandou, A., M. Tombrou, E. Akylas, N. Soulakellis, and E. Bossioli (2005), Development and evaluation of an urban parameterization scheme in the Penn State/NCAR Mesoscale Model (MM5), *Journal of Geophysical Research-Atmospheres*, *110*(D10).

Decker, M., M. A. Brunke, Z. Wang, K. Sakaguchi, X. B. Zeng, and M. G. Bosilovich (2012), Evaluation of the Reanalysis Products from GSFC, NCEP, and ECMWF Using Flux Tower Observations, *Journal of Climate*, *25*(6), 1916-1944.

Dore, S., T. E. Kolb, M. Montes-Helu, B. W. Sullivan, W. D. Winslow, S. C. Hart, J. P. Kaye, G. W. Koch, and B. A. Hungate (2008), Long-term impact of a stand-replacing fire on ecosystem CO(2) exchange of a ponderosa pine forest, *Global Change Biology*, *14*(8), 1801-1820.

Dupont, S., T. L. Otte, and J. K. S. Ching (2004), Simulation of meteorological fields within and above urban and rural canopies with a mesoscale model (MM5), *Boundary-Layer Meteorology*, *113*(1), 111-158.

Duynkerke, P. G., and J. Teixeira (2001), Comparison of the ECMWF reanalysis with FIRE I observations: Diurnal variation of marine stratocumulus, *Journal of Climate*, *14*(7), 1466-1478.

Fels, S. B., and M. D. Schwarzkopf (1975), Simplified Exchange Approximation - New Method for Radiative-Transfer Calculations, *Journal of the Atmospheric Sciences*, *32*(7), 1475-1488.

Ferrier, B. S., Y. Jin, Y. Lin, T. Black, E. Rogers, and G. DiMego (2002), Implementation of a new grid-scale cloud and precipitation scheme in the NCEP Eta Model, paper presented at 19th Conf. on Weather Analysis and Forecasting/15th Conf. on Numerical Weather Prediction, Amer. Meteor. Soc., San Antonio, TX.

Fischer, E. M., K. W. Oleson, and D. M. Lawrence (2012), Contrasting urban and rural heat stress responses to climate change, *Geophysical Research Letters*, *39*.

Fischer, E. M., and C. Schar (2010), Consistent geographical patterns of changes in high-impact European heatwaves, *Nat Geosci*, *3*(6), 398-403, doi:Doi 10.1038/Ngeo866.

Frauenfeld, O. W., T. J. Zhang, and M. C. Serreze (2005), Climate change and variability using European Centre for Medium-Range Weather Forecasts reanalysis (ERA-40) temperatures on the Tibetan Plateau, *Journal of Geophysical Research-Atmospheres*, *110*(D2).

Gallo, K. P., J. O. Adegoke, T. W. Owen, and C. D. Elvidge (2002), Satellite-based detection of global urban heat-island temperature influence, *Journal of Geophysical Research-Atmospheres*, *107*(D24), doi:10.1029/2002jd002588.

Garratt, J. R. (1994), *The atmospheric boundary layer*, Cambridge university press.

Georgescu, M., P. E. Morefield, B. G. Bierwagen, and C. P. Weaver (2014), Urban adaptation can roll back warming of emerging megapolitan regions, *Proceedings of the National Academy of Sciences of the United States of America*, *111*(8), 2909-2914, doi:Doi 10.1073/Pnas.1322280111.

Georgescu, M., M. Moustaoui, A. Mahalov, and J. Dudhia (2013), Summer-time climate impacts of projected megapolitan expansion in Arizona, *Nat Clim Change*, *3*(1), 37-41.

Gholz, H. L., and K. L. Clark (2002), Energy exchange across a chronosequence of slash pine forests in Florida, *Agricultural and Forest Meteorology*, *112*(2), 87-102.

Giannaros, T. M., and D. Melas (2012), Study of the urban heat island in a coastal Mediterranean City: The case study of Thessaloniki, Greece, *Atmos. Res.*, *118*, 103-120.

Gilmanov, T. G., L. L. Tieszen, B. K. Wylie, L. B. Flanagan, A. B. Frank, M. R. Haferkamp, T. P. Meyers, and J. A. Morgan (2005), Integration of CO2 flux and remotely-sensed data for primary production and ecosystem respiration analyses in the Northern Great Plains: potential for quantitative spatial extrapolation, *Global Ecology and Biogeography*, *14*(3), 271-292.

Grimm, N. B., S. H. Faeth, N. E. Golubiewski, C. L. Redman, J. G. Wu, X. M. Bai, and J. M. Briggs (2008), Global change and the ecology of cities, *Science*, *319*(5864), 756-760.

Grimmond, C. S. B. (2006), Progress in measuring and observing the urban atmosphere, *Theoretical and Applied Climatology*, *84*(1-3), 3-22.

Grimmond, C. S. B., et al. (2010), The International Urban Energy Balance Models Comparison Project: First Results from Phase 1, *Journal of Applied Meteorology and Climatology*, *49*(6), 1268-1292.

Grimmond, C. S. B., and T. R. Oke (2002), Turbulent heat fluxes in urban areas: Observations and a local-scale urban meteorological parameterization scheme (LUMPS), *Journal of Applied Meteorology*, *41*(7), 792-810.

Grimmond, S. (2007), Urbanization and global environmental change: local effects of urban warming, *Geographical Journal*, *173*, 83-88.

Gu, L. H., J. D. Fuentes, H. H. Shugart, R. M. Staebler, and T. A. Black (1999), Responses of net ecosystem exchanges of carbon dioxide to changes in cloudiness: Results from two North American deciduous forests, *Journal of Geophysical Research-Atmospheres*, *104*(D24), 31421-31434.

Gu, L. H., T. Meyers, S. G. Pallardy, P. J. Hanson, B. Yang, M. Heuer, K. P. Hosman, J. S. Riggs, D. Sluss, and S. D. Wullschleger (2006), Direct and indirect effects of atmospheric conditions and soil moisture on surface energy partitioning revealed by a prolonged drought at a temperate forest site, *Journal of Geophysical Research-Atmospheres*, *111*(D16).

Hansen, J., M. Sato, and R. Ruedy (2012), Perception of climate change, *Proceedings of the National Academy of Sciences of the United States of America*, *109*(37), E2415-E2423, doi:Doi 10.1073/Pnas.1205276109.

Harman, I. N., J. F. Barlow, and S. E. Belcher (2004), Scalar fluxes from urban street canyons. Part II: Model, *Boundary-Layer Meteorology*, *113*(3), 387-409.

Hatzianastassiou, N., C. Matsoukas, A. Fotiadi, K. G. Pavlakis, E. Drakakis, D. Hatzidimitriou, and I. Vardavas (2005), Global distribution of Earth's surface shortwave radiation budget, *Atmospheric Chemistry and Physics*, *5*, 2847-2867.

Hickman, J. E., S. L. Wu, L. J. Mickley, and M. T. Lerdau (2010), Kudzu (Pueraria montana) invasion doubles emissions of nitric oxide and increases ozone pollution, *Proceedings of the National Academy of Sciences of the United States of America*, *107*(22), 10115-10119.

Hicks, B. B., W. J. Callahan, and M. A. Hoekzema (2010), On the Heat Islands of Washington, DC, and New York City, NY, *Boundary-Layer Meteorology*, *135*(2), 291-300.

Hollinger, D. Y., S. M. Goltz, E. A. Davidson, J. T. Lee, K. Tu, and H. T. Valentine (1999), Seasonal patterns and environmental control of carbon dioxide and water vapour exchange in an ecotonal boreal forest, *Global Change Biology*, *5*(8), 891-902.

Hollinger, S. E., C. J. Bernacchi, and T. P. Meyers (2005), Carbon budget of mature no-till ecosystem in North Central Region of the United States, *Agricultural and Forest Meteorology*, *130*(1-2), 59-69.

Humphreys, E. R., T. A. Black, G. J. Ethier, G. B. Drewitt, D. L. Spittlehouse, E. M. Jork, Z. Nesic, and N. J. Livingston (2003), Annual and seasonal variability of sensible and latent heat fluxes above a coastal Douglas-fir forest, British Columbia, Canada, *Agricultural and Forest Meteorology*, *115*(1-2), 109-125.

Humphreys, E. R., T. A. Black, K. Morgenstern, T. B. Cai, G. B. Drewitt, Z. Nesic, and J. A. Trofymow (2006), Carbon dioxide fluxes in coastal Douglas-fir stands at different stages of development after clearcut harvesting, *Agricultural and Forest Meteorology*, *140*(1-4), 6-22.

Hung, T., D. Uchihama, S. Ochi, and Y. Yasuoka (2006), Assessment with satellite data of the urban heat island effects in Asian mega cities, *Int J Appl Earth Obs*, *8*(1), 34-48, doi:Doi 10.1016/J.Jag.2005.05.003.

Hurrell, J. W., et al. (2013), The Community Earth System Model A Framework for Collaborative Research, *Bulletin of the American Meteorological Society*, *94*(9), 1339-1360, doi:Doi 10.1175/Bams-D-12-00121.1.

Imhoff, M. L., P. Zhang, R. E. Wolfe, and L. Bounoua (2010), Remote sensing of the urban heat island effect across biomes in the continental USA, *Remote Sensing of Environment*, *114*(3), 504-513.

Jarvis, P. G., J. M. Massheder, S. E. Hale, J. B. Moncrieff, M. Rayment, and S. L. Scott (1997), Seasonal variation of carbon dioxide, water vapor, and energy exchanges of a boreal black spruce forest, *Journal of Geophysical Research-Atmospheres*, *102*(D24), 28953-28966.

Jimenez, C., et al. (2011), Global intercomparison of 12 land surface heat flux estimates, *Journal of Geophysical Research-Atmospheres*, *116*.

Jung, M., et al. (2011), Global patterns of land-atmosphere fluxes of carbon dioxide, latent heat, and sensible heat derived from eddy covariance, satellite, and meteorological observations, *Journal of Geophysical Research-Biogeosciences*, *116*.

Kalnay, E., and M. Cai (2003), Impact of urbanization and land-use change on climate, *Nature*, *423*(6939), 528-531.

Kalnay, E., et al. (1996), The NCEP/NCAR 40-year reanalysis project, *Bulletin of the American Meteorological Society*, *77*(3), 437-471.

Kato, S., N. G. Loeb, F. G. Rose, D. R. Doelling, D. A. Rutan, T. E. Caldwell, L. S. Yu, and R. A. Weller (2013), Surface Irradiances Consistent with CERES-Derived Top-of-Atmosphere Shortwave and Longwave Irradiances, *Journal of Climate*, *26*(9), 2719-2740.

Kennedy, A. D., X. Q. Dong, B. K. Xi, S. C. Xie, Y. Y. Zhang, and J. Y. Chen (2011), A Comparison of MERRA and NARR Reanalyses with the DOE ARM SGP Data, *Journal of Climate*, *24*(17), 4541-4557.

Kiehl, J. T., and K. E. Trenberth (1997), Earth's annual global mean energy budget, *Bulletin of the American Meteorological Society*, *78*(2), 197-208.

Knutti, R., and J. Sedlacek (2013), Robustness and uncertainties in the new CMIP5 climate model projections, *Nat Clim Change*, *3*(4), 369-373, doi:Doi 10.1038/Nclimate1716.

Kondo, H., Y. Genchi, Y. Kikegawa, Y. Ohashi, H. Yoshikado, and H. Komiyama (2005), Development of a multi-layer urban canopy model for the analysis of energy consumption in a big city: Structure of the urban canopy model and its basic performance, *Boundary-Layer Meteorology*, *116*(3), 395-421.

Krishnan, P., T. P. Meyers, R. L. Scott, L. Kennedy, and M. Heuer (2012), Energy exchange and evapotranspiration over two temperate semi-arid grasslands in North America, *Agricultural and Forest Meteorology*, *153*, 31-44.

Lacis, A. A., and J. E. Hansen (1974), Parameterization for Absorption of Solar-Radiation in Earths Atmosphere, *Journal of the Atmospheric Sciences*, *31*(1), 118-133.

Landsberg, H. E. (1981), The Urban Climate, *International Geophysical Series*, *28*, 275.

Lee, X., J. D. Fuentes, R. M. Staebler, and H. H. Neumann (1999), Long-term observation of the atmospheric exchange of CO2 with a temperate deciduous forest in southern Ontario, Canada, *Journal of Geophysical Research-Atmospheres*, *104*(D13), 15975-15984.

Lee, X., et al. (2011), Observed increase in local cooling effect of deforestation at higher latitudes, *Nature*, *479*(7373), 384-387.

Lemonsu, A., C. S. B. Grimmond, and V. Masson (2004), Modeling the surface energy balance of the core of an old Mediterranean city: Marseille, *Journal of Applied Meteorology*, *43*(2), 312-327.

Leung, L. R., and W. I. Gustafson (2005), Potential regional climate change and implications to US air quality, *Geophysical Research Letters*, *32*(16).

Li, D., and E. Bou-Zeid (2013), Synergistic Interactions between Urban Heat Islands and Heat Waves: The Impact in Cities Is Larger than the Sum of Its Parts*,

Journal of Applied Meteorology and Climatology, *52*(9), 2051-2064, doi:Doi 10.1175/Jamc-D-13-02.1.

Li, D., E. Bou-Zeid, and M. Oppenheimer (2014), The effectiveness of cool and green roofs as urban heat island mitigation strategies, *Environ. Res. Lett.*, *9*(5), doi:Artn 055002 Doi 10.1088/1748-9326/9/5/055002.

Ma, S. Y., D. D. Baldocchi, L. K. Xu, and T. Hehn (2007), Inter-annual variability in carbon dioxide exchange of an oak/grass savanna and open grassland in California, *Agricultural and Forest Meteorology*, *147*(3-4), 157-171.

Mackey, C. W., X. Lee, and R. B. Smith (2012), Remotely sensing the cooling effects of city scale efforts to reduce urban heat island, *Build Environ*, *49*, 348-358, doi:Doi 10.1016/J.Buildenv.2011.08.004.

Markovic, M., C. G. Jones, K. Winger, and D. Paquin (2009), The surface radiation budget over North America: gridded data assessment and evaluation of regional climate models, *International Journal of Climatology*, *29*(15), 2226-2240.

Martilli, A., A. Clappier, and M. W. Rotach (2002), An urban surface exchange parameterisation for mesoscale models, *Boundary-Layer Meteorology*, *104*(2), 261-304.

Masson, V. (2000), A physically-based scheme for the urban energy budget in atmospheric models, *Boundary-Layer Meteorology*, *94*(3), 357-397.

Masson, V., C. S. B. Grimmond, and T. R. Oke (2002), Evaluation of the Town Energy Balance (TEB) scheme with direct measurements from dry districts in two cities, *Journal of Applied Meteorology*, *41*(10), 1011-1026.

Mesinger, F., et al. (2006), North American regional reanalysis, *Bulletin of the American Meteorological Society*, *87*(3), 343-+.

Mickley, L. J., D. J. Jacob, B. D. Field, and D. Rind (2004), Climate response to the increase in tropospheric ozone since preindustrial times: A comparison between ozone and equivalent CO2 forcings, *Journal of Geophysical Research-Atmospheres*, *109*(D5).

Monson, R. K., A. A. Turnipseed, J. P. Sparks, P. C. Harley, L. E. Scott-Denton, K. Sparks, and T. E. Huxman (2002), Carbon sequestration in a high-elevation, subalpine forest, *Global Change Biology*, *8*(5), 459-478.

Moss, R. H., et al. (2010), The next generation of scenarios for climate change research and assessment, *Nature*, *463*(7282), 747-756, doi:Doi 10.1038/Nature08823.

Mu, Q. Z., M. S. Zhao, and S. W. Running (2011), Improvements to a MODIS global terrestrial evapotranspiration algorithm, *Remote Sensing of Environment*, *115*(8), 1781-1800.

Nichol, J. E., W. Y. Fung, K. S. Lam, and M. S. Wong (2009), Urban heat island diagnosis using ASTER satellite images and 'in situ' air temperature, *Atmos. Res.*, *94*(2), 276-284, doi:Doi 10.1016/J.Atmosres.2009.06.011.

Nolte, C. G., A. B. Gilliland, C. Hogrefe, and L. J. Mickley (2008), Linking global to regional models to assess future climate impacts on surface ozone levels in the United States, *Journal of Geophysical Research-Atmospheres*, *113*(D14).

Noormets, A., M. J. Gavazzi, S. G. McNulty, J. C. Domec, G. Sun, J. S. King, and J. Q. Chen (2010), Response of carbon fluxes to drought in a coastal plain loblolly pine forest, *Global Change Biology*, *16*(1), 272-287.

Ohmura, A., et al. (1998), Baseline Surface Radiation Network (BSRN/WCRP): New precision radiometry for climate research, *Bulletin of the American Meteorological Society*, *79*(10), 2115-2136.

Oke, T. R. (1973), City size and the urban heat island, *Atmospheric Environment (1967)*, *7*(8), 769-779, doi:http://dx.doi.org/10.1016/0004-6981(73)90140-6.

Oke, T. R. (1976), The distinction between canopy and boundary-layer urban heat islands, *Atmosphere*, *14*(4), 268-277, doi:10.1080/00046973.1976.9648422.

Oke, T. R. (1981), Canyon Geometry and the Nocturnal Urban Heat-Island - Comparison of Scale Model and Field Observations, *Journal of Climatology*, *1*(3), 237-&.

Oke, T. R. (1982), The Energetic Basis of the Urban Heat-Island, *Quarterly Journal of the Royal Meteorological Society*, *108*(455), 1-24.

Oke, T. R. (1987), - Boundary layer climates.

Oleson, K. (2012), Contrasts between Urban and Rural Climate in CCSM4 CMIP5 Climate Change Scenarios, *Journal of Climate*, *25*(5), 1390-1412.

Oleson, K., G. B. Bonan, J. Feddema, and T. Jackson (2011), An examination of urban heat island characteristics in a global climate model, *International Journal of Climatology*, *31*(12), 1848-1865.

Oleson, K., G. B. Bonan, J. Feddema, and M. Vertenstein (2008a), An urban parameterization for a global climate model. Part II: Sensitivity to input parameters and the simulated urban heat island in offline Simulations, *Journal of Applied Meteorology and Climatology*, *47*(4), 1061-1076.

Oleson, K., G. B. Bonan, J. Feddema, M. Vertenstein, and C. S. B. Grimmond (2008b), An urban parameterization for a global climate model. Part I: Formulation and evaluation for two cities, *Journal of Applied Meteorology and Climatology*, *47*(4), 1038-1060.

Oleson, K., D. M. Lawrence, G. Bonan, G. M. Flanner, E. Kluzek, J. P. Lawrence, S. Levis, C. S. Swenson, and E. P. Thornton (2010), Technical description of version 4.0 of the Community Land Model (CLM), *NCAR Tech. Note Rep. NCAR/TN-478+STR*, 257 pp.

Oren, R., C. I. Hseih, P. Stoy, J. Albertson, H. R. McCarthy, P. Harrell, and G. G. Katul (2006), Estimating the uncertainty in annual net ecosystem carbon exchange: spatial variation in turbulent fluxes and sampling errors in eddy-covariance measurements, *Global Change Biology*, *12*(5), 883-896.

Otte, T. L., A. Lacser, S. Dupont, and J. K. S. Ching (2004), Implementation of an urban canopy parameterization in a mesoscale meteorological model, *Journal of Applied Meteorology*, *43*(11), 1648-1665.

Peng, S. S., S. L. Piao, P. Ciais, P. Friedlingstein, C. Ottle, F. M. Breon, H. J. Nan, L. M. Zhou, and R. B. Myneni (2012), Surface Urban Heat Island Across 419 Global Big Cities, *Environ. Sci. Technol.*, *46*(2), 696-703.

Piringer, M., et al. (2002), Investigating the surface energy balance in urban areas - Recent advances and future needs, in *Urban Air Quality - Recent Advances, Proceedings*, edited, pp. 1-16, Springer, Dordrecht.

Qian, T. T., A. Dai, K. E. Trenberth, and K. W. Oleson (2006), Simulation of global land surface conditions from 1948 to 2004. Part I: Forcing data and evaluations, *J. Hydrometeorol.*, *7*(5), 953-975.

Raupach, M. R. (1994), Simplified Expressions for Vegetation Roughness Length and Zero-Plane Displacement as Functions of Canopy Height and Area Index, *Boundary-Layer Meteorology*, *71*(1-2), 211-216, doi:Doi 10.1007/Bf00709229.

Richardson, A. D., X. Lee, and A. J. Friedland (2004), Microclimatology of treeline spruce-fir forests in mountains of the northeastern United States, *Agricultural and Forest Meteorology*, *125*(1-2), 53-66.

Rienecker, M. M., et al. (2011), MERRA: NASA's Modern-Era Retrospective Analysis for Research and Applications, *Journal of Climate*, *24*(14), 3624-3648.

Rosenzweig, C., et al. (2009), MITIGATING NEW YORK CITY'S HEAT ISLAND Integrating Stakeholder Perspectives and Scientific Evaluation, *Bulletin of the American Meteorological Society*, *90*(9), 1297-1312.

Rossow, W. B., and Y. C. Zhang (1995), Calculation of Surface and Top of Atmosphere Radiative Fluxes from Physical Quantities Based on Isccp Data Sets .2. Validation and First Results, *Journal of Geophysical Research-Atmospheres*, *100*(D1), 1167-1197.

Rotenberg, E., and D. Yakir (2010), Contribution of Semi-Arid Forests to the Climate System, *Science*, *327*(5964), 451-454.

Roth, M., and W. T. L. Chow (2012), A historical review and assessment of urban heat island research in Singapore, *Singap. J. Trop. Geogr.*, *33*(3), 381-397.

Roth, M., T. R. Oke, and W. J. Emery (1989), Satellite-Derived Urban Heat Islands from 3 Coastal Cities and the Utilization of Such Data in Urban Climatology, *Int. J. Remote Sens.*, *10*(11), 1699-1720.

Schar, C., P. L. Vidale, D. Luthi, C. Frei, C. Haberli, M. A. Liniger, and C. Appenzeller (2004), The role of increasing temperature variability in European summer heatwaves, *Nature*, *427*(6972), 332-336, doi:Doi 10.1038/Nature02300.

Schmid, H. P., C. S. B. Grimmond, F. Cropley, B. Offerle, and H. B. Su (2000), Measurements of CO2 and energy fluxes over a mixed hardwood forest in the mid-western United States, *Agricultural and Forest Meteorology*, *103*(4), 357-374.

Schmid, H. P., H. B. Su, C. S. Vogel, and P. S. Curtis (2003), Ecosystem-atmosphere exchange of carbon dioxide over a mixed hardwood forest in northern lower Michigan, *Journal of Geophysical Research-Atmospheres*, *108*(D14).

Schmidt, A., C. Hanson, W. S. Chan, and B. E. Law (2012), Empirical assessment of uncertainties of meteorological parameters and turbulent fluxes in the AmeriFlux network, *Journal of Geophysical Research-Biogeosciences*, *117*.

Smith, T. T., B. F. Zaitchik, and J. M. Gohlke (2013), Heat waves in the United States: definitions, patterns and trends, *Climatic Change*, *118*(3-4), 811-825, doi:Doi 10.1007/S10584-012-0659-2.

Souch, C., and S. Grimmond (2006), Applied climatology: urban climate, *Progress in Physical Geography*, *30*(2), 270-279.

Stephens, G. L., J. Li, M. Wild, C. A. Clayson, N. Loeb, S. Kato, T. L'Ecuyer, P. W. Stackhouse, M. Lebsock, and T. Andrews (2012a), An update on Earth's energy balance in light of the latest global observations, *Nature Geosci*, *5*(10), 691-696.

Stephens, G. L., M. Wild, P. W. Stackhouse, T. L'Ecuyer, S. Kato, and D. S. Henderson (2012b), The Global Character of the Flux of Downward Longwave Radiation, *Journal of Climate*, *25*(7), 2329-2340.

Stevens, B., A. Beljaars, S. Bordoni, C. Holloway, M. Kohler, S. Krueger, V. Savic-Jovcic, and Y. Y. Zhang (2007), On the structure of the lower troposphere in the summertime stratocumulus regime of the northeast Pacific, *Mon. Weather Rev.*, *135*(3), 985-1005.

Stone, B., J. Vargo, and D. Habeeb (2012), Managing climate change in cities: Will climate action plans work?, *Landscape Urban Plan*, *107*(3), 263-271, doi:Doi 10.1016/J.Landurbplan.2012.05.014.

Stone, B., J. Vargo, P. Liu, D. Habeeb, A. DeLucia, M. Trail, Y. T. Hu, and A. Russell (2014), Avoided Heat-Related Mortality through Climate Adaptation Strategies in Three US Cities, *Plos One*, *9*(6), doi:ARTN e100852 DOI 10.1371/journal.pone.0100852.

Stone, B., J. Vargo, P. Liu, Y. T. Hu, and A. Russell (2013), Climate Change Adaptation Through Urban Heat Management in Atlanta, Georgia, *Environ. Sci. Technol.*, *47*(14), 7780-7786, doi:Doi 10.1021/Es304352e.

Taha, H. (1997), Urban climates and heat islands: Albedo, evapotranspiration, and anthropogenic heat, *Energy Build.*, *25*(2), 99-103, doi:Doi 10.1016/S0378-7788(96)00999-1.

Taylor, A. E., R. J. Stouffer, and G. A. Meehl (2009), A summary of the CMIP5 experiment design, *World Climate Research Program*, *[Available at* http://cmip-pcmdi.llnl.gov/cmip5/docs/Taylor_CMIP5_design.pdf.%5D, 32.

Tereshchenko, I. E., and A. E. Filonov (2001), Air temperature fluctuations in Guadalajara, Mexico, from 1926 to 1994 in relation to urban growth, *International Journal of Climatology*, *21*(4), 483-494.

Trenberth, K. E., J. T. Fasullo, and J. Kiehl (2009), Earth's Global Energy Budget, *Bulletin of the American Meteorological Society*, *90*(3), 311-+.

Viterbo, P. A., and P. Courtier (1995), The importance of soil water for medium-range weather forecasting., paper presented at Implications for data assimilation, Workshop on Imbalance of Slowly Varying Components of Predictable Atmospheric Motions, World Meteorol. Org., Beijing, China.

Voogt, J. A., and C. S. B. Grimmond (2000), Modeling surface sensible heat flux using surface radiative temperatures in a simple urban area, *Journal of Applied Meteorology*, *39*(10), 1679-1699.

Voogt, J. A., and T. R. Oke (1997), Complete urban surface temperatures, *Journal of Applied Meteorology*, *36*(9), 1117-1132.

Voogt, J. A., and T. R. Oke (2003), Thermal remote sensing of urban climates, *Remote Sensing of Environment*, *86*(3), 370-384.

Walsh, J. E., W. L. Chapman, and D. H. Portis (2009), Arctic Cloud Fraction and Radiative Fluxes in Atmospheric Reanalyses, *Journal of Climate*, *22*(9), 2316-2334.

Wang, A., and X. Zeng (2012), Evaluation of multireanalysis products with in situ observations over the Tibetan Plateau, *J. Geophys. Res.*, *117*(D5), D05102, doi:10.1029/2011jd016553.

Wang, K. C., J. K. Wang, P. C. Wang, M. Sparrow, J. Yang, and H. B. Chen (2007), Influences of urbanization on surface characteristics as derived from the Moderate-Resolution Imaging Spectroradiometer: A case study for the Beijing metropolitan area, *Journal of Geophysical Research-Atmospheres*, *112*(D22).

Weaver, C. P., et al. (2009), A Preliminary Synthesis of Modeled Climate Change Impacts on Us Regional Ozone Concentrations, *Bulletin of the American Meteorological Society*, *90*(12), 1843-1863.

Wild, M. (2009), Global dimming and brightening: A review, *Journal of Geophysical Research-Atmospheres*, *114*.

Wild, M., D. Folini, C. Schar, N. Loeb, E. G. Dutton, and G. Konig-Langlo (2013), The global energy balance from a surface perspective, *Clim Dynam*, *40*(11-12), 3107-3134, doi:Doi 10.1007/S00382-012-1569-8.

Wild, M., A. Ohmura, H. Gilgen, and J. J. Morcrette (1998), The distribution of solar energy at the Earth's surface as calculated in the ECMWF Re-Analysis, *Geophysical Research Letters*, *25*(23), 4373-4376.

Wild, M., A. Ohmura, H. Gilgen, and E. Roeckner (1995), Validation of General-Circulation Model Radiative Fluxes Using Surface Observations, *Journal of Climate*, *8*(5), 1309-1324.

Wilson, K. B., and T. P. Meyers (2001), The spatial variability of energy and carbon dioxide fluxes at the floor of a deciduous forest, *Boundary-Layer Meteorology*, *98*(3), 443-473.

Wu, W., Y. G. Liu, and A. K. Betts (2012), Observationally based evaluation of NWP reanalyses in modeling cloud properties over the Southern Great Plains, *Journal of Geophysical Research-Atmospheres*, *117*.

Yu, L., X. Jin, and R. A. Weller (2008), Multidecade Global Flux Datasets from the Objectively Analyzed Air-sea Fluxes (OAFlux) Project: Latent and sensible heat fluxes, ocean evaporation, and related surface meteorological variables, *OAFlux Project Technical Rep. OA-2008-01*, 64 pp, Woods Hole Oceanographic Institution, Woods Hole. Massachusetts.

Zhang, Y. C., W. B. Rossow, and A. A. Lacis (1995), Calculation of Surface and Top of Atmosphere Radiative Fluxes from Physical Quantities Based on Isccp Data Sets .1. Method and Sensitivity to Input Data Uncertainties, *Journal of Geophysical Research-Atmospheres*, *100*(D1), 1149-1165.

Zhang, Y. C., W. B. Rossow, A. A. Lacis, V. Oinas, and M. I. Mishchenko (2004), Calculation of radiative fluxes from the surface to top of atmosphere based on ISCCP and other global data sets: Refinements of the radiative transfer model and the input data, *Journal of Geophysical Research-Atmospheres*, *109*(D19).

Zhao, M., and Z. E. Wang (2010), Comparison of Arctic clouds between European Center for Medium-Range Weather Forecasts simulations and Atmospheric Radiation Measurement Climate Research Facility long-term observations at the North Slope of Alaska Barrow site, *Journal of Geophysical Research-Atmospheres*, *115*.

Zhao, P., Z. J. Zhou, and J. P. Liu (2007), Variability of Tibetan spring snow and its associations with the hemispheric extratropical circulation and East Asian summer monsoon rainfall: An observational investigation, *Journal of Climate*, *20*(15), 3942-3955.

Zhou, L. M., R. E. Dickinson, Y. H. Tian, J. Y. Fang, Q. X. Li, R. K. Kaufmann, C. J. Tucker, and R. B. Myneni (2004), Evidence for a significant urbanization effect on climate in China, *Proceedings of the National Academy of Sciences of the United States of America*, *101*(26), 9540-9544.

Zib, B. J., X. Q. Dong, B. K. Xi, and A. Kennedy (2012), Evaluation and Intercomparison of Cloud Fraction and Radiative Fluxes in Recent Reanalyses over the Arctic Using BSRN Surface Observations, *Journal of Climate*, *25*(7), 2291-2305.

Appendix A Radiometric resistance to heat transfer

Submitted to *Boundary-Layer Meteorology* as Zhao, L., X. Lee, A. E. Suyker, and X. Wen (2015), Influence of leaf area index on the radiometric resistance to heat transfer

Summary

Sensible heat flux is an important component of the surface energy balance. Land surface models often use the radiative surface temperature instead of the aerodynamic temperature to predict the surface sensible flux, because the former is much easier to be observed by remote sensing or to be computed from the surface energy balance equation. In this study, using measurements at 44 FLUXNET sites we examine the stability and LAI (leaf area index) dependence of the radiometric resistance, a resistance that should be included in the bulk transfer method if the radiometric temperature is used for the flux calculation. Results show that the radiometric resistance is much higher under stable conditions than under unstable conditions. In unstable conditions, the radiometric resistance is highly sensitive to LAI, decreasing exponentially as LAI increases. Omission of the radiometric resistance from the bulk transfer method will cause large overestimation in the sensible heat flux, especially for low LAI surfaces and under unstable conditions.

A.1 Introduction

The bulk transfer equation (Equation 1) [*Garratt and Francey*, 1978; *Garratt and Hicks*, 1973; *Monteith*, 1973] is a widely employed method for estimating sensible heat flux (H) in land surface models (LSMs) [*Mahrt and Vickers*, 2004]. It uses the difference between the air temperature at a reference height in the surface layer (T_a) and the aerodynamic temperature (T_0), and a heat resistance that accounts for the heat diffusion between the two heights:

$$H = \rho C_p \frac{T_0 - T_a}{R_{ah}} \qquad \text{(A.1)}$$

where ρ is air density, and C_p is the air heat capacity and R_{ah} is given as,

$$R_{ah} = \frac{[\ln(\frac{z-d}{z_0}) - \Psi_M][\ln(\frac{z-d}{z_h}) - \Psi_H]}{k^2 u} \qquad \text{(A.2)}$$

where k is the von Karman constant, z is the measurement height of T_a and wind speed u, d is the displacement height, z_0 is the roughness length for momentum, z_h is the roughness length for heat, and Ψ_M and Ψ_H are the stability correction functions for momentum and heat, respectively.

The accuracy of Equation (A.1) depends on how the surface temperature is chosen. Use of R_{ah} defined in Equation (A.2) requires that T_0 be the aerodynamic temperature at the roughness length for heat, z_h. The two roughness lengths in Equation (A.2) are typically different [*Garratt and Hicks*, 1973] and their ratio is a function of surface stiffness and the roughness Reynolds number [*Molder and Lindroth*, 2001]. A universal and robust parameterization of z_h across a large variety of land cover types does not exist. Therefore two alternative approaches are used to remove z_h from the bulk transfer method. In one approach, z_h is assumed to be equal to z_0, and R_{ah} is simply reduced to the aerodynamic resistance R_a,

$$R_a = \frac{[\ln(\frac{z-d}{z_0}) - \Psi_M][\ln(\frac{z-d}{z_0}) - \Psi_H]}{k^2 u} \qquad \text{(A.3)}$$

. In the other approach, R_{ah} is expressed as a combination of the aerodynamic resistance, R_a and the excess resistance, R_{ex},

$$R_{ah} = R_a + R_{ex} \quad \text{(A.4)}$$

In neutral stability, manipulation of Equations (A.2), (A.3) and (A.4) gives,

$$R_{ex} = \frac{\ln(z_0 / z_h)}{k u_*} \quad \text{(A.5)}$$

where u_* is the friction velocity.

One difficulty with the above formulations is that T_0 cannot be measured directly. In field campaigns, this temperature is usually inferred from extrapolation of the temperature profile to z_0 or z_h according to the Monin-Obukhov similarity theory [*Garratt and Francey*, 1978; *Thom et al.*, 1975]. Both z_0 and z_h, however, are within the roughness sublayer where the similarity theory does not hold. Therefore, the extrapolation of temperature profile is an important source of error. In addition, vertical temperature profiles are generally not available in remote sensing applications [*Kustas and Anderson*, 2009; *Kustas et al.*, 2003; *Matsushima*, 2005; *Mu et al.*, 2011]. For these reasons, in practice T_0 is usually replaced with the surface radiative temperature T_s which can be measured by remote sensing techniques or computed from the surface energy balance equation [*Sun and Mahrt*, 1995]. Use of T_s in place of T_0 for the bulk parameterization is especially attractive to modelers because in almost all land surface models, T_s is an important prognostic variable solved from the surface energy balance equation.

Previous researchers have reported that T_s and T_0 can be very different, especially in unstable conditions, and a simple substitution of T_0 by T_s can result in systematic high

biases in the prediction of sensible heat flux [*Beljaars and Holtslag*, 1991; *Choudhury et al.*, 1986; *Hall et al.*, 1992]. To date, efforts to remediate the problem fall into three categories:

- To predict T_0 from T_s: In some studies, the relationship between the radiative and aerodynamic temperature is expressed as a function of z_h [*Brutsaert and Sugita*, 1992; *Garratt and Francey*, 1978]. *Beljaars and Holtslag* [1991] suggested that their relationship should depend on the temperature scale θ_* and air stability. *Mahrt and Vickers* [2004] and *Matsushima* [2005] found that $T_s - T_0$ is related to solar radiation and leaf area index (LAI).
- To introduce a new roughness length z_r, called "radiometric roughness length", which is smaller than z_h by up to a few orders of magnitude: In a number of studies, the kB^{-1} parameter is redefined as $\ln(\frac{z_0}{z_r})$ instead of the standard formulation [$kB^{-1} = \ln(\frac{z_0}{z_h})$]; this new kB^{-1} number is related to the roughness Reynolds number and T_s [*Kustas et al.*, 1989; *Stewart et al.*, 1994; *Sugita and Brutsaert*, 1990; *Sun and Mahrt*, 1995; *Yang et al.*, 2003]. These studies show that the new kB^{-1} behaves erratically, and that a universal parameterization seems impossible.
- to add an extra resistance: a "radiometric resistance", R_r, is added to the bulk transfer formulation [*Lhomme et al.*, 1988; *Stewart et al.*, 1994], such that,

$$H = \rho C_p \frac{T_s - T_a}{R_r + R_{ah}} \qquad \text{(A.6)}$$

According to *Lhomme et al.* [1988]; *Stewart et al.* [1994], R_r is generally larger than R_{ah}.

A number of studies have suggested the importance of LAI and air stability in controlling the biases caused by substituting T_0 with T_s. *Beljaars and Holtslag* [1991] found that $T_0 - T_s$ varies from 6 K in stable conditions to -6 K in unstable conditions. *Mahrt and Vickers* [2004] reported a significant positive linear dependence of $T_s - T_o$ on solar radiation and a negative dependence on LAI. One way that solar radiation influences the heat transfer is through its effect on air stability. These relationships have been established with observations at several land cover types including a bare soil site, three grassland sites, a cropland site and 4 forest sites. *Kustas et al.* [2007] found that the slopes and intercepts of the linear regressions that *Mahrt and Vickers* [2004] proposed vary considerably when applied to a wider range of landscapes (LAI: 0.5 – 3.0) and meteorological conditions. Similarly, the correction factor proposed by *Matsushima* [2005] for $T_s - T_0$ has a strong correlation with LAI. In a recent study, *Zheng et al.* [2012] developed new formulations of the momentum and thermal roughness lengths using a green vegetation fraction derived from the remotely-sensed normalized difference vegetation index, the latter of which is known to be a good estimator of LAI.

The primary objective of this study is to revisit the roles of LAI and air stability in the bulk formulation. Our focus is on patterns of the radiometric resistance R_r across a diverse set of ecosystems. Previous studies have been restricted to a small number of

sites (1 to 9). Here we deploy data obtained from 44 sites in the FLUXNET network. Specifically, we examine how site mean resistance values vary across the sites, instead of half-hourly values at a specific site as was done in previous studies. The advantage of this site-mean approach is that it brings out more clearly patterns caused by land cover differences from synoptic meteorological fluctuations and instrument noises. In addition, we provide an assessment of the prediction error of sensible heat flux caused by omission of R_r from Equation (A.6).

A.2 Data and Methods

A.2.1 Surface observations

In this study, we examined tower observations from 44 FLUXNET sites in the US, Canada and China (Table A.1). FLUXNET is a global network of surface eddy-covariance observations. These sites cover a large range of u_* (site mean value 0.10 – 1.45 m s^{-1}). We chose these sites because measurement was made of the longwave components of the surface radiation balance, in addition to the energy and momentum fluxes and micrometeorological variables, and for long enough time (> 12 months). They span a large range of LAI (0 to 9) and canopy height (0.1 to 33 m). They are divided into four categories: 19 conifer forest sites (with nearly constant LAI throughout the year), 12 deciduous forest sites (with seasonal LAI change), 6 grassland sites (with seasonal LAI change), and 7 cropland sites(with sharp LAI change between growing and non-growing season). For each site, we selected one year of measurements and confined our analysis to December - February and June - August for the winter and summer seasons (>90% data coverage for each site for each

season). We also separate the data into stable and unstable conditions. The original data are half-hour values for 43 sites; for four sites (site ID: US-MMS, US-Ne1, US-Ne2 and US-Ne3, Table A.1) only hourly measurements are available.

Table A.1 List of the selected FLUXNET sites and their land surface types.

Site ID	Site Name	State /Prov.	Lat.	Lon.	Vegetation	Reference
CA-WP1	Western Peatland	AB	54.95	-112.47	Conifer	(Syed, Flanagan et al. 2006)
CA-Obs	Old Black Spruce	SK	53.99	-105.12	Conifer	(Jarvis, Massheder et al. 1997)
CA-SJ2	SK-2002 Jack Pine	SK	53.94	-104.65	Conifer	(Coursolle, Margolis et al. 2006)
CA-Ojp	Old Jack Pine	SK	53.92	-104.69	Conifer	(Baldocchi, Vogel et al. 1997)
CA-SJ3	SK-1975 (Young) Jack Pine	SK	53.88	-104.65	Conifer	(Mahrt and Vickers 2002)
CA-Oas	Old Aspen	SK	53.63	-106.20	Deciduous	(Blanken, Black et al. 1997)
CA-Ca1	Douglas-fir 1949	SK	49.87	-125.33	Conifer	(Humphreys, Black et al. 2003)
CA-Qfo	Quebec Mature Boreal Forest	QC	49.69	-74.34	Conifer	(Bergeron, Margolis et al. 2007)
CA-Ca3	Douglas-fir 1988	BC	49.53	-124.90	Conifer	(Humphreys, Black et al. 2006)
US-FPe	Fort Peck	MT	48.31	-105.10	Grassland	(Schmidt, Hanson et al. 2011)
CA-Gro	Groundhog River Mixedwood	ON	48.22	-82.16	mixed	(Coursolle, Margolis et al. 2006)
CA-Na1	Nashwaak Lake 1 1967 Balsam Fir	NB	46.47	-67.10	Deciduous	(Coursolle, Margolis et al. 2006)
US-WCr	Willow Creek	WI	45.81	-90.08	Deciduous	(Davis, Bakwin et al. 2003)
US-UMB	UMBS	MI	45.56	-84.71	Deciduous	(Schmid, Su et al. 2003)
CA-Mer	Mer Bleue Eastern Peatland	ON	45.41	-75.52	Deciduous	(Coursolle, Margolis et al. 2006)
US-Ho2	Howland Forest West Tower	ME	45.21	-68.75	Conifer	(Thornton, Law et al. 2002)
US-Ho3	Howland Forest East Tower	ME	45.21	-68.73	Conifer	(Hollinger, Aber et al. 2004)
US-Ho1	Howland Forest Main	ME	45.20	-68.74	Conifer	(Hollinger, Goltz et al. 1999)
US-MRf	Marys River	OR	44.65	-123.55	Conifer	(Vickers, Thomas et al. 2009)
US-Me2	Metolius Intermediate Pine	OR	44.45	-121.56	Conifer	(Law, Turner et al. 2004)
US-Bkg	Brookings	SD	44.35	-96.84	Grass/Crops	(Gilmanov, Tieszen et al. 2005)

US-Me3	Metolius Second Young Pine	OR	44.32	-121.61	Conifer	(Vickers, Thomas et al. 2009)
CN-Du2	Duolun-grassland	Inner Mongolia	42.05	116.28	Grassland	(Chen, Chen et al. 2009)
US-GLE	GLEES	WY	41.36	-106.24	Conifer	(Massman 2000)
US-Ne3	Mead rainfed maize-soybean rotation	NE	41.18	-96.44	Cropland	(Suyker, Verma et al. 2005)
US-Ne1	Mead irrigated continuous maize	NE	41.17	-96.48	Cropland	(Suyker, Verma et al. 2004)
US-Ne2	Mead irrigated maize-soybean rotation	NE	41.16	-96.47	Cropland	(Suyker, Verma et al. 2004)
US-NR1	Niwot Ridge	CO	40.03	-105.55	Conifer	(Monson, Turnipseed et al. 2002)
US-Bo1	Bondville	IL	40.01	-88.29	Cropland	(Hollinger, Bernacchi et al. 2005)
US-Slt	Silas Little Experimental Forest	NJ	39.91	-74.60	Deciduous	(Clark, Skowronski et al. 2010)
US-MMS	Morgan Monroe State Forest	IN	39.32	-86.41	Deciduous	(Schmid, Grimmond et al. 2000)
US-CaV	Canaan Valley	WV	39.06	-79.42	Cropland	(Hollinger, Ollinger et al. 2010)
US-MOz	Missouri Ozark	MO	38.74	-92.20	Deciduous	(Gu, Meyers et al. 2006)
US-Var	Vaira Ranch	CA	38.41	-120.95	Shrubs/Grassland	(Ma, Baldocchi et al. 2007)
US-ARM	ARM Southern Great Plains	OK	36.61	-97.49	Grass/Crops	(Fischer, Billesbach et al. 2007)
US-WBW	Walker Branch	TN	35.96	-84.29	Deciduous	(Wilson and Meyers 2001)
US-NC1	North Carolina Clearcut	NC	35.81	-76.71	Deciduous	(Noormets, Gavazzi et al. 2010)
US-NC2	North Carolina Loblolly Plantation	NC	35.80	-76.67	Conifer	(Noormets, Gavazzi et al. 2010)
US-Fwf	Flagstaff Wildfire	AZ	35.45	-111.77	Shrubs	(Dore, Kolb et al. 2008)
US-Fmf	Flagstaff Managed Forest	AZ	35.14	-111.73	Conifer	(Dore, Kolb et al. 2008)
US-Fuf	Flagstaff Unmanaged Forest	AZ	35.09	-111.76	Conifer	(Dore, Kolb et al. 2008)
US-Goo	Goodwin Creek	MS	34.25	-89.87	Deciduous	(Wilson and Meyers 2007)
US-SRM	Santa Rita Mesquite	AZ	31.82	-110.87	Shrubs/Grassland	(Scott, Jenerette et al. 2009)
US-Aud	Audubon Research Ranch	AZ	31.59	-110.51	Grassland	(Krishnan, Meyers et al. 2012)

Except for the Mead Irrigated cropland site in Nebraska (site ID, US-Ne1, Table A.1), all the results were reported as site mean values. At the Mead cropland site, high frequency measurement of LAI was available from 2006 to 2012, showing large LAI changes within the growing season. To capture these seasonal variations, we analyzed the daily mean quantities for this site.

A.2.2 Data Analysis

We computed the half-hourly or hourly R_r using Equation (A.6). In this equation, the total heat resistance consists of three additive components (Figure A.1). The aerodynamic resistance R_a was determined with Equation (A.3). The excess resistance R_{ex} was approximated by

$$R_{ex} = \frac{2}{ku_*} \qquad \text{(A.7)}$$

Equation (A.7) indicates that $\frac{z_0}{z_h} = 7.4$, a typical ratio for rough surfaces [*Garratt*, 1994]. The corresponding kB^{-1} value is 2. Making use of Equations (A.4), (A.6), and (A.7), we obtained an expression for computing R_r:

$$R_r = \frac{\rho C_p (T_s - T_a)}{H} - R_a - \frac{2}{ku_*} \qquad \text{(A.8)}$$

In Equation (A.2), (A.3), and (A.8), H, T_a and u_* were from direct tower measurements, T_s, ρ, R_a and the stability correction factor Ψ_M and Ψ_H were calculated using measured variables, and d and z_o were assumed as 70% and 10% of the canopy height (h), respectively.

We separated the data between stable and unstable conditions by the direction of the surface sensible heat flux:

H < -5 W m^{-2} stable condition

H > 5 W m^{-2} unstable condition.

The surface radiative temperature T_s was determined from the upward longwave radiation flux and corrected for the surface reflection of the downward longwave radiation flux, as

$$T_s = \left[\frac{(L_{\uparrow} - (1-\varepsilon)L_{\downarrow})}{\varepsilon\sigma} \right]^{1/4} \qquad \text{(A.9)}$$

where $L_{\uparrow}$ is the upward longwave radiation, $L_{\downarrow}$ is the downward longwave radiation, ε is the surface emissivity (assumed to be 0.98), and σ is the Stefan-Boltzmann constant.

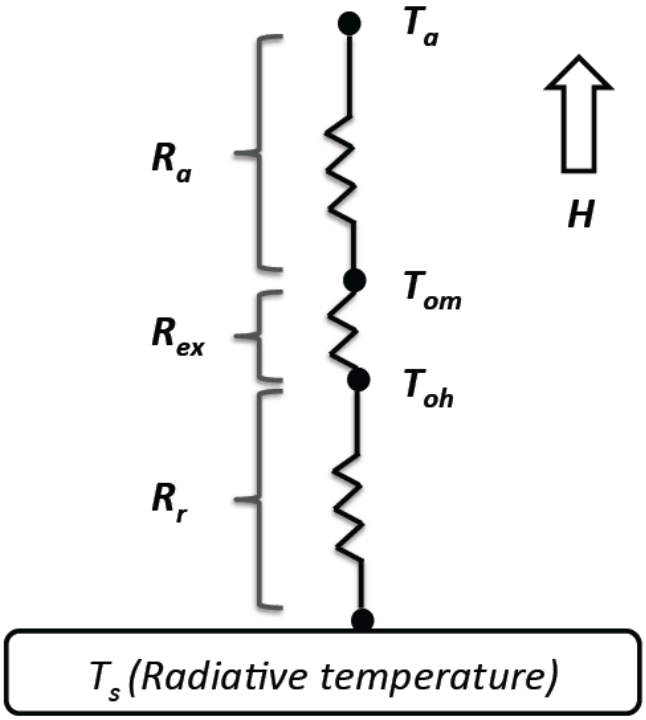

Figure A.1 Schematic of the resistance decomposition model for calculating the sensible heat flux, *H*. T_{oh} is the aerodynamic temperature at the thermal roughness height; T_{om} is the aerodynamic temperature at the momentum roughness height.

A.3 Results and Discussion

A.3.1 Relations of heat resistances to LAI under unstable conditions

In this section, we provide a detailed examination of the resistances under unstable conditions. Previous studies have shown that the bulk formulation is much more uncertain under unstable conditions than under stable conditions. The excess resistance R_{ex} shows little dependence on LAI (Figure A.2e, A.2f). The excess resistance arises from the fact that heat is transferred by molecular diffusion through the laminar boundary layer in immediate contact with the surface whereas the

momentum exchange is more efficient due to viscous shear and form drag [*Thom*, 1972]. The form drag is associated with the individual roughness elements of a surface, and the viscous shear is related to wind speed. The molecular heat diffusion, however, depends mainly on the temperature field of the fluid. The insensitivity of R_{ex} to LAI suggests that R_{ex} is controlled primarily by these processes at the leaf scale and is not affected by the amount or arrangement of the foliage elements at the canopy scale.

Unlike the excess resistance, the radiometric resistance R_r behaves more dynamically. It shows an exponential decay as LAI increases (Figure A.2a and A.2b). At low LAI values (LAI < 1), R_r is 3.7 times larger than R_{ex} in the summer and 1.4 times larger in the winter. An alternative interpretation is that the effective z_r is much smaller than z_h for sparse vegetation. Because at sites of larger R_r the temperature difference T_s - T_0 should be larger in magnitude, our results are consistent with those found by *Mahrt and Vickers* [2004]. Using airbone measurements in the Southern Great Plains Experiment, these authors showed that $T_s - T_0$ can be described by the simple linear expression model,

$$T_s - T_0 = C\left[S - C_s(LAI - LAI_{ref})\right] \qquad \text{(A.10)}$$

where C and C_s are positive regression coefficients, S is solar radiation, and the reference LAI value (LAI_{ref}) is approximately 1.0. This expression illustrates that $T_s - T_0$ is large when LAI is small. They also acknowledged that a more complex function of LAI is required for very large LAIs. The dependence on S is explained by the fact that sunlit surfaces warm up faster than the air at the roughness height.

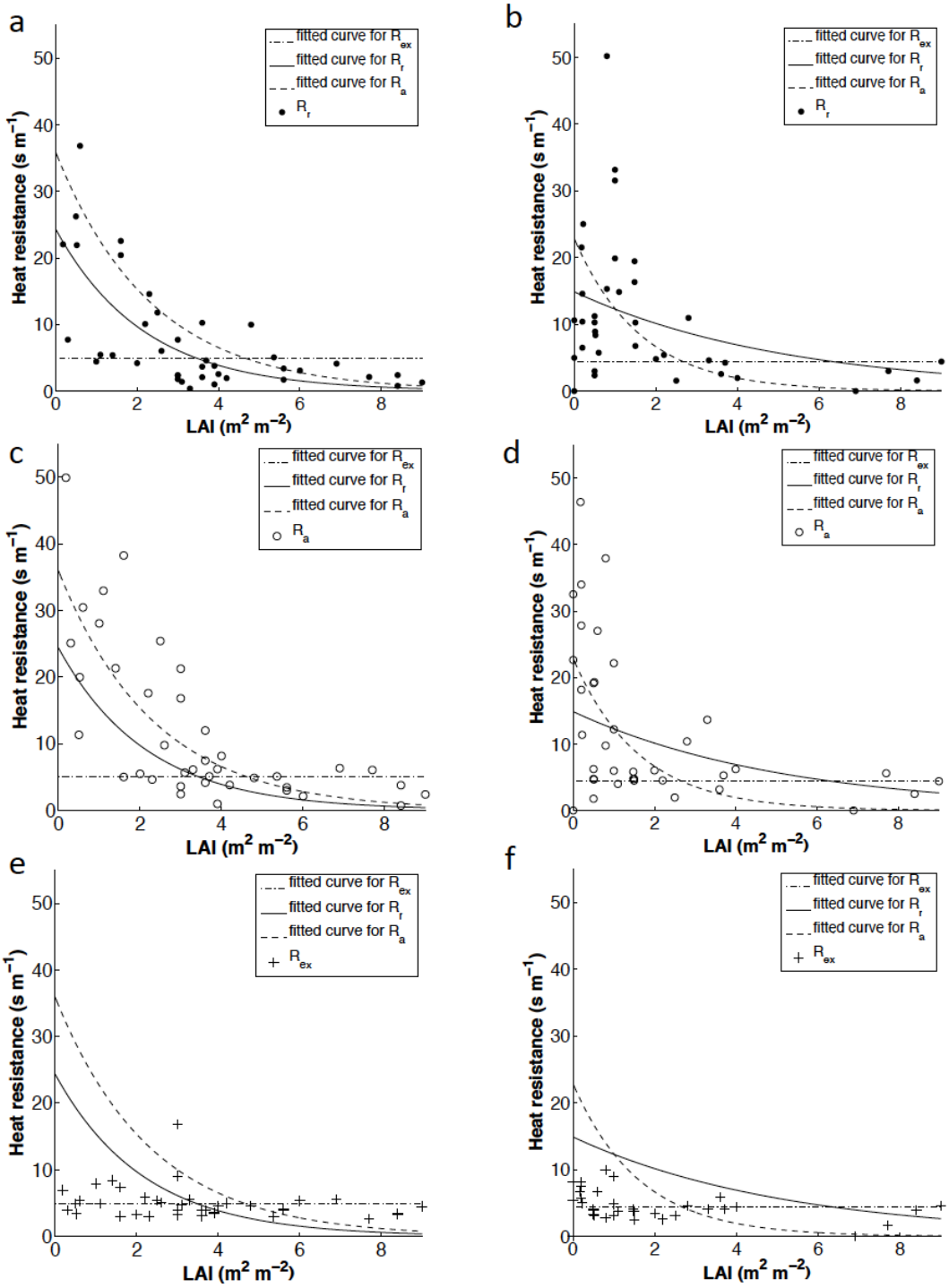

Figure A.2 Relationship between the three heat resistances and LAI under unstable conditions. a, c, e: summer; b, d, f: winter. Each date point represents a site seasonal mean value. Lines are regression fits to the data: R_r, $y = 24.4\exp(-0.5x)$ (summer), $y = 14.9\exp(-0.2x)$ (winter); R_a, $y = 35.9\exp(-0.4x)$ (summer), $y = 22.9\exp(-0.6x)$ (winter); R_{ex}, $y = 5.0$ (summer), $y = 4.4$ (winter).

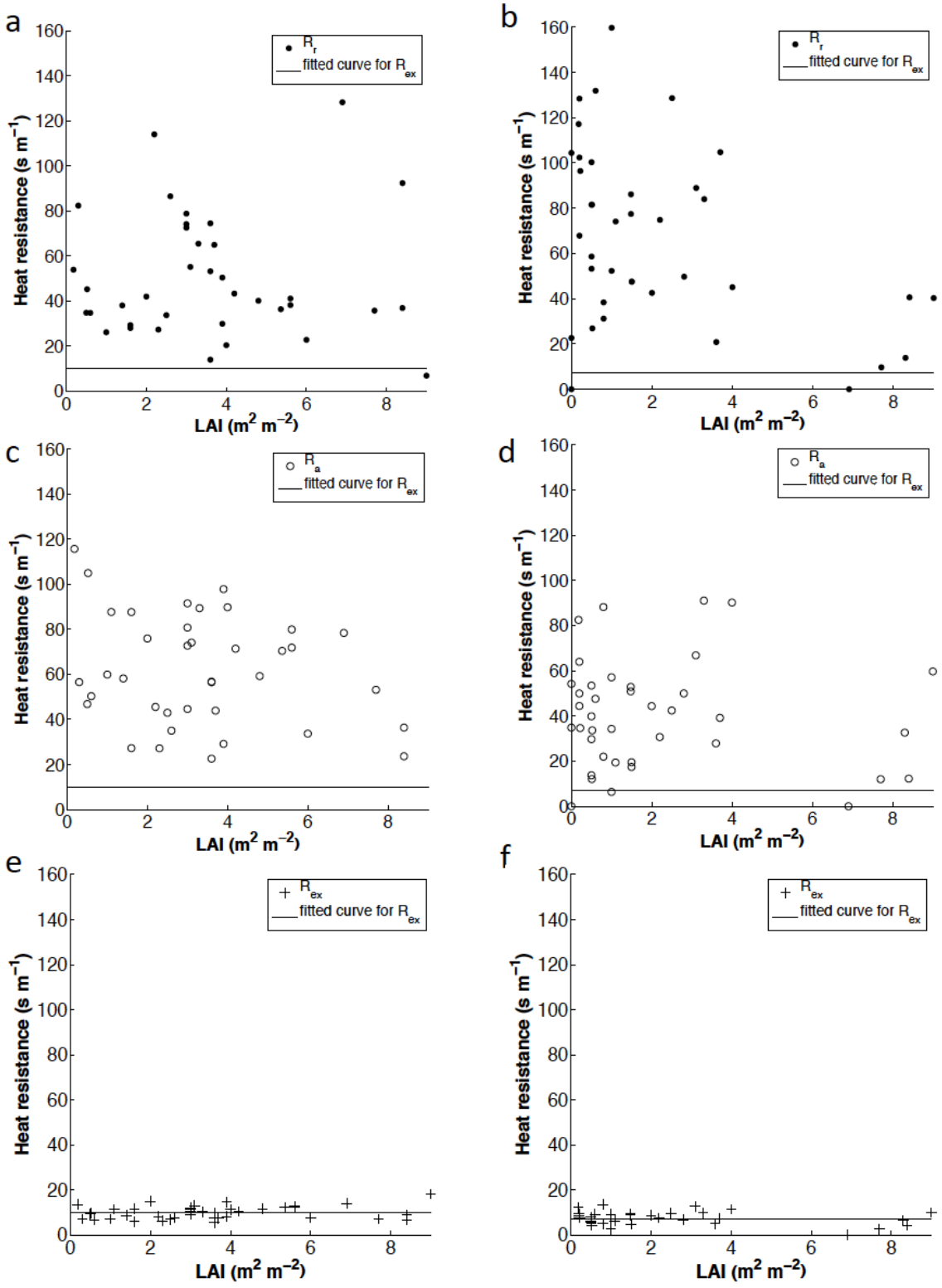

Figure A.3. Same as Figure 2 except for under stable conditions.

The aerodynamic resistance R_a behaves similarly to R_r as LAI changes (Figure A.2c and A.2d). In terms of magnitude, R_a is comparable with R_r. The physical explanation of the exponential correlation between the LAI and the aerodynamic resistance lies in the convection efficiency. High LAI usually corresponds to aerodynamically rough surfaces that trigger large coherent eddies which are efficient in heat convection, whereas low LAI surfaces (grassland or fallow cropland) are more like bluff-rough surfaces which are less efficient to generate eddies [*Stewart et al.*, 1994; *Voogt and Grimmond*, 2000].

A.3.2 Summer versus winter

There is some seasonal difference in the three resistances (Table A.2). Figure A.2 shows that the general patterns on LAI are similar between the summer and winter seasons. In the winter when LAI is small, the site-mean values of R_r and R_a are more scattered than those in the summer (Figure A.2a-d). One reason is related to deciduous forest sites. These sites have low LAI in the winter, but are still aerodynamically rough. Instead of assuming z_o being proportional to stand height, an improved parameterization, such as in *Raupach* [1994] where z_o is a function of both canopy height and LAI, may reduce these scatters.

In terms of magnitude, only R_r shows higher values in the winter than in the summer, whereas the other two resistances do not show much seasonal differences. The R_r seasonality is partly explained by LAI changes. For the deciduous forest group, the average winter LAI is low (1.5), and the average R_r is 65.6 s m^{-1}. In the summer when the average LAI increases to 4.1, the average R_r is 37.0 s m^{-1}. It appears that the

seasonal LAI change alters the radiative property of the surface that is related to the radiometric resistance, but the exact nature of this property is not known.

For the coniferous forest site group, because the difference in the average LAI between summer and winter is very small, the seasonal difference R_r is largely reduced (Table A.2). The LAI difference is not zero between summer and winter for this group because of the presence of deciduous understory vegetation and deciduous trees at some of the coniferous sites.

The R_r in the cropland group behaves similarly to the deciduous forest group, showing much larger values in the winter than in the summer. The grassland/shrubland group, unlike the deciduous forest and cropland groups, shows little difference in R_r between summer and winter under unstable conditions. This is because for grasslands, unless it is burned, dead vegetation is still standing at the surface, whereas for cropland there is a drastic difference in the vegetation stands between growing and non-growing season.

Table A.2 Statistics of the three component resistances among all the sites.

Veg. Type	Season	Stability	LAI	Rr	Ra	Rex
				mean±s.e. (s m-1)	mean±s.e. (s m-1)	mean±s.e. (s m-1)
Deciduous	Summer	Unstable	4.1	4.3±09	7.6±2.1	5.5±1.2
		Stable		46.8±6.9	54.8±7.6	9.5±0.8
	Winter	Unstable	1.5	8.6±1.8	9.3±3.1	4.1±0.5
		Stable		78.3±9.7	28.1±5.3	6.1±0.6
Conifer	Summer	Unstable	4.0	6.4±1.8	8.2±2.5	4.1±0.2
		Stable		51.8±6.3	66.5±6.0	10.6±0.8
	Winter	Unstable	3.4	9.3±2.0	9.2±2.4	3.8±0.4
		Stable		59.8±9.4	44.0±5.9	7.3±0.8
Grass/Shrub	Summer	Unstable	1.2	17.5±5.2	27.7±3.7	6.0±0.5
		Stable		31.8±1.6	62.6±8.3	8.8±0.9
	Winter	Unstable	0.3	16.9±7.5	20.6±5.7	5.4±1.4
		Stable		56.0±17.8	44.2±11.9	7.1±1.8
Crop	Summer	Unstable	3.6	8.5±0.5	19.8±1.7	6.3±1.0
		Stable		98.3±8.5	58.3±5.2	8.8±0.8
	Winter	Unstable	0.4	17.5±4.8	22.7±1.8	7.4±0.6
		Stable		98.1±16.2	50.4±2.4	8.9±0.1

A.3.3 Daily variations

In order to further investigate the influence of LAI, we analyzed the daily variations of the radiometric resistance for a cropland site with continuous maize plantation, Mead Irrigated site in Nebraska (site ID, US-Ne1, Table A.1). The growing season is from the beginning of June to the end of September. The irrigated cropland site has a more dynamic LAI change over the year compared to a typical forest or grassland site.

The patterns seen in the seasonal mean values across multiple sites still hold for the daily values at this specific site (Figure A.4). The multiyear data show obvious annual

cycles of R_r with a range from -20 to 330 s m^{-1} in variations (Figure A.4a and b). The trend of the cycle is just opposite to the phase of the crop LAI cycle. The seasonal pattern is much stronger under unstable conditions than under stable conditions, which is consistent with what was observed in the seasonal mean values at multiple sites (Figure A.2).

Under unstable conditions, the day-to-day variation is smaller than the contrast between the growing and the non-growing season. For example, in the year 2008 – 2009 the standard deviation of the daily R_r is 6.1 s m^{-1} for the growing season (June 10th 2008- October 7th 2008) under unstable conditions. For comparison the mean difference between the two seasons is 56.7 s m^{-1} under unstable conditions. The day-to-day flucutations were caused by variations in the site microclimatic conditions. Since the goal of this research is to better isolate the influences on the heat resistances from different land surface types, these variations are unwanted "random noises". By using seasonal mean values, these fluctuations were filtered out.

Under unstable conditions, the daily mean R_r shows a similar pattern (Figure A.4c) as the seasonal mean across the sites (Figure A.2a), that is, an exponential decay of R_r with increasing LAI. Although the general pattern is similar with what is seen in the seasonal mean values at multiple sites, the regression curve is different. The difference is caused by the negative radiometric resistance values that occurred persistently in the growing season (Figure A.4a and c). The two outliers in Figure 4c should result from the measurement errors. These two days are July 12th 2006 and

July 6th 2007. For both days, during the daytime only one single value can be used to calculate resistances, because for all other hourly measurements, the sign of $T_s - T_a$ is opposite to the sign of H.

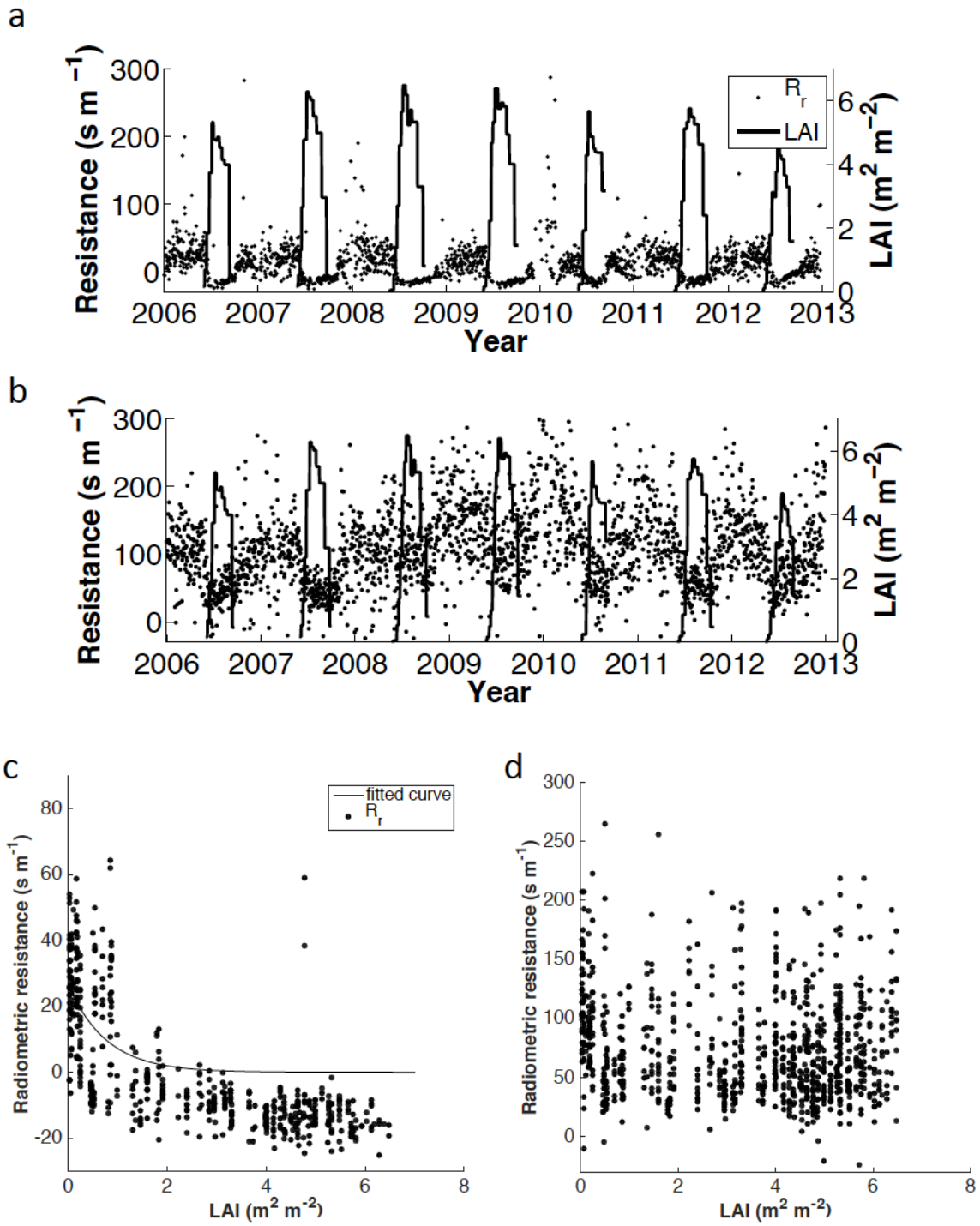

Figure A.4. Correlation between the daily radiometric resistance and LAI at the Mead Irrigated site in Nebraska (site ID, US-Ne1). a, time series under unstable conditions (daytime); b, time series under stable conditions (nighttime); c, scatter plot under unstable conditions; d, scatter plot under stable condition.

Under stable conditions, this exponential decay relationship is no longer detectable (Figure A.4d). Instead R_r appears independent of LAI. The mean R_r value is 105.1 s m^{-1}.

Negative resistances are physically unacceptable. Two possible causes of the negative R_r values in this site are contamination of the air temperature measurement by solar heating and inaccurate z_0 parameterization. The scatter plot of half-hourly H versus $T_s - T_a$ for this site revealed that at $H = 0$ W m^{-2}, the temperature difference $T_s - T_a$ had an offset of 1 – 1.5 K, indicating a potential bias in the temperature measurement. One source of bias errors was related to sunlight heating of the air temperature sensor. Another possible source of error was the temperature calibration. Vaisala calibration, which was not always a very accurate calibration, was used in this site. Indeed, reducing T_a by 1K did eliminate a number of negative R_r values and brought the result into better agreement with the site mean regression curve (Figure A.5a).

Raupach [1994] has shown that z_0 should dynamically respond to both canopy height and LAI. We then parameterized z_0 as a function of canopy height and LAI according to *Raupach* [1994] to determine if negative R_r may be caused by inaccurate z_0 parameterization. Comparison of this new result (Figure A.5a) with the calculation using fixed z_0 (Figure A.4c) shows that this dynamic parameterization has little effects on the negative R_r values.

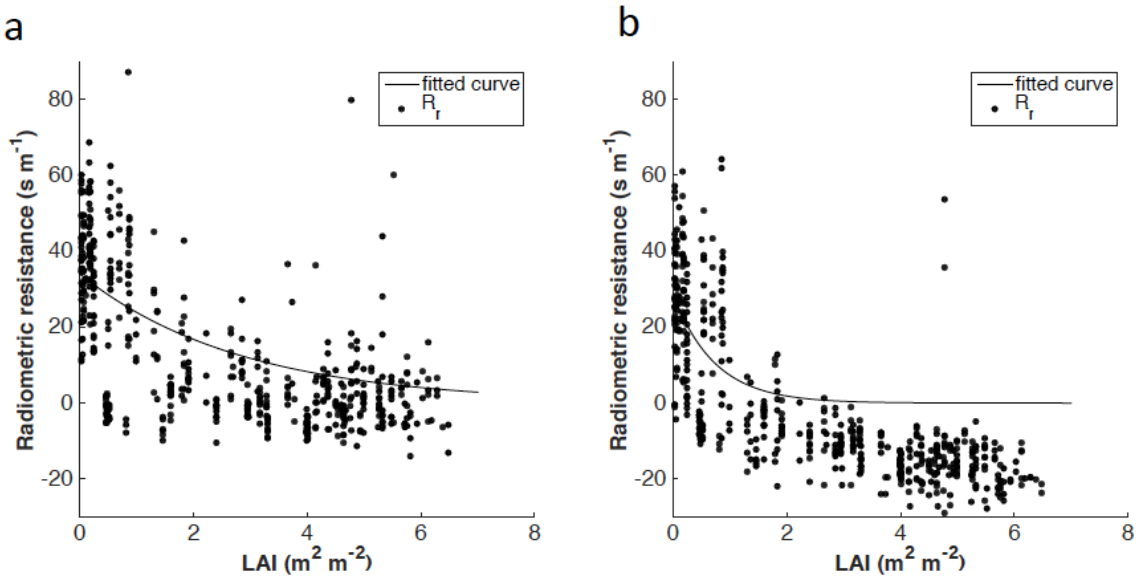

Figure A.5 Sensitivity analyses to air temperature bias and z_0 parameterization under unstable conditions for the Nebraska site. a, Ta reduced by 1.0K; b, original T_a,

$$z_0 = \exp(-2.3) \times h \times LAI^{-0.15}$$

A.3.4 Relations of heat resistances to air stability

All the three component resistances are generally larger under stable conditions than those under unstable conditions (Figures A.2 and A.3). Table A.2 shows the average resistances among all the sites under unstable and stable conditions in the summer and the winter. Our results confirm that the stratified air under stable conditions prevents the heat transfer more than the air under unstable conditions. This air stability effect has been known for a long time for aerodynamic resistance [*Garratt*, 1994]. According to our results, air stability has similar impacts on the radiometric resistance.

Under stable conditions, there is no apparent correlation between LAI and the aerodynamic resistance (summer: $R^2 < 0.05$, winter: $R^2 < 0.01$), a pattern that is different from that observed in unstable conditions (summer: $R^2 > 0.58$, winter: $R^2 > 0.30$). Under stable conditions, R_r shows no apparent correlation to the LAI either (Figure A.3a and A.3b), and is on average 40.2 s m^{-1} larger than the R_{ex} in summer and 64.8 s m^{-1} larger in winter for all the sites examined in this study. These values are compatible with the R_r estimates by *Stewart et al.* [1994] (22 – 73 s m^{-1}). Under unstable conditions, the average R_r is 7.8 s m^{-1} and is only slightly larger than R_{ex} (4.9 s m^{-1}).

A.3.5 Impacts of radiometric resistance on sensible heat flux calculation

In order to assess the impacts of radiometric resistance on the sensible heat flux calculation, we first calculated the sensible heat flux by using the complete Equation 6 and again by omitting R_r from Equation 6, as

$$\hat{H} = \rho C_p \frac{T_s - T_a}{R_a + R_{ex}} \qquad \text{(A.11)}$$

In Equation 6, R_r was obtained from the regression fit functions of LAI shown in Figure 2a (summer) and 2b (winter) for unstable conditions and constant values of 50 s m^{-1} (summer) and 66 s m^{-1} (winter) for stable conditions, and other terms were provided by field measurements. The prediction error e and the relative prediction error e_r are defined as,

$$e = \hat{H} - H \qquad \text{(A.12)}$$

$$e_r = \frac{e}{H} \qquad \text{(A.13)}$$

where H is the observed sensible heat flux.

Not surprisingly, omission of R_r results in an overestimation of the magnitude of sensible heat flux. Under stable conditions, the prediction error has no apparent correlation to the site LAI. Under unstable conditions the prediction error is much larger for low LAI sites and smaller for high LAI sites (Figure A.6a). The relative error decreases as the LAI increases under unstable conditions and has no apparent correlation with LAI under stable conditions (Figure A.6b). These results show that the largest overestimation due to omission of R_r occurs at low LAI surfaces and under unstable conditions.

Similar results can be found in published literature. In an experiment study in a soybean field, *Lee et al.* [2009] reported larger prediction errors (up to 308 W m^{-2}) for the early part of the growing season (LAI < 2) than in the middle part of the growing season (error < 15 W m^{-2}) when LAI is large (LAI = 7.6). *Chen and Zhang* [2009] compared the observed heat transfer coefficient C_h from Ameriflux sites and the modeled C_h by Noah LSM, and reported large model overestimations for short vegetation in Noah LSM. In Noah, the two roughness (z_h and z_0) are used to calculate C_h without the radiometric resistance Because C_h is inversely proportional to the heat resistance, overestimation of C_h indicates overestimation of H in the model. *Zheng et al.* [2012] reported a large cold bias in the daytime T_s (up to -15^{o}C) produced by NCEP operational Global Forecast System over the arid western continental United States where LAI is very small. In NCEP, T_s is solved from the energy balance

equation with H parameterized according to Equation (A.1) and with the approximation $T_s = T_0$. In other words, the default NCEP calculation omits the radiometric resistance. By adding the radiometric resistance as a function of vegetation fraction to the bulk formula, *Zheng et al.* [2012] significantly reduce the cold bias in T_s (average bias < -4^{o}C). Similar with our findings, they found that their R_r formulation has a minimal effect on the nighttime T_s under stable conditions.. Recently, *Zhang et al.* [2014] also reported a large high bias (120 W m^{-2}) in H calculated with a LAI-independent parameterization of z_r for a dessert steppe site, and using a time-varying heat roughness length as a function of vegetation growth reduced more than half of the root mean squared error of H.

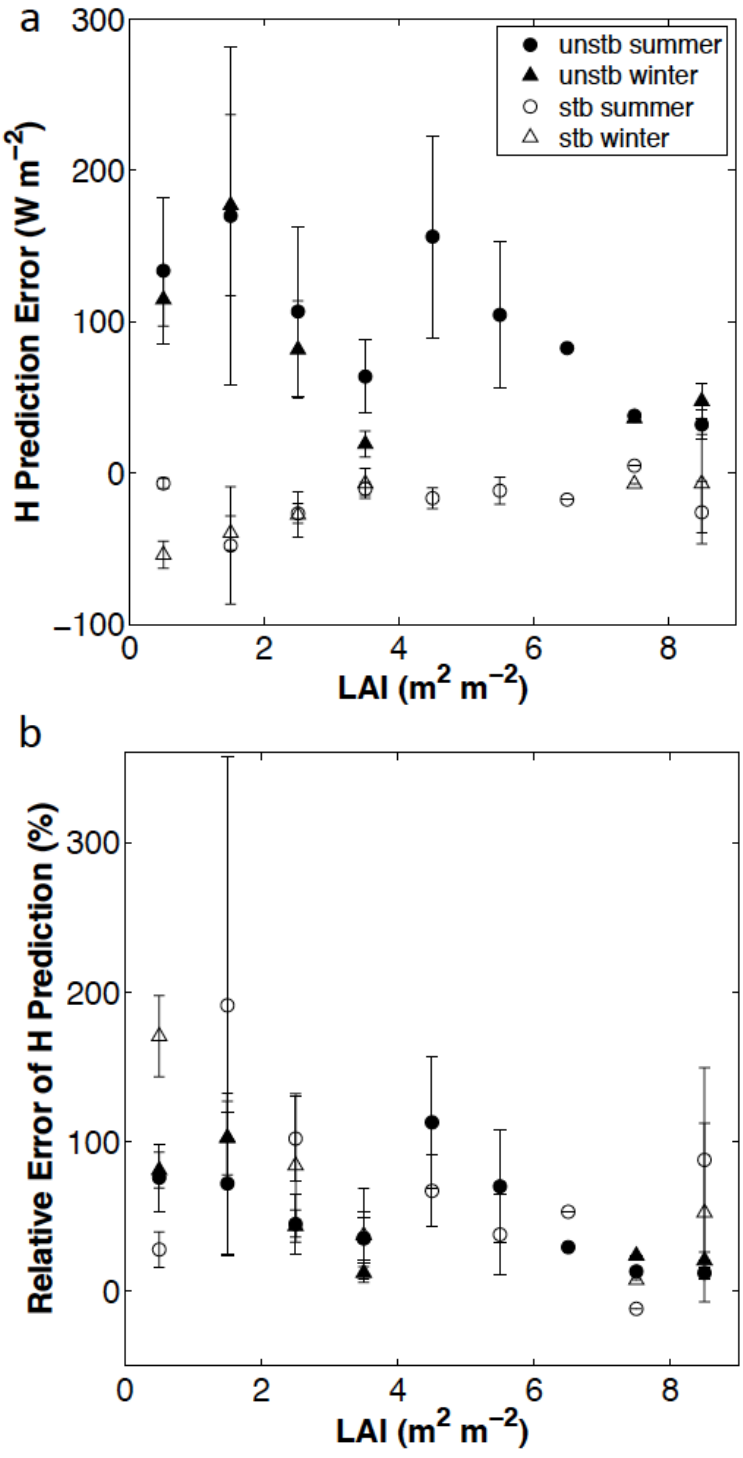

Figure A.6 Bin average prediction errors of sensible heat flux caused by omission of the radiometric resistance. Top panel: prediction error; bottom panel: relative prediction error. Error bars denote 1 s.e.

A.4 Conclusions

A simple resistance model was used to decompose the total resistance to heat transfer from the surface to the reference height into three additive components: radiometric resistance, excess resistance, and aerodynamic resistance. On average, all the resistances are higher under stable conditions than under unstable conditions. The excess resistance shows no apparent relations to the LAI change under unstable or stable conditions. The aerodynamic and radiometric resistance decrease exponentially as the LAI increases under unstable conditions. Under stable conditions, the aerodynamic and radiometric resistance show no apparent relations to the LAI change and are much larger than the excess resistance. The daily data at a cropland site show that the relations to LAI seen in the seasonal mean values across multiple sites still hold for the daily values.

High bias in the sensible heat flux calculation occurs if the radiometric resistance is omitted from the bulk transfer formulation. The overestimation is larger at lower LAI surfaces. The problem is especially severe at low LAI (<4) and under unstable conditions.

References

Beljaars, A. C. M., and A. A. M. Holtslag (1991), Flux Parameterization over Land Surfaces for Atmospheric Models, *Journal of Applied Meteorology*, *30*(3), 327-341.

Brutsaert, W., and M. Sugita (1992), Regional surface fluxes from satellite-derived surface temperatures (AVHRR) and radiosonde profiles, *Boundary-Layer Meteorology*, *58*(4), 355-366.

Chen, F., and Y. Zhang (2009), On the coupling strength between the land surface and the atmosphere: From viewpoint of surface exchange coefficients, *Geophysical Research Letters*, *36*, doi:Artn L10404
Doi 10.1029/2009gl037980.

Choudhury, B. J., R. J. Reginato, and S. B. Idso (1986), An Analysis of Infrared Temperature Observations over Wheat and Calculation of Latent-Heat Flux, *Agricultural and Forest Meteorology*, *37*(1), 75-88.

Garratt, J. R. (1994), *The atmospheric boundary layer*, Cambridge university press.

Garratt, J. R., and R. Francey (1978), Bulk characteristics of heat transfer in the unstable, baroclinic atmospheric boundary layer, *Boundary-Layer Meteorology*, *15*(4), 399-421.

Garratt, J. R., and B. B. Hicks (1973), Momentum, heat and water vapour transfer to and from natural and artificial surfaces, *Quarterly Journal of the Royal Meteorological Society*, *99*(422), 680-687, doi:10.1002/qj.49709942209.

Hall, F. G., K. F. Huemmrich, S. J. Goetz, P. J. Sellers, and J. E. Nickeson (1992), Satellite Remote-Sensing of Surface-Energy Balance - Success, Failures, and Unresolved Issues in Fife, *Journal of Geophysical Research-Atmospheres*, *97*(D17), 19061-19089.

Kustas, W. P., and M. Anderson (2009), Advances in thermal infrared remote sensing for land surface modeling, *Agricultural and Forest Meteorology*, *149*(12), 2071-2081, doi:Doi 10.1016/J.Agrformet.2009.05.016.

Kustas, W. P., M. C. Anderson, J. M. Norman, and F. Li (2007), Utility of radiometric-aerodynamic temperature relations for heat flux estimation, *Boundary-Layer Meteorology*, *122*(1), 167-187.

Kustas, W. P., B. J. Choudhury, M. S. Moran, R. J. Reginato, R. D. Jackson, L. W. Gay, and H. L. Weaver (1989), Determination of Sensible Heat-Flux over Sparse Canopy Using Thermal Infrared Data, *Agricultural and Forest Meteorology*, *44*(3-4), 197-216.

Kustas, W. P., T. Jackson, J. Prueger, J. Hatfield, and M. Anderson (2003), Remote sensing field experiments evaluate retrieval algorithms and land-atmosphere modeling, *Eos, Transactions American Geophysical Union*, *84*(45), 485-493.

Lee, X. H., T. J. Griffis, J. M. Baker, K. A. Billmark, K. Kim, and L. R. Welp (2009), Canopy-scale kinetic fractionation of atmospheric carbon dioxide and water vapor isotopes, *Global Biogeochemical Cycles*, *23*, doi:Artn Gb1002
Doi 10.1029/2008gb003331.

Lhomme, J. P., N. Katerji, A. Perrier, and J. M. Bertolini (1988), Radiative Surface-Temperature and Convective Flux Calculation over Crop Canopies, *Boundary-Layer Meteorology*, *43*(4), 383-392.

Mahrt, L., and D. Vickers (2004), Bulk formulation of the surface heat flux, *Boundary-Layer Meteorology*, *110*(3), 357-379.
Matsushima, D. (2005), Relations between aerodynamic parameters of heat transfer and thermal-infrared thermometry in the bulk surface formulation, *Journal of the Meteorological Society of Japan*, *83*(3), 373-389.
Molder, M., and A. Lindroth (2001), Dependence of kB(-1) factor on roughness Reynolds number for barley and pasture, *Agricultural and Forest Meteorology*, *106*(2), 147-152.
Monteith, J. L. (1973), *Principles of environmental physics*, American Elsevier Pub. Co.
Mu, Q. Z., M. S. Zhao, and S. W. Running (2011), Improvements to a MODIS global terrestrial evapotranspiration algorithm, *Remote Sensing of Environment*, *115*(8), 1781-1800.
Raupach, M. R. (1994), Simplified Expressions for Vegetation Roughness Length and Zero-Plane Displacement as Functions of Canopy Height and Area Index, *Boundary-Layer Meteorology*, *71*(1-2), 211-216, doi:Doi 10.1007/Bf00709229.
Stewart, J. B., W. P. Kustas, K. S. Humes, W. D. Nichols, M. S. Moran, and H. A. R. Debruin (1994), Sensible Heat-Flux Radiometric Surface-Temperature Relationship for 8 Semiarid Areas, *Journal of Applied Meteorology*, *33*(9), 1110-1117.
Sugita, M., and W. Brutsaert (1990), Regional Surface Fluxes from Remotely Sensed Skin Temperature and Lower Boundary-Layer Measurements, *Water Resources Research*, *26*(12), 2937-2944.
Sun, J. L., and L. Mahrt (1995), Determination of Surface Fluxes from the Surface Radiative Temperature, *Journal of the Atmospheric Sciences*, *52*(8), 1096-1106.
Thom, A. S. (1972), Momentum, Mass and Heat-Exchange of Vegetation, *Quarterly Journal of the Royal Meteorological Society*, *98*(415), 124-&, doi:Doi 10.1002/Qj.49709841510.
Thom, A. S., J. B. Stewart, H. R. Oliver, and J. H. C. Gash (1975), Comparison of aerodynamic and energy budget estimates of fluxes over a pine forest, *Quarterly Journal of the Royal Meteorological Society*, *101*(427), 93-105, doi:10.1002/qj.49710142708.
Voogt, J. A., and C. S. B. Grimmond (2000), Modeling surface sensible heat flux using surface radiative temperatures in a simple urban area, *Journal of Applied Meteorology*, *39*(10), 1679-1699.
Yang, K., T. Koike, and D. W. Yang (2003), Surface flux parameterization in the Tibetan Plateau, *Boundary-Layer Meteorology*, *106*(2), 245-262, doi:Doi 10.1023/A:1021152407334.
Zhang, G., G. S. Zhou, F. Chen, M. Barlage, and L. L. Xue (2014), A Trial to Improve Surface Heat Exchange Simulation through Sensitivity Experiments over a Desert Steppe Site, *J. Hydrometeorol.*, *15*(2), 664-684, doi:Doi 10.1175/Jhm-D-13-0113.1.
Zheng, W. Z., H. L. Wei, Z. Wang, X. B. Zeng, J. Meng, M. Ek, K. Mitchell, and J. Derber (2012), Improvement of daytime land surface skin temperature over

arid regions in the NCEP GFS model and its impact on satellite data assimilation, *Journal of Geophysical Research-Atmospheres*, *117*, doi:Artn D06117 Doi 10.1029/2011jd015901.